Universidade do Minho
Escola de Engenharia

José Guimarães Gomes

Design of reinforced concrete slabs under the combined effect of restrained shrinkage and applied loads

august 2023

Design of reinforced concrete slabs under the combined effect of restrained shrinkage and applied loads

José Guimarães Gomes

UMinho | 2023

Fundação para a Ciência e a Tecnologia

Cofinanciado por:

COMPETE 2020

PORTUGAL 2020

UNIÃO EUROPEIA
Fundo Europeu de Desenvolvimento Regional

Universidade do Minho
Escola de Engenharia

José Guimarães Gomes

Design of reinforced concrete slabs under the combined effect of restrained shrinkage and applied loads

Doctorate Thesis in Civil Engineering

Work conducted under the supervision of:
Professor Doctor Miguel Ângelo Dias Azenha
Professor Doctor Rui Manuel Carvalho Marques de Faria
Professor Doctor Carlos Filipe Ferreira de Sousa

august 2023

Acknowledgements

This work was financially supported by Fundação para a Ciência e Tecnologia (FCT) under the grant with reference SFRH/BD/148558/2019. This work was also developed under the scope of the research project IntegraCrete, with the reference PTDC/ECM EST/1056/2014 (POCI-01-0145-FEDER-016841), supported by FEDER funds through the Operational Program for Competitiveness Factors – COMPETE and FCT.

To all those who accompanied me throughout the development of this thesis, I express my sincere gratitude. For their importance, I offer my special thanks:

To my parents, for all the support provided throughout my academic career, as well as for the transmitted values that have been reflected in the exercise of my duties as a researcher.

To Elisabete, for the words of comfort and encouragement and for being my greatest source of motivation.

To Professor Carlos Sousa, for the unsurpassable support provided in the development of this thesis, for all the knowledge transmitted and for being someone I have always looked up to, professionally and personally.

To Professors Miguel Azenha and Rui Faria, for their support and encouragement and for the transmitted knowledge.

To my colleagues from the Doctoral program, in particular to Ricardo Cruz and Jorge Rocha, and to Hélder Sousa, with whom I had the privilege of sharing the office, for sharing ideas and knowledge and for the companionship and moments of conviviality.

To Behzad Zahabizadeh, Claúdio Ferreira, José Granja and Professors Dirk Schlicke and Mário Pimentel, with whom I had the privilege of collaborating within the framework of the work for the IntegraCrete project.

The execution of the experimental campaign would not have been possible without the support of several people. In this sense, I also express my gratitude to Marco and the rest of the team at the Structural Laboratory of the University of Minho – César, Luciano, Sr. Goncalves and Mr. Matos – for all the support given in the execution of the experimental campaign, to Patrícia Pereira and Dora Pinheiro, from LEMC (Laboratório de Ensaio de Materials de Construção - FEUP), for the loan of equipment to monitor the slabs and to Eng. Carlos Rodrigues, for his support in purchase and installation of fiber optic sensors.

Statement of integrity

I hereby declare having conducted this academic work with integrity. I confirm that I have not used plagiarism or any form of undue use of information or falsification of results along the process leading to its elaboration.

I further declare that I have fully acknowledged the Code of Ethical Conduct of the University of Minho.

Dimensionamento de lajes de betão armado sujeitas ao efeito combinado de retração restringida e cargas aplicadas

Resumo

O controlo da fissuração em estruturas de betão armado (BA) é essencial para o correto funcionamento em serviço, ao longo do respetivo período de vida útil, sem custos de manutenção acrescidos. As recomendações e códigos de dimensionamento atuais fornecem metodologias para dimensionamento de elementos de BA sujeitos aos efeitos independentes de carregamento externo ou deformações impostas restringidas. No entanto, o cálculo de forças de restrição atuantes e de abertura de fendas em estruturas sujeitas à combinação dos dois efeitos é ainda um desafio devido à falta de conhecimento sobre a complexa interação que existe entre os efeitos da flexão, viscoelasticidade e deformações impostas no desenvolvimento da fissuração.

Tendo como objetivo aprofundar os conhecimentos em relação à combinação de efeitos acima descritos, é apresentado um novo método experimental para ensaio de elementos de betão (tipo laje) restringidos. Este método consiste na utilização de um dispositivo para restrição axial de um elemento de BA sujeito, simultaneamente, a esforços de flexão e de corte. A restrição das deformações impostas é realizada através de atuadores hidráulicos conectados a uma das extremidades do proves, permitindo o ajuste progressivo do esforço axial atuante de forma a controlar a deformação de uma região de controlo previamente definida (restrição ativa).

A campanha experimental apresentada fornece uma base de dados importante para validação de abordagens numérica e analíticas para previsão do comportamento estrutural em lajes restringidas sujeitas a cargas de serviço. O comportamento higro-mecânico dos provetes ensaiados é simulado com um modelo 3D multi-físico baseado no método de elementos finitos. A mesma estratégia de simulação, é adotada na análise de um caso de estudo referente ao comportamento em serviço de uma laje unidirecional totalmente restringida e sujeita a uma combinação de ações quase-permanente

É ainda proposto um método simplificado, baseado na compatibilidade de deformações, para estimativa da força de restrição atuante a longo prazo em estruturas longitudinalmente restringidas. Este método é validado com base nas análises experimentais e numérica abordadas nesta dissertação e pode ser aplicado em combinação com as formulações mais recentes para cálculo de abertura de fenda em estruturas de betão armado, considerando um cenário de flexão composta.

Palavras-chave

Betão Armado, Deformações Restringidas, Estado Limite de Serviço; Fissuração; Retração.

Design of reinforced concrete slabs under the combined effect of restrained shrinkage and applied loads.

Abstract

Cracking control of reinforced concrete (RC) is of paramount importance to ensure a proper service behaviour on RC structures, during their lifespan, without excessive maintenance costs. Current design codes and recommendations for RC structures provide methodologies for reinforcement design on elements subjected to the independent effects of either external loads or restraints due to imposed deformations. However, the determination of restraint forces and crack width control in structures subjected to the combination of such two effects is still a challenge, due to the lack of knowledge about the complex interplay between the effects of bending, viscoelasticity and imposed deformations on crack width development.

To further investigate the aforementioned effects and their intricate interplay, a new experimental method is applied, in which a restraining device is used to constrain the axial deformation of a slab-like specimen, while allowing it to simultaneously endure bending and shear stresses. The deformation is restrained by two hydraulic actuators connected to one of the slab extremities, allowing a progressive adjustment of the axial force installed whilst controlling the deformation on a pre-defined region (active restraint).

The experimental campaign provides an important and unprecedented database for validation of numerical and analytical approaches for prediction of the structural behaviour of restrained slabs subjected to service load. In this work, the hygro-mechanical behaviour of the tested specimens is simulated with a 3D Finite Element (FE) based multi-physics framework. Upon experimental validation of the multi-physics approach, the same numerical simulation strategy is used for the analysis of a case study regarding the serviceability behaviour of a fully restrained one-way slab, subjected to a quasi-permanent load combination.

A simplified method based on the compatibility of deformation is also proposed for estimation of the long-term restraint forces. This method is validated with both experimental and numerical (based on multi-physics approach) analyses and may be applied in combination with the most up-to-date design code formulations for estimation of crack width in RC elements by considering a scenario of composed bending.

Keywords

Cracking, Reinforced Concrete, Restrained Deformation, Service Limit State; Shrinkage.

Table of Contents

List of Symbols

List of Latin Upper-Case Letters:

A_c – Area of concrete cross-section

$\overline{A_c}$ – Area of homogenised RC cross-section

$A_{c,eff}$ – Effective area of concrete

A_T – Rate constant

D_H – Moisture diffusivity

D_0 – Moisture diffusivity for $H = 0$

D_1 – Moisture diffusivity for $H = 1$

E_a – Apparent activation energy

E_c – Young modulus of concrete

E_s – Young modulus of steel

E_0 – Asymptotic Young modulus of concrete

E_μ – Stiffness of Kelvin unit μ

F_{cc} – Internal force at concrete compressive zone

F_{ct} – Internal force at concrete tensile zone

$F_{s,b}$ – Internal force at bottom reinforcement

$F_{s,t}$ – Internal force at top reinforcement

G_F – Fracture Energy

H – Relative humidity

H_c – Relative humidity for which $D_H = 0.5D_1$

H_{env} – Relative humidity of environment

H_{surf} – Relative humidity at concrete surface

$\bar{I}$ – Moment of inertia of homogenised RC cross-section

J – Specific creep

J_{exp} – Experimental specific creep

L – Free span

$L_{crcaked}$ – Cracked length

L_s – Transfer length

M – Flexural moment

M_s – Flexural moment caused by N_f

M_{qpc} – Flexural moment caused by quasi-permanent load combination

N_{cr} – Cracking force of concrete

N_f – Fixation force

N_{Rest} – Restraint force

N_s – Axial force caused by N_f

Q – Cement heat generation rate

R – Ideal gas constant

T – Temperature

T_{env} – Temperature of environment

W – Total water concentration

List of Latin Lower-Case Letters:

a – Degree of restraint

b – Cross-section width

c – Specific heat

d_t – Depth of top reinforcement

d_b – Depth of bottom reinforcement

f_c – Compressive strength of concrete

$f_{c,cube}$ – Cube compressive strength of concrete

f_{ct} – Tensile strength of concrete

$f_{ct,fl}$ – Flexural tensile strength of concrete

$f_{ct,sp}$ – Splitting tensile strength of concrete

$f_{ct,w}$ - Weighted tensile strength of concrete

f_{ys} – Yield stress of steel

g – Permanent load

g_1 – Additional permanent load

h – Cross-section height

h_c – Convection coefficient

h_{cr} – Convection-radiation coefficient

h_m – Boundary transfer coefficient

h_r – Radiation coefficient

k – thermal conductivity

k_h - Coefficient of homogenization in concrete

p – Distributed load

P_{qpc} – Distributed load for quasi-permanent load combination

q – Live load

q_h – Heat flux

q_m – Moisture flux

t – Time

t_i – Concrete age at beginning of drying

t_0 – Loading age

w – Crack width

w/c – Water to cement ratio

x – Spatial coordinate

x_{na} – Position of neutral axis

x_{cr} – Position of crack tip

y – Spatial coordinate

z – Spatial coordinate

List of Greek Upper-Case Letters:

$\Delta\varepsilon_{G,sh}$ – Variation of axial strain at mid-height due to dry shrinkage

Φ – Curvature

List of Greek Lower-Case Letters:

α_c – Coefficient of thermal expansion of concrete

α_{fl} – Conversion facto for flexural tensile strength

α_s – Coefficient of thermal expansion of steel

α_{sp} – Conversion factor for splitting tensile strength

α_T – Degree of heat development

β – Tension stiffening parameter

δ_{slab} – vertical displacement of the slab

ε_{cr} – Crack strain

ε_G – Axial strain at mid-height

ε_s – Reinforcement strain

ε_{sh} – Concrete shrinkage strain

$\varepsilon_{sh,ult}$ – Ultimate shrinkage strain (upon total drying)

μ – Kelvin unit number

$\overline{v_t}$ – Position of centre of gravity of homogenised cross-section

ξ – Reduction coefficient for calculation of N_{Rest}

ρ – Mass density

ρ_s – Reinforcement ratio

$\rho_{s,eff}$ – Reinforcement ratio in effective area of concrete

σ_c – Concrete stress

σ_s – Reinforcement stress

$\sigma_{s,crack}$ – Maximum steel stress at crack cross-section

$\sigma_{s,average}$ – Average steel stress over transfer length

τ_μ – Retardation time of Kelvin unit μ

χ – Aging factor

ψ_2 – reduction factor for live loads in quasi-permanent load combination

List of Acronyms

AAEM – Age adjusted Elastic Method

AASHTO – American Society of State Highway and Transportation Officials.

AFR – After formwork removal

ARF – Adjustable Restraint Frame

ASTM – American Society for Testing Materials

BFR – Before formwork removal

CAD – Computer Aided Design

EC - Eurocode

FE – Finite Element

FEM – Finite Element Method

FBG – Fibre Bragg Grating

LVDT – Linear Variable Differential Transformer

MC10 – Model Code 2010

MS – Mechanical simulation

RC – Reinforced Concrete

RH – Relative Humidity

SHS – Square Hollow Section

SLS – Service Limit State

T - Temperture

THMS – Thermo-hygro-mechanical simulation

TMS – Thermo-mechanical simulation

TSTM – Temperature Stress Testing Machine

ULS – Ultimate Limit State

VRF – Variable Restraint Frame

VWSG – Vibrating Wire Strain Gage

XPS – Extruded Polystyrene

List of Figures

List of Tables

Chapter 1

Introduction

1.1 General Remarks

After setting, the reduction of water in concrete pores induces a volumetric contraction that is defined as drying shrinkage, when it occurs due to evaporation, and autogenous shrinkage, when it occurs due to internal consumption during the cement hydration process [1]. This contraction only occurs in the cement paste, being partially restrained by the aggregates [1,2] and reinforcement, in case of RC. In concrete buildings the axial shortening of solid RC slabs due to shrinkage is normally also restrained by their interaction with the bracing system (namely building cores), shear walls, soil retaining walls and foundations. As a consequence, axial forces develop on the slabs, with implications on: (i) the serviceability performance of the slabs in terms of steel stresses, crack widths and deformations [3]; (ii) the serviceability behaviour of bracing systems, which are subjected to horizontal forces transmitted by the floors [4]. Besides, in jointless RC structures the overall axial shortening of the slabs has to be limited, to avoid damages in cladding systems and partition walls – this limitation refers to the relative movements between adjacent floors [4].

Despite the relevance of the above-mentioned effects, the technical and scientific knowledge about the structural behaviour of RC slabs subjected to the combined effect of restrained shrinkage and applied loads is still limited up to this date. Current design recommendations [5–10] do not provide specific instructions regarding the methodology to adopt when designing such structures and the effects of restrained deformations and applied loads are addressed separately. For instance, Eurocode 2 (EC2) [6], provides a general expression for quantification of the crack width on RC elements subjected to external loads, allowing to neglect the effect of imposed deformations (if joints are incorporated at every 30 m), and direct quantification of the resulting restraint forces are not pursued further. In Eurocode 2 Part 3 [7], an alternative method is proposed to quantify the crack width due to restrained deformations along the edge or at the ends of RC members, but the effects of applied loads are not addressed in that approach. This gap in actual codes can either lead to very conservative solutions, when the design is based on taking the axial cracking force, or to inadequate service life behaviour of RC structures, even when code specifications are strictly respected [11,12].

Over the last years several authors have tackled this problem by applying non-linear numerical and analytical methods to study the structural behaviour of RC elements subjected to superimposition of bending and restrained deformations [13–20]. Regardless of the analysis complexity, there is a consensus that: (i) the internal axial forces caused by restrained deformations cannot be neglected; (ii) in

slabs subjected to the combined effects of bending and restrained shrinkage deformations the internal axial forces are smaller than in members subjected to end-restrained deformations only.

The above-mentioned studies are of paramount importance to understand the stress development and crack inducing mechanism on RC structures subjected to these combined effects. However, it is worth mentioning that in these works some simplified assumptions were considered, and the self-induced stresses due to heat of hydration and non-uniformity of drying shrinkage were neglected. Due to the exothermic nature of cement hydration reaction, concrete elements are subjected to a non-uniform distribution of temperatures during concrete curing, since temperatures are normally higher on the core and lower near the surfaces in contact with the air. Regarding the effect of drying shrinkage, it is normal practice to consider a uniform shrinkage strain field in concrete elements to determine the corresponding stresses caused by external restraint to deformation. Indeed, the restraint of the volumetric deformations associated to the temperature fields and the non-uniformity of deformations within the thickness of concrete elements induce stresses in concrete that are usually not taken into account in an integrated way [21].

Moreover, the employed modelling strategies (such as the cracking models and their interaction with creep and shrinkage) are still lacking experimental validation of the complex interplay with long-term real-scale experiments. In fact, the study of cracking and stress development in RC elements subjected to self-imposed deformations, with corresponding validation at structural scale, is currently limited to tests on specimens merely restrained by their own reinforcement and subjected to bending [22,23], or longitudinally restrained specimens without bending or shear stresses induced by external loads [24–30].

The present work intends to fill the aforementioned gap in the literature. It proposes a test setup for simultaneous application of axial restraint and vertical loads to slab-like specimens and presents the procedures and results of the long-term experimental campaign. The experimental programme includes the testing of restrained and unrestrained specimens (with different levels of vertical loading) and further characterization of the concrete, to support simulation models with different levels of complexity. A multi-physics simulation framework is calibrated/validated with the results from the experimental campaign and compared with simplified approaches. The findings from both experimental and numerical analyses should enable a better understanding of the complex interaction that occur between self-imposed deformations, viscoelasticity and flexural cracking, contributing to safer, yet cost-effective design of RC of elements subjected to the aforementioned combination of effects.

1.2 Motivation

The practical interest of further investigating the combined effect of restrained deformations and external loads in RC slabs in the scope of structural design was demonstrated in the previous sub-chapter. It contributes to more efficient control of cracking in restrained RC structures under service loading and, consequently, to proper service life behaviour during their life span, without excessive maintenance costs. The importance of restrained deformations in the service life behaviour of RC structures has been growing over the last years. One of the reasons is the increased use of high strength concrete, which demands the use of higher cement quantities, leading to higher thermal deformations at early ages. Another reason is the shortage of fly-ash in some countries, such as Portugal (where the partial cement replacement with fly-ash has been common practice since the 1990's), as explained in the following paragraph.

The advantages of partially replacing Portland cement with fly-ash, which comes from burning coal to produce electricity, are known: (i) cheaper and more sustainable production of concrete due to the reduction in the amount of cement required for a given strength class [31,32]; (ii) increased workability of the concrete and reduced water-to-cement ratio (w/c) required for a given slump class [31,33]; (iii) reduction of heat generated during hydration of the concrete cement [31,32]; (iv) increased durability of concrete due to increased resistance to sulphates, control of the alkali-silica reaction, decreased diffusion of chlorides and decreased leaching and efflorescence [31]. Even though the addition of fly-ash in concrete composition does not directly affect the hygro-thermal behaviour of concrete [31], the reduction of relative quantity of cement paste in concrete and the reduction of w/c in the mixture results in the decrease of concrete shrinkage at long term, as observed in several studies [1,34–38].

With the closure of coal-based thermoelectric power stations, and the consequent end of fly-ash, which was abundantly available in the Portuguese market, ready-mixed concrete tends to be manufactured (given the lack of a substitute product in the current scenario) with cement only. This is reflected in a considerable increase in the amount of cement required for the production of concrete and the consequent need to adopt measures that mitigate the adverse effects associated with increased heat of hydration and shrinkage.

1.3 Description of Thesis Content

In Chapter 1, a general framework of this dissertation, the author's motivations for choosing the theme of the thesis and the description of its content are presented.

In Chapter 2, the two main topics addressed in this work are introduced. Firstly, the main experimental techniques, reported in current literature, for testing concrete under restrained deformation are resumed.

Then, a multi-physics framework based on the FE method for analysis of the thermo-hygro-mechanical behaviour of RC structures, in which self-induced stressed caused by non-uniform distribution of moisture and temperature are considered, is presented.

Chapter 3 presents the long-term experimental campaign undertaken for simulating the combined effects of restrained shrinkage and vertical loads on RC slabs. The overall strategy, the test setup and results are fully addressed in this chapter.

In Chapter 4, the numerical simulation of the structural behaviour of the slabs that were tested in the experimental campaign performed in this thesis, and presented in Chapter 3, is presented with the multi-physics framework addressed in Chapter 2. A simplified approach based on compatibility of deformations for calculation of the restraint force is proposed, and estimates regarding tested restrained slabs are compared with the experimental data.

In Chapter 5, a representative case study of a thin fully restrained solid slab is presented, being analysed with the multi-physics framework addressed in Chapter 2 and validated in Chapter 4. The analysis with the multi-physics framework is compared against simplified approaches with different levels of complexity. Finally, a parametric study on the influence of the reinforcement ratio, calculated for different design strategies, is performed.

Chapter 7 draws the main conclusions and contributions of the work carried out, as well as some suggestions for future developments.

Chapter 8 presents the references used to support all decisions and the methodology used in this study.

Chapter 2

Restrained deformations in RC structures: experimental and numerical approaches

2.1 Introduction

Concrete is subjected to volumetric changes because of its intrinsic properties (chemical, autogenous and thermal shrinkage), as well as environmental factors such as ambient temperature and moisture [39]. Even though the restriction of these imposed deformations causes axial forces that may become important to the design of both the restrained element and the restraining component, the determination of these forces is not trivial due to four reasons, as listed by Schlicke *et al.* [20]: (i) the quantification of the imposed deformation itself is subject to a complex time-dependent thermo-hygro-chemo-mechanical behaviour of the concrete; (ii) the axial deformation of the slab which interacts with the external restraining condition is partly reduced by internal restraint [40,41]; (iii) the external restraining condition of the slab is affected by the global stiffness of the bracing system, as well as by the local stiffness of the connection of the slab and the bracing system [42]; and (iv) the finally occurring restraint forces are strongly subjected (and reduced) by the released axial deformation due to bending cracking of the slabs under service loads.

Given the complexity of the many phenomena involved, experimental and numerical simulations of concrete and RC elements subjected to restrained deformations are essential to better predict the structural behaviour of real-life structures under similar conditions and to optimize the design of reinforcement in RC elements. In that regard, both experimental and numerical approaches are addressed in the present chapter.

A summary of the main experimental techniques for simulation of structural behaviour of concrete and RC elements under restrained shrinkage is presented in sub-chapter 2.2, and the long-term experimental campaign presented in Chapter 3 for simulation of a RC slab subjected to the combined effect of restrained shrinkage and service life vertical loads is contextualized in light of the current state-of-the-art.

In sub-chapter 2.3, the FE based multi-physics approach employed in Chapters 4 and 5 for simulation of the experimental campaign presented in Chapter 3 and the case study of a fully restrained solid slab, respectively, is described.

2.2 Experimental approach for analysis of restrained concrete

This section intends to present some of the experimental techniques, addressed in the existing literature, that may be implemented to study the complex interplay that exists between cracking, viscoelasticity and imposed deformations in restrained concrete elements.

As pointed by Kanavaris *et al.* [43], given the complexity of mechanisms involved on the restrained behaviour of concrete elements, there is not a single unified experimental system that is capable to account for all phenomena holistically. Therefore, each experimental setup is built to obtain different information, with different complexities, ranging between qualitative assessment of cracking potential under specific ambient conditions and characterization of mechanical and viscoelastic properties as affected by thermal and hygrometric effects.

According to Bentur and Kovler [44] the experimental restraining devices can be classified into four distinct categories: ring tests, panel tests, substrate restrained tests and longitudinal tests, as described in the following sections.

2.2.1 Ring tests

The ring test has been widely used over the last decades, and its original setup dates back to the late 1930's [44,45]. It consists in casting a concrete ring around a restraining core (usually made up of steel) that prevents its shrinkage, causing the development of tensile circumferential stresses on the concrete ring (Fig. 2.1) that may lead to cracking.

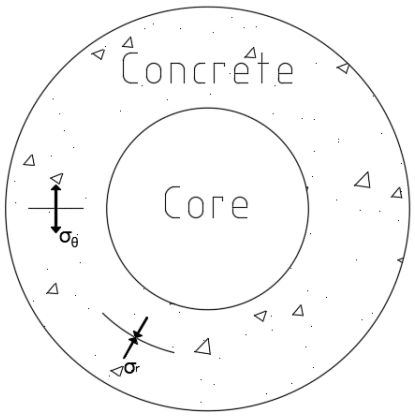

Figure 2.1 – Schematic representation of the ring test. Adapted from Bentur and Kovler [44].

Conventionally, the ring test has been considered as a qualitative technique for assessment of plastic shrinkage cracking and shrinkage cracking of hardened concrete, in which the evaluation of performance is based on characterization of cracks and their quantification regarding maximum and average width, number and time of occurrence [44,45]. However, induced restraint stresses in concrete may be estimated based on analytical approaches, which require either additional testing for assessment of free shrinkage and elastic modulus of the tested concrete [46–52] or monitoring of steel ring strains induced by concrete shrinkage [46,52–55].

Given the applicability of the ring test for assessment of cracking behaviour of concrete with different compositions (as to analyse the influence of specific additives, aggregates, fibres, etc.), it has been standardized by the American Association of State Highway and Transportation Officials (AASHTO) [56] and by the American Society for Testing Materials (ASTM) [57].

2.2.2 Plate tests

The plate test was developed and is mainly used for evaluation of concrete performance regarding plastic shrinkage cracking [58–64]. The test procedure consists in casting concrete in a square slab mould with reinforcement at the edges of the plate to induce restraint. Plastic shrinkage may be accelerated with hot hair blown from a fan (Fig. 2.2), and the performance of the concrete is quantified by measuring the crack widths, the total crack length, the crack area (crack width multiplied by its length) and the number of cracks per unit area [44].

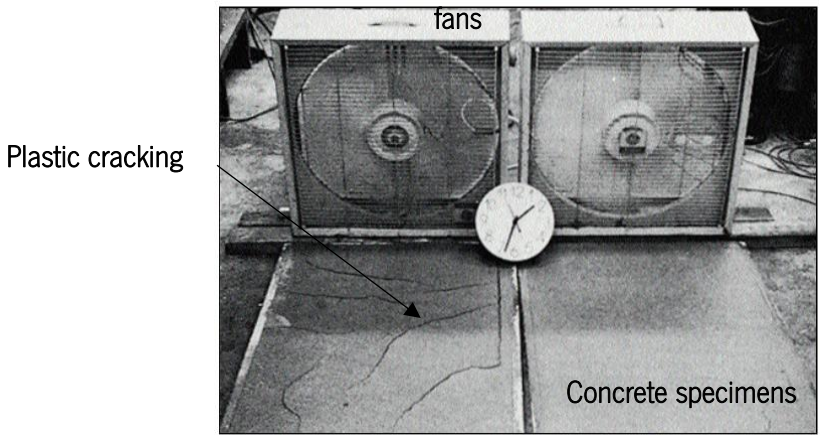

Figure 2.2 – Illustration of two plate test panels. Adapted from Kraii [61].

2.2.3 Substrate restrained tests

The substrate restrained tests were developed to simulate the restraining condition of pavements, induced by the substrate. According to Bentur and Kovler [44], it can be classified into two categories, depending on the object of study: cracking or curling. Different substrate retrained tests were developed and implemented over the last decades [65–71], being the most prominent ones presented in the following paragraphs.

Banthia *et al.* [65] developed a test in which the restraining substrate is previously cast in a mould and its surface is roughened manually with the application of aggregates on the top surface of the fresh concrete, followed by a curing in a 50°C water bath for 3 days. The second phase of casting is followed by a curing process in a climatic chamber with a constant temperature (T) of 38°C and relative humidity

(RH) of 50%, and with circulation of hot air to accelerate the drying shrinkage process (Fig. 2.3). This test allows to simulate the cracking pattern due to shrinkage that occurs in applications such as repair or resurfacing.

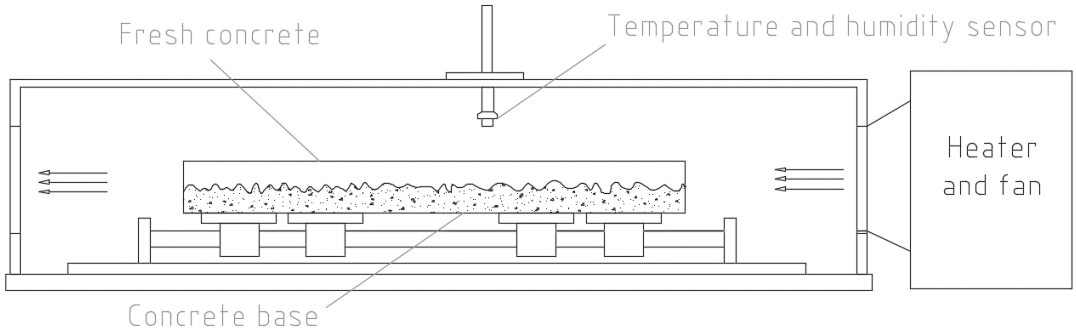

Figure 2.3 – Schematic representation of substrate restrained test for assessment of cracking. Adapted from Banthia *et al.* [65].

A test based on concrete curvature was developed by the Structural Preservation System, Inc. in order to evaluate the behaviour of repair systems [70]. The test consists of casting a cementitious material layer on a steel plate, coated with epoxy and sand grit to assure bonding between the two materials. One end of the specimen is gripped into a frame, while the other is free (Fig. 2.4), enabling the measurement of the relative displacement of the two extremities and calculate the element curvature.

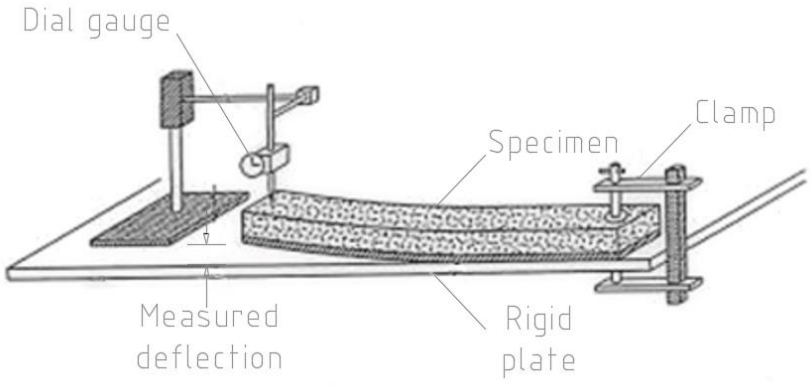

Figure 2.4 - Schematic representation of substrate restrained test for assessment of curling. Adapted from Vaysburd *et al.* [70].

2.2.4 Longitudinal restrained tests

According to Kanavaris *et al.* [43], longitudinal restrained tests can be divided in four main categories: (i) the longitudinal-qualitative test, where the longitudinal geometry is used as a restraint to measure crack widths; (ii) the longitudinal-passive test, in which the restraint is achieved by longitudinal bars, where strain gauges are mounted to determine the restraining forces and stresses; (iii) the longitudinal-active, in which the position of the grip is adjusted to keep the deformation close to zero (or close to it), while

measuring the load in the grip and (iv) the longitudinal combined test, which intend to simulate the interplay of restrained deformations originated from the material itself with further external actions, such as external imposed deformations or loads.

Examples of each type of longitudinal restrained test are presented in the following paragraphs.

2.2.4.1 Longitudinal-qualitative tests

Longitudinal-qualitative restrained tests are mainly used for evaluation of performance of fibre reinforced concrete mixtures regarding restrained shrinkage cracking [72–74].

An example of a longitudinal restraining rig for evaluation of cracking is the one presented in Fig. 2.5, proposed by Banthia *et al.* [72,73], in which the restraint of the concrete specimen is generated by end grips. The specimen is cast into a mould with embedded bar anchors at their ends, which are rigidly connected to the base of a rigid frame through vertical posts. These end anchors are the only source of restraint to the specimen, as the mould itself is mounted on two frictionless rollers that are free to slide along two horizontal slide rails. Concrete specimens are mounted on this assembly after formwork removal and subjected to an environmental T of 50°C and RH of 50%. The total crack width and cracked length are measured and used as parameters to characterize the cracking behaviour and compare different compositions.

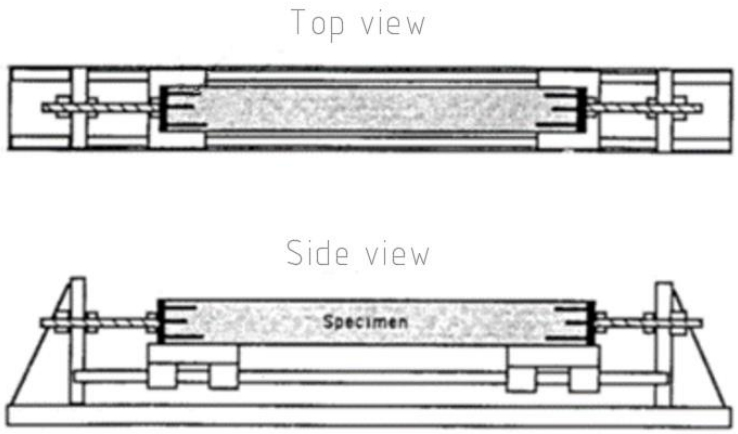

Figure 2.5 - Schematic representation of longitudinal-qualitative restrained test setup. Adapted from Banthia *et al.* [72].

2.2.4.2 Longitudinal-passive tests

The longitudinal passive tests are based on the *Rigid Cracking Frame* (RCF) developed in the Technical University of Munich in the late 1960's [75]. This method emerged as an attempt to quantify the effects of thermal stresses on early age behaviour of concretes subjected to adiabatic conditions. This

mechanism was adopted by RILEM in 1997 as a recommendation test method [76], encouraging its broader use for studies on the influence of concrete composition in its thermal cracking risk [77–82].

A schematic representation of the test setup is shown in Fig. 2.6. It consists of a dog-bone shaped concrete specimen casted and restrained by two massive steel bars, usually made from Invar steel in order to minimize deformations due to ambient temperature variations. The steel bars are instrumented with strain gauges for measurement of small strains that are not restrained, and the restraint stresses are calculated from the strain data and cross section areas. The test setup enables the accommodation of both compressive and tensile restraint stresses, which occur during heat and cooling periods, respectively. Quasi-adiabatic conditions are ensured with a thermally insulating formwork (made of polystyrene) and the temperature of the test specimen is controlled by copper pipes embedded in the formwork for circulation of water at the desired T. The stress development curves, the zero-stress temperature (at which the compressive stress induced during heating is reduced back to zero) and the cracking temperature (in the cooling phase at which cracking occurs) are measured and used as parameters to characterize the thermal behaviour of concrete at early ages [44].

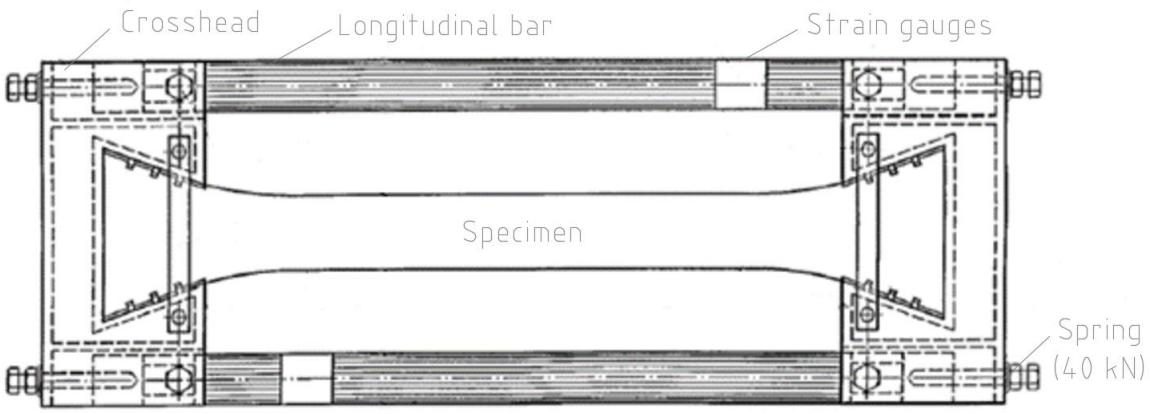

Figure 2.6 - Schematic representation of longitudinal-passive restrained test setup. Adapted from RILEM [76].

Different versions of the longitudinal-passive test, in which a dog-bone specimen is restrained by a rigid frame, have been used over the last decades, weather for assessment of thermal induced stresses in mass concrete [83,84], monitorization of early-age cracking in fibre reinforced mortars using acoustic emission [85], assessment of drying shrinkage cracking potential of concrete [86–91] or assessment of post-restrained properties of concrete [92–94].

2.2.4.3 Longitudinal-active tests

The stresses developed in the longitudinal-passive rigs described in the previous section are influenced by the ratio between the rigidity of concrete and of the restraining frame. Longitudinal-active restraining rigs were therefore developed in order to achieve full restraint of the concrete specimens under investigation, regardless of the rigidity of the testing rig. The active modified rig consists of two grips, in which one is fixed and the other one is free to move, returning to its original position after some deformation occurred. This may be achieved manually or automatically by activation of a screw or a hydraulic mechanism to bring back the grip to the initial position. The restraint load is measured with a load cell [44].

The mounting of the specimen on the longitudinal-active rigs can either be horizontal or vertical. The former one enables the measurement immediately after casting, whereas the latter one is only adequate for measurement in hardened concrete.

An horizontal longitudinal-active restrained test was firstly reported by Springenschmid *et al.* [95] in the early 1990's, as an improvement to the RCF setup proposed by RILEM [76] to evaluate the cracking propensity of concretes with different compositions under adiabatic conditions. Given its original application, this test setup has become known as the Temperature Stress Testing Machine (TSTM).

As pointed by Kanavaris *et al.* [43], the original TSTM apparatus, with similar operating principles and test setup configurations, was adopted by several authors worldwide [96–100], contributing to the wideness of investigations regarding early age viscoelastic behaviour of concrete. The original TSTM apparatus was also improved over the last decades in order to overcome the pre-existing limitations.

A closed-loop system for the TSTM was developed by Kovler [24,101] in 1994, where the control of the grip displacement consists in an automatic compensation of the deformation registered in two specimens, one free to deform and the other restrained. Based on a predetermined criterion, different levels of restriction can be imposed with the activation of a step motor that imposes a tensile force on the restrained specimen (Fig. 2.7). Since this test minimize human intervention, it provided results with enough precision to evaluate creep deformations on concrete specimens.

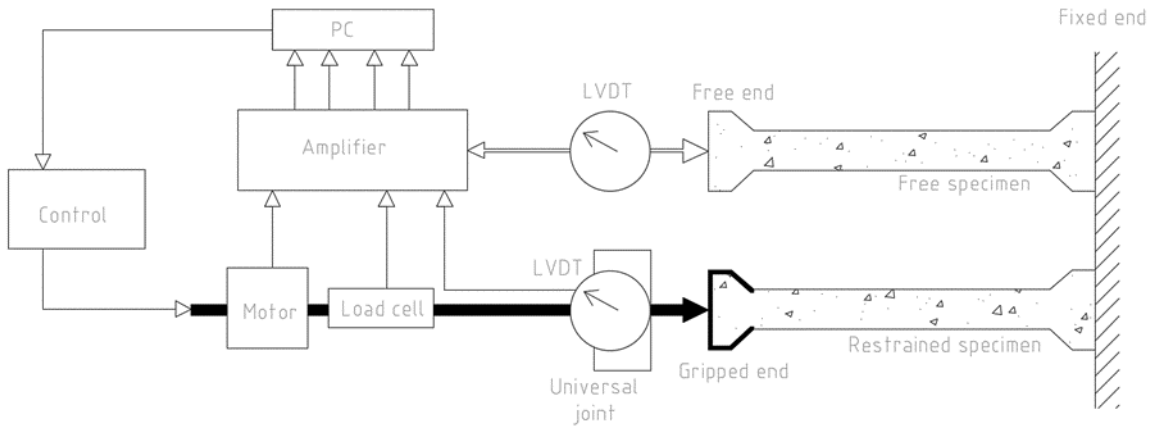

Figure 2.7 - Schematic representation of the closed-loop restrained system developed by Kovler [24]. Adapted from Kovler *et al.* [101].

Neto *et al.* [102] and Delsaute *et al.* [103] presented some modifications of the TSTM to ensure an adequate control over the specimen's temperature and isolate effects of shrinkage and temperature. The former developed a system where the temperature is controlled with a thermic bath on both specimens, and the latter with liquid circulation on zinc moulds that embrace the specimens.

In order to enable the testing of relatively large-sized reinforced high-performance concrete specimens under realistic thermal conditions, and varying degrees of restraint, Cusson and Hoogeveen [25] proposed a test rig, known as Variable Restraint Frame (VRF), where the restriction is accomplished by applying a tensile force to the steel reinforcement of the specimen with a hydraulic actuator (Fig. 2.8).

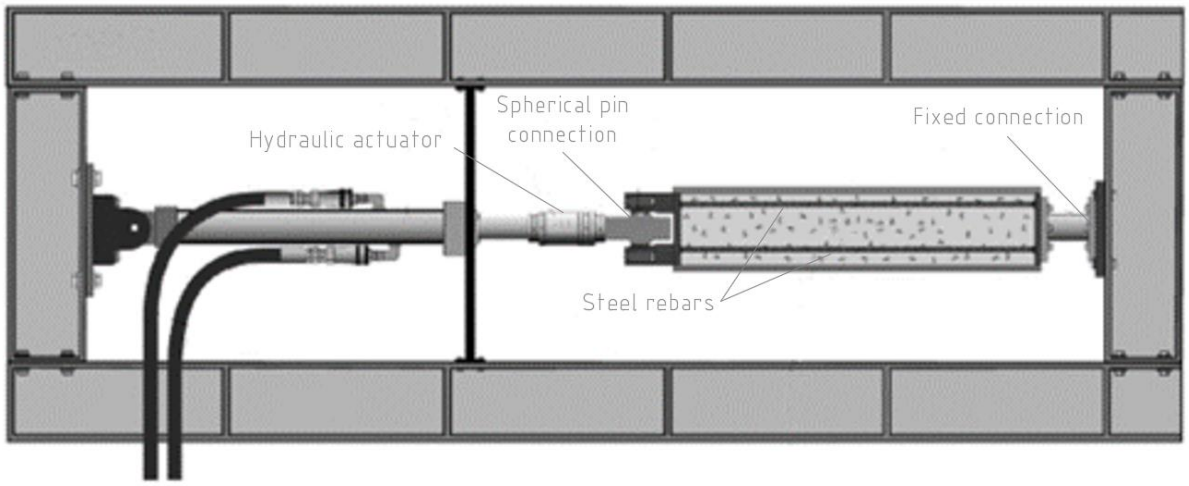

Figure 2.8 - Schematic representation of the VRF system developed by Cusson and Hoogeveen [25]. Adapted from Cusson and Hoogeveen [25].

Faria *et al.* [26] presented a VRF testing system, based on the original idea of Cusson and Hoogeveen [25], that enables the measurement of concrete tensile creep strain. The testing device uses two concrete specimens of the same batch and with equal cross-section: one is unrestrained and allow the measurement of the free shrinkage ("dummy"); the other is the restrained test specimen. The restrained

specimen has two steel rods embedded in concrete, threaded for the use of nuts that fix stiff plates at the rod extremities, to anchor the hydraulic jacks that transmit the tensile forces to the specimen (Fig. 2.9). Compared to the VRF proposed originally by Cusson and Hoogeveen [25], this system allows a uniform drying around all surfaces, as required when drying shrinkage is of relevance, and both dummy and restrained specimens are cured under the same exact T and RH conditions to ensure that free shrinkage measured on the dummy is representative of the volumetric changes that would be expected on the test specimen if it was not restrained.

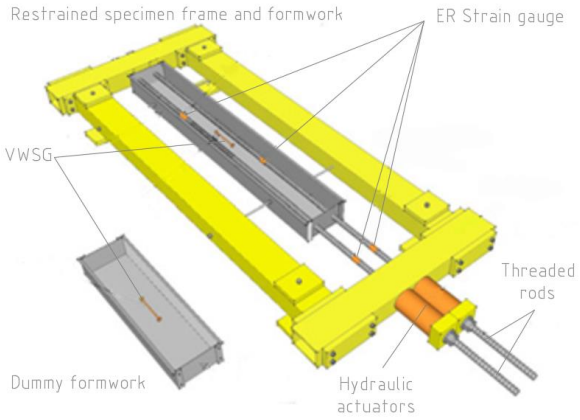

Figure 2.9 - Schematic representation of the VRF system developed by Faria *et al.* [26]. Adapted from Faria *et al.* [26].

The VRF systems proposed by Cusson and Hoogeveen [25] and Faria *et al.* [26] allow the restraint level to be adjusted during the test, and a smooth tensile strain field is induced in the restrained specimen due to the threads over the entire length of the two steel rods, improving the bond with the concrete. In addition, the test is able to proceed even if the restrained specimen cracks.

2.2.4.4 Longitudinal-combined tests

Longitudinal-combined tests are based on longitudinal restrained tests but designed to simulate the combined effects of restrained self-induced deformation with further external actions such as externally imposed loads or strains.

These tests are suitable for macro simulation of the structural behaviour of concrete elements, instead of the material behaviour itself. Test specimens are reinforced and the experiment is conducted beyond cracking. The structural behaviour may be monitored since casting, and tests are able to account for the early age thermal and autogenous deformations, as well as bulk drying shrinkage, in combination with the deformations imposed by external actions, enabling the investigation of crack width opening in RC elements under realistic loading scenarios [43].

There are currently two test setup proposals with such features: (i) the adjustable restraining frame (ARF) for testing the interplay of early age restraint with imposed deformations during service life, developed at Graz University of Technology [104–106], and (ii) the restraint frame for testing the combined effect of axial restraint and bending due to loading, developed at University of Minho [107–109]. The latter will be presented in detail in Chapter 3, as the experimental simulation of the combined effect of axial restraint and bending due to loading is part of the objectives of this thesis. The former is presented in the following paragraphs.

A schematic representation of the experimental setup of Graz University of Technology is shown in Fig. 2.10. It consists of a massive steel frame which restrains a 25×25cm² RC tie.

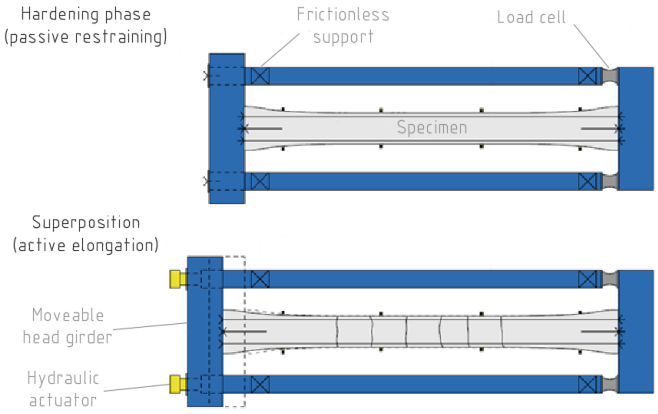

Figure 2.10 - Schematic representation of the ARF system developed at Graz University of Technology. Adapted from Schlicke *et al.* [106].

The test is divided in two phases: (i) hardening phase, when the stresses induced by cement hydration are simulated and (ii) superposition phase, when the resulting stresses and cracking from the hydration process are combined with additional stresses due to imposed deformations that are representative of service life conditions.

During the first phase, the restraining condition is passive (fully restrained), without any external control, and the specimen is covered with thermal insulation to simulate a temperature history due to heat of hydration that is representative of a member thickness of more than 1m. After the hardening phase, additional deformations representative of service life loading are imposed to the concrete tie, decreasing the degree of restraint (extent to which concrete is prevented from deforming), without affecting the already existing stresses due to heat of hydration.

2.3 Numerical approach: multi-physics framework

The FE based multi-physics simulation framework to be employed in Chapters 4 and 5 of this thesis was proposed by Azenha [110], and it was cumulatively implemented and validated over the last years [21,111]. The method consists of a staggered simulation in which the temperature T, the RH and the mechanical fields are computed sequentially, with transition of information from thermal and moisture models to the mechanical model, as shown in the schematic representation in Fig. 2.11.

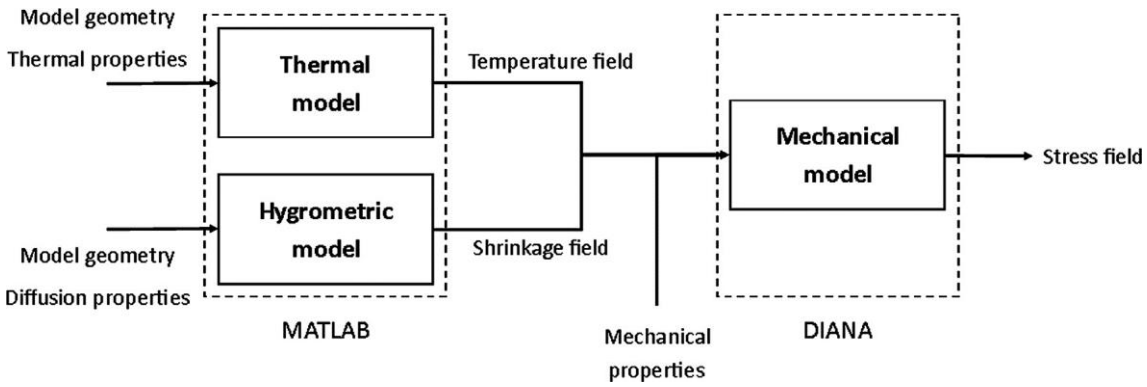

Figure 2.11 - Global overview of the thermo-hygro-mechanical simulation framework [110].

The thermal and hygrometric models are solved prior to the mechanical model with an in-house developed 3D Finite Element Method (FEM) software [110], coded in MATLAB®. The FE mesh is composed by solid elements (with nodes coincident with the ones of the mechanical FE mesh), as well as by surface elements to account for the fluxes, normal to the defined boundaries. The temperatures, determined from the thermal model, are directly input in the nodes of the mechanical model, whereas the infinitesimal shrinkage field, calculated from the moisture model (based on the internal RH, assumed as the driving force), is transformed into a fictitious temperature field based on a constant value of the coefficient of thermal expansion of the concrete α_c. The mechanical model is computed using the FEM package DIANA 10.4 [112], taking into account the mechanical properties of the materials as well as the imposed strains, directly computed from the T and RH fields obtained for the previous thermal-hygrometric simulation.

The governing equations of the thermal and hygrometric simulations are briefly described in sub-chapters 2.3.1 and 2.3.2, respectively, whereas a detailed presentation of the thermo-hygrometric model can be found in [110]. The main modelling strategies adopted in the mechanical simulation are presented in sub-chapter 2.3.3.

2.3.1 Thermal model

The energy balance for computing the transient temperature field is expressed by the following equation [113]:

$$\frac{\partial}{\partial x}\left(k\frac{\partial T}{\partial x}\right)+\frac{\partial}{\partial y}\left(k\frac{\partial T}{\partial y}\right)+\frac{\partial}{\partial z}\left(k\frac{\partial T}{\partial z}\right)+\dot{Q}=\rho c\frac{\partial T}{\partial t} \quad \text{(Eq. 2.1)}$$

where T is the temperature (°C), c is the specific heat of the material (J.kg^{-1}.°C^{-1}), ρ is the mass density (kg.m^{-3}), $\dot{Q}$ is the cement heat generation rate (W.m^{-3}), k is the thermal conductivity of concrete (W.m^{-1}.°C^{-1}) assumed constant throughout the period of analysis, and x, y and z are the spatial coordinates (m). The cement heat generation rate $\dot{Q}$ is accessed experimentally by calorimetric testing, and can be expressed through an Arrhenius-type function based on the degree of heat development α_T [110,114]:

$$\dot{Q}=f(\alpha_T)A_T e^{\frac{E_a}{RT}} \quad \text{(Eq. 2.2)}$$

where α_T is the degree of heat development (normalized degree of hydration established as a function of the total generated heat), $f(\alpha_T)$ is the normalized heat generation function, A_T is a rate constant, R is the ideal gas constant (8.314 J.mol^{-1}. °C^{-1}) and E_a is the apparent activation energy (J.mol^{-1}).

The heat transfer between the concrete surface and the surrounding environment is expressed with a Neumann-type formulation that includes a lumped convection-radiation coefficient h_{cr} [110,115]:

$$q_h=h_{cr}\cdot(T-T_{env}) \quad \text{(Eq. 2.3)}$$

$$h_{cr}=h_c+h_r \quad \text{(Eq. 2.4)}$$

where q_h is the heat flux (W.m^{-2}) through a boundary at temperature T (°C), T_{env} is the environmental temperature (°C), h_c is the convection coefficient and h_r is the radiation coefficient (W.m^{-2}.°C^{-1}). When the concrete surface is covered by another material (e.g. formwork), the value of h_{cr} can be adjusted using an electrical analogy, detailed in the works of Azenha [110] and Jonasson [115].

2.3.2 Hygrometric model

The RH field inside the concrete pores is modelled with a macroscale approach, in which the moisture transport is simulated through a diffusion-type equation, considering the internal RH as the driving potential. The adopted field equation for characterizing the moisture diffusion in concrete follows a similar approach to the one proposed in Model Code 2010 [10]:

$$\frac{\partial RH}{\partial t}=\left(\frac{dW}{dRH}\right)^{-1}div\left(D_H\,grad(RH)\right)+\frac{\partial H_s}{\partial t} \quad \text{(Eq. 2.5)}$$

where $\left(\frac{dW}{dH}\right)^{-1}$ is the moisture capacity, W is the total water concentration (kg.m^{-2}.s^{-1}), t is the time (s), D_H is the moisture diffusivity (m^2.s^{-1}), which is a function of RH, and $\frac{\partial H_s}{\partial t}$ is the internal change of RH due to self-desiccation.

Taking into account that the influence of internal water consumption due to chemical hydration reactions in the pores can be considered negligible for ordinary concrete (type 1 normal Portland cement and high values of w/c ratio) [116], and that the moisture capacity of cementitious materials at common environmental conditions (with a relative humidity above 50%) has been reported to be fairly constant [117], Eq. 2.5 can be simplified as:

$$\frac{\partial RH}{\partial t} = div\left(D_H \, grad(RH)\right) \qquad \text{(Eq. 2.6)}$$

The diffusion parameter D_H is determined according to a formulation proposed by Bažant and Najjar [118]:

$$D_{H^*} = D_1 \left[\alpha_H + \frac{1-\alpha_H}{1+\left[\frac{1-RH}{1-H_c}\right]^n}\right] \; with \; \alpha_H = \frac{D_0}{D_1} \qquad \text{(Eq. 2.7)}$$

where D_1 and D_0 (m^2.s^{-1}) are the values of D_H for $RH = 1$ and $RH = 0$, respectively, H_c is the relative humidity for which $D_H = 0.5D_1$ and n is a material property.

The boundary conditions for the moisture field in concrete are defined in a similar way to the ones in the thermal model. A Neumann-type approach is thus adopted as follows:

$$q_m = h_m \cdot \left(H_{surf} - H_{env}\right) \qquad \text{(Eq. 2.8)}$$

where q_m (m.s^{-1}) is the moisture flux between the concrete pores and the environment, h_m (m.s^{-1}) is the boundary transfer coefficient and H_{surf} and H_{env} are the values of RH on the surface and on the surrounding environment, respectively.

The internal humidity field within the FE mesh, computed by the hygrometric model, is then converted to an imposed drying shrinkage strain, defined according to the formulation proposed by Kwak *et al.* [119]:

$$\varepsilon_{sh} = \varepsilon_{sh,ult} \cdot [0.97 - 1.895 \cdot (RH - 0.2)^2] \qquad \text{(Eq. 2.9)}$$

where ε_{sh} is the shrinkage strain variation in the concrete for a given variation of humidity and $\varepsilon_{sh,ult}$ is the ultimate shrinkage of concrete upon total drying.

2.3.3 Mechanical model

The mechanical simulation follows a relatively standard approach for structural non-linear analysis in RC elements. The analysis includes the effect of imposed strains generated by the heat of hydration and drying shrinkage (calculated through the abovementioned thermal and hygrometric models), as well as the effect of the evolutionary mechanical properties of concrete, viscoelasticity and cracking. The creep and cracking models adopted in the mechanical simulation are descried in the following sections.

2.3.3.1 Creep model

The viscoelastic behaviour of concrete (elastic and creep deformations) is simulated through an ageing Kelvin chain, which associates in series a spring and N Kelvin units with stiffness E_μ and retardation times τ_μ. The mathematical expressions of the adopted rheological model are based on an adaptation of the Dirichlet series approximation of the Double Power Law [120] :

$$J(t,t_0) = \frac{1}{E_0(t_0)} + \sum_{\mu=1}^{N} \frac{1}{E_\mu(t_0)} \left[1 - e^{-\frac{(t-t_0)}{t_\mu}}\right] \qquad \text{(Eq. 2.10)}$$

$$\frac{1}{E_\mu(t_0)} = b \left(\frac{\tau_1}{0.002}\right)^n \frac{\varphi_1}{E_0(t_0)} 10^{n(N-1)} t_0^{-m} \qquad (\mu < N) \qquad \text{(Eq. 2.11)}$$

$$\frac{1}{E_N(t_0)} = 1.2b \left(\frac{\tau_1}{0.002}\right)^n \frac{\varphi_1}{E_0(t_0)} 10^{n(N-1)} t_0^{-m} \qquad (\mu = N) \qquad \text{(Eq. 2.12)}$$

where $E_0(t_0)$ is the asymptotic Young´s modulus of concrete (corresponding to short term loads) at the loading age t_0, and b, n, m and φ_1 are adjusting parameters to best fit the numerical to the experimental creep curves. The latter set of parameters is determined through a fitting procedure based on the least squared error method (LSM), in order to minimize the difference between the experimental values of the creep curve $J_{exp}(t_{j,i}, t_{0,i})$ and the values of the creep function $J(t_{j,i}, t_{0,i})$ determined with Eq. 2.10. The objective function of the LSM takes the form of:

$$Min \sum_{i=1}^{L} \sum_{j=1}^{M} \left[J(t_{j,i}, t_{0,i}) - J_{exp}(t_{j,i}, t_{0,i})\right]^2 \qquad \text{(Eq. 2.13)}$$

where $t_{o,i}$ correspond to the loading ages, $t_{j,i}$ are the time steps, L is the total number of loading ages to be fitted by the model and M is the number of discrete points of each creep function.

2.3.3.2 Cracking model

Concrete cracking is simulated with a smeared, multi-directional, fixed crack model with strain decomposition, in which the total strain is decomposed into stress-dependent and stress independent components, plus a crack strain vector [121].

For large-scale models of RC elements, consideration of perfect bond between concrete and reinforcement (average steel strains is equal to the average concrete strains) becomes appropriate and larger FEs may be used in 2D and 3D simulations [122]. For such modelling approach, the difference between the structural response of the RC member and the bare steel, designated as tension stiffening [123], should be simulated by means of constitutive models for concrete and steel that describe the stresses in each material averaged along the transfer length L_s [124].

The constitutive behaviour of the concrete (Fig. 2.12a) is defined by a diagram in which the concrete stress is expressed as a function of the strain normal to the crack ε_{cr}, in coherence with the stress–strain (Fig. 2.12b) and stress-crack opening (Fig. 2.12c) relations for concrete under uniaxial tension, as proposed by Model Code 10 (MC10) [10].

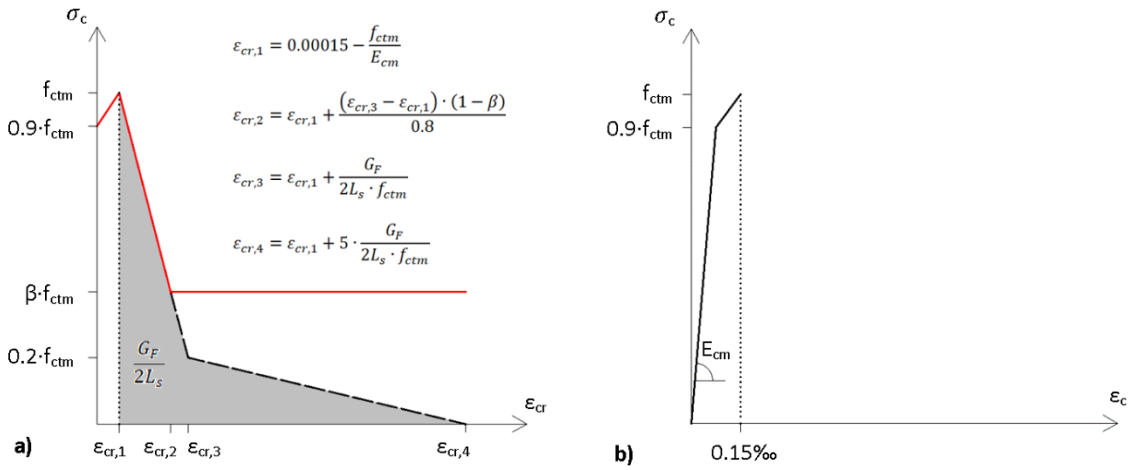

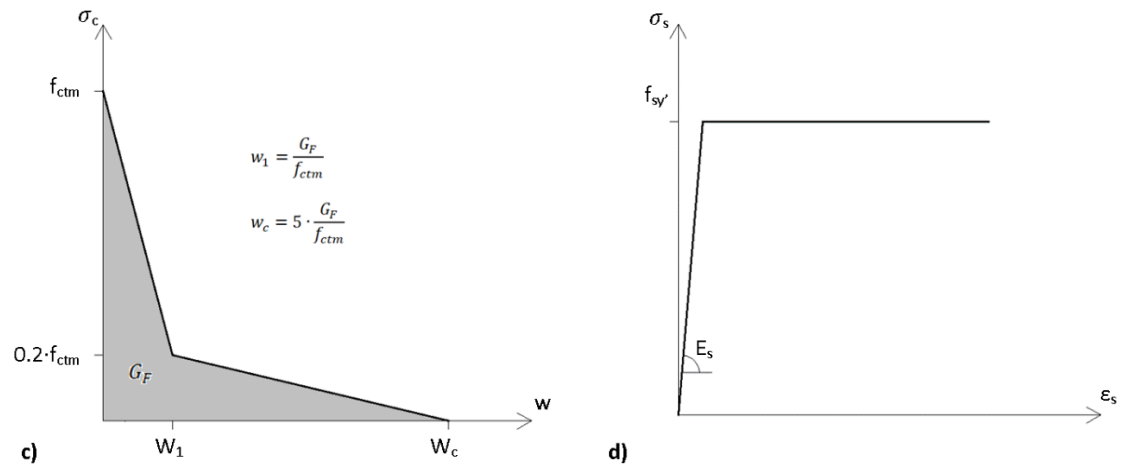

Figure 2.12 - a) Concrete stress-crack strain relation assumed for the crack model (red line); b) schematic representation of the stress–strain relation for uniaxial tension proposed by FIB [10]; c) schematic representation of the stress–crack opening relation for uniaxial tension proposed by FIB [10]; d) Steel stress-strain relation assumed for the crack model.

The ascending part of the diagram describes the stiffness decrease due to the formation of microcracks for stresses higher than $0.9f_{ctm}$, while the descending part describes the softening behaviour of the material. In this modelling approach, the fracture energy of concrete, G_F, is released throughout the length $2L_s$, simulating the released energy in the structure, in each crack, given that the estimated crack spacing is $2L_s$. The descending part of the diagram is therefore dependent on the crack spacing $2L_s$, not the crack bandwidth of the FE, because crack localization does not occur [125]. For higher crack strains, the average concrete stress normal to the crack is equal to βf_{ctm}, as recommended by Model Code 10 [10]. The variable β represents a tension stiffening parameter, which, for long-term analyses, can be considered constant and equal to 0.4 [10,124].

The steel reinforcement is modelled by truss FEs embedded in the concrete element. The constitutive model for the steel, shown in Fig. 2.12d, simulates an elastic-perfectly plastic behaviour. The limit of elasticity is reached when the steel stress at the crack section is equal to the yield stress of the reinforcement, $f_{sy} = 400MPa$. At that point, the average steel stress is $f_{sy'} = f_{sy} - \beta f_{ctm}/\rho_{s,eff}$ [124]. Variable $\rho_{s,eff}$ is the percentage of reinforcement in the effective area of concrete, $A_{c,eff}$, which in turn is quantified according to the MC10 [10]. Given the fact that steel yielding is thought to be avoided under the envisaged serviceability analyses, the steel behaviour after yielding is modelled in a simplified way, without a detailed description of strain hardening effects.

By using this tension stiffening modelling approach, the steel stress computed in the FE analyses is the stress averaged over the transfer length. The maximum steel stress, which occurs at the crack cross section, $\sigma_{s,crack}$, is given by:

$$\sigma_{s,crack} = \sigma_{s,average} + \frac{\beta f_{ctm}}{\rho_{s,eff}} \quad \text{(Eq. 4.6)}$$

The crack width is determined by integrating the distributed crack strain along the length $2L_s$, which corresponds to the crack spacing.

Chapter 3

Long-term experimental campaign

3.1 Introduction

This chapter presents a long-term experimental campaign for simulation of the combined effects of restrained shrinkage and vertical loads on RC slabs, performed on the scope of both this thesis and the FCT project "IntegraCrete: a multi-physics and multi-scale approach to the combined effects of applied loads and thermal/shrinkage deformations in reinforced concrete structures".

In this experimental campaign, a new method is applied, in which a restraining device is used to constrain the axial deformation of a slab-like specimen, while allowing it to simultaneously endure bending and shear stresses. The deformation is restrained by two hydraulic actuators connected to one of the slab extremities, allowing a progressive adjustment of the axial force installed whilst controlling the deformation on a pre-defined region (active restraint). The design of the restraining device was accomplished by the investigators of IntegraCrete project team (http://civil.uminho.pt/integracrete/). The author, as a research fellow in the aforementioned project, was responsible for planning and conduction of the experimental campaign.

The experimental program comprehends the long-term testing of slabs, in a controlled environment room, under four distinct situations by combining the two following conditions: (i) with or without restraint to axial deformations and (ii) with or without application of vertical loads. The structural behaviour of the slabs is continuously monitored over a period of 18 months, while several mechanical properties, as well as the internal RH of concrete, are assessed in complementary specimens from the same batch.

The overall strategy that was envisaged for this experimental program is explained in section 3.2. A detailed description of the test setup is performed in section 3.3, including the restraining device, test specimens and sensors. All the work concerning the preparation and conduction of the long-term experimental campaign is revealed in section 3.4. Finally, results regarding the structural behaviour of tested specimens and concrete characterization are presented in section 3.5 and discussed in section 3.6. Final considerations regarding the work presented in this chapter are drawn in section 3.7.

3.2 Experimental Method

The restraint axial force acting on a RC slab is directly influenced by its stiffness (which is considerably reduced after cracking), and by the axial load needed to form a new crack. When the restrained axial deformation is combined with vertical loading, the stiffness reduction is anticipated due to flexural cracking, and the axial load to form a new crack also decreases. In the latter scenario, the developed

axial restraint force is not only influenced by the degree of restraint, but also by the level of flexural cracking: under usual values of imposed axial deformation, higher levels of vertical loading result in smaller restraint axial forces [13,19,126,127].

In order to address these different scenarios, in terms of cracking and self-induced stresses, the long-term experimental campaign presented in this chapter involves the simultaneous testing of three slabs on distinct situations, regarding restraint of deformation and vertical load level. Accordingly: SLAB1 is subjected to the combined effect of restrained shrinkage and vertical loads (corresponding to the quasi-permanent load combination); SLAB2 is subjected to restrained shrinkage and minor bending moments caused by the slab's self-weight; SLAB3 is subjected to the same vertical loads that are applied on SLAB1, but without any externally induced restraint to axial deformation. A fourth situation, in which no axial restraint nor vertical loads are considered, is covered with the measurement of two complementary unrestrained specimens of plain concrete (DUMMY1 and DUMMY2), with the same cross-section of the slabs and 50cm long, allowing to determine the exact free deformations that are involved on the abovementioned slabs.

Whether these imposed deformations are caused by thermal variations (due to cement heat of hydration release or environmental temperature) or by drying shrinkage (which is the case addressed in this experimental campaign), they occur non-uniformly across the slab thickness. Even though drying shrinkage is essentially simulated (in current design standards) as a uniform strain field for practical determination of its structural effects [6,10], the non-linear process of humidity diffusion and evaporation from the exposed slab surfaces induces non-uniform stresses across the member thickness, which are known to influence the structural behaviour of the RC structure [21,110,111]. To enable validation of sophisticated numerical simulations, in which a non-uniform moisture field is considered, the evolution of RH profiles of concrete is assessed in the experimental program presented herein, using companion specimens from the same batch of the slabs and exposed to the same environment. The experimental program is complemented with test specimens for further characterization of the following concrete features at different ages: compressive strength, tensile strength, E-modulus and creep in compression.

The restraining device, schematically depicted on Fig. 3.1, was planned to simulate a stretch of a continuous one-way slab supported by transverse beams at every 4 m. Since the slab is simply supported, the free span is adjusted to 2.4 m, corresponding to the distance between zero bending moments in the continuous slab with the 4m span (i.e., ~3/5 of the total span). The supports are materialized by two transverse 40mm diameter steel rods, embedded in the slab at both extremities. Significant cracking is

expected at the extremities of the slab, because of concrete stress concentrations close to the steel rods, and the transfer of forces to the concrete by bond action. Therefore, the measurement of the slab's average axial deformation is limited to a central control region with a length of 1.4m – see Fig. 3.1.

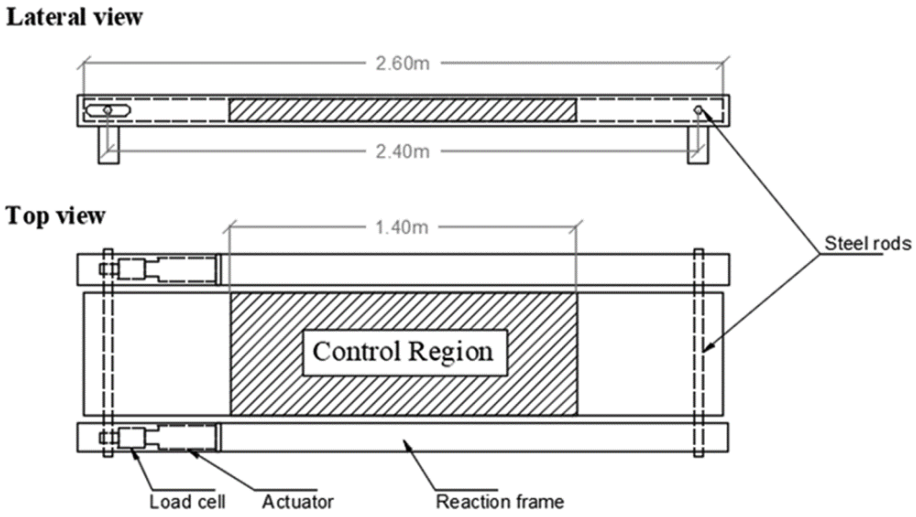

Figure 3.1 – Setup of the restraining device.

On each of the restrained slabs (SLAB1 and SLAB2) the axial deformation is controlled by imposing an axial force via two actuators, connected to the steel rods embedded in the slabs. On each slab a manually controlled hydraulic pump is used to induce the force in the two actuators. The structural behaviour of all slabs is continuously monitored throughout the entire experimental campaign, by recording the vertical deflection at mid-span, the average in-plane deformation in the control region, the steel strains in the tensile and compression reinforcement, the evolution of the crack pattern at the bottom slab surface and the crack widths.

All tests are conducted within a climatic chamber with controlled T and RH. A steady pace of monitoring of several relevant parameters, as well as the continuous assessment of the structural behaviour of the slab, is performed over 18 months, under constant environmental conditions.

3.3 Test setup

3.3.1 Restraining device

The restraining device consists of two reaction frames, made-up with hollow section steel profiles designed to provide enough inner space to accommodate the hydraulic actuators and load cells that are connected to the moving steel rod embedded in the slab, as shown in Fig. 3.2.

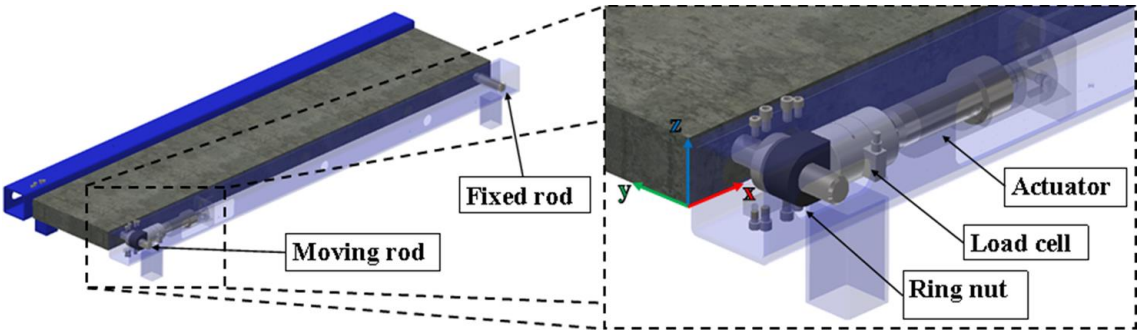

Figure 3.2 – Experimental setup of the restraining device.

Each reaction frame is composed by two 2.65m long steel Square Hollow Section (SHS) struts, with an outer cross-section of 140×140 mm² and 8mm thick walls, supported by four 0.30m long steel SHS columns with an outer cross-section of 80×80 mm² and 4mm thick walls. Each slab support is materialized with one solid steel rod, with a diameter of 40mm, embedded at mid-height. In one of the extremities, the "Fixed rod" is inserted in a 40mm diameter hole, located on the lateral side of the metallic strut (see Fig. 3.3a). On the other extremity, the "Moving rod" (see Fig. 3.3b) is connected to a radial ball bearing (SKF® 6208-2RS1), between two roller tracks whose position is adjusted with 4 socket head cap screws. The radial ball bearing carries the vertical load and is longitudinally free to slide, while the axial restraint of the slab is performed with two double effect hydraulic actuators (with negligible stiffness in the vertical direction, hence capturing no vertical load), each one with a capacity of 100 kN in compression at a pressure of 200 bar, placed inside the metallic strut, and connected to the moving rod by a ring nut. The hydraulic actuators are connected in parallel to a manual hydraulic pump capable to apply a pressure up to 250 bar, with a 3 litters reservoir. Two TCETM type resistive load cells of Class 1 accuracy and a measurement range of 100kN, from AEP transducers, are connected between the ring nuts and the actuators, to assess the axial load applied to the slab at each instant – see Fig. 3.3b.

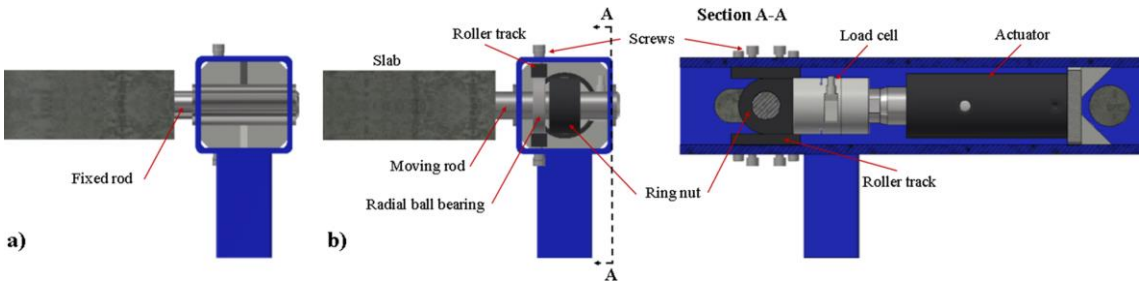

Figure 3.3 – 2D view of the restraining device components inside the metallic frame: a) fixed support; b) moving support.

Given the complexity of the devised test setup, with several elements of different nature interacting with each other, the modelling of the restraining device was performed with an object-oriented approach, in which the model is composed by objects that, besides the geometric parameters, are attributed with other type of data (e.g., information about manufacturer, cost and technical features, spatial relations with

adjacent objects and behaviour rules). Such approach enables the development of complex models in periods of time that would not be possible with conventional computer aided design (CAD) software and reduces the risk of mistakes through automatic detection of incompatibilities.

The model of the restraining device was developed in AutoDesk Inventor Professional 2018. It is composed by several assemblies, which includes the steel components of the reaction frames and support system, actuators and load cells, wood components for formwork and propping system, and the test specimen. Fig. 3.4 shows an exploded view of the restraining device and subsequent stages of the test setup assembly, automatically generated from the final model.

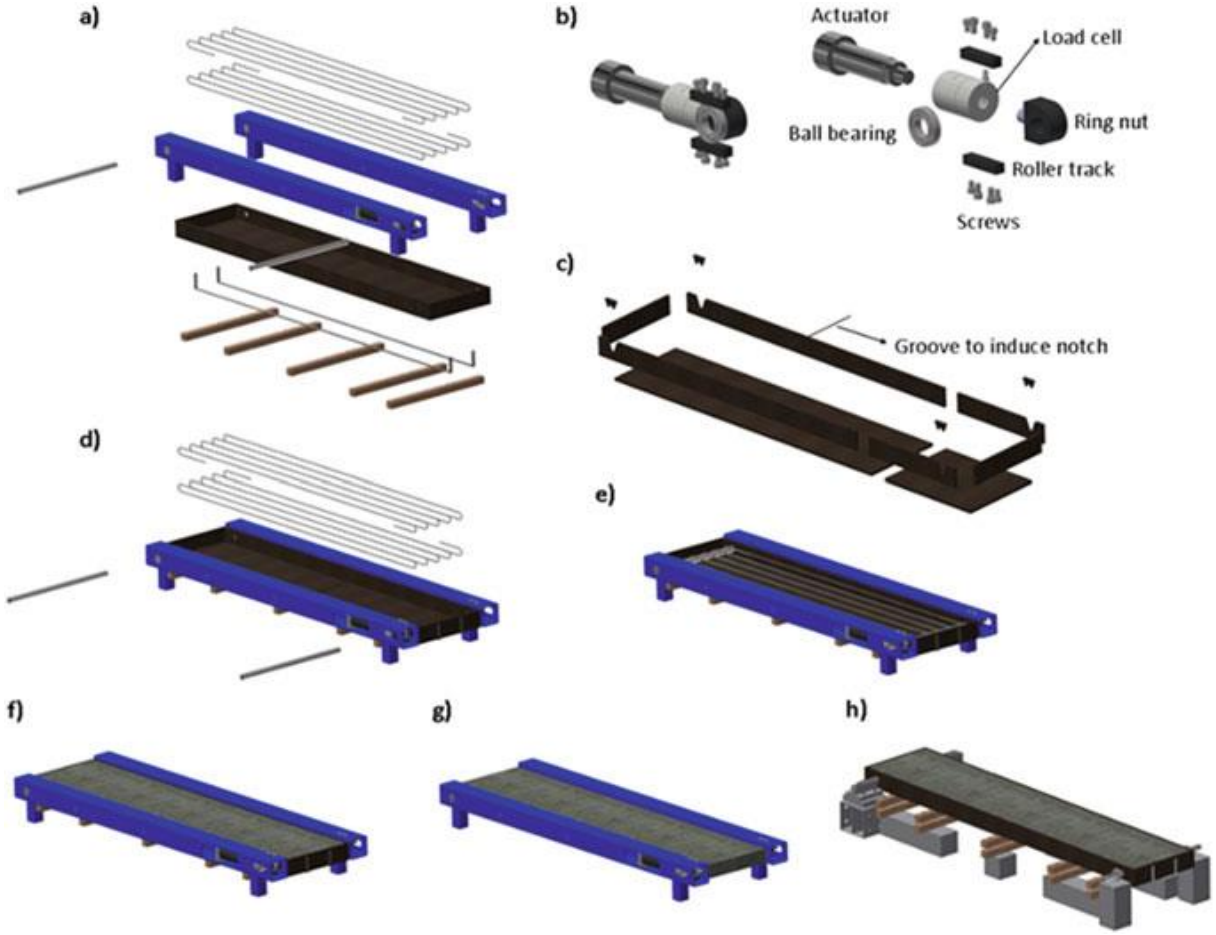

Figure 3.4 – Assembling steps of the test setup: a) pre-assembled restraining system; b) components inside the restraint frame; c) pre-assembled formwork; d) positioning and propping of formwork; e) positioning of longitudinal rebars and steel rods; f) casted test specimen; g) test specimen after formwork removal; h) support and formwork propping systems for unrestrained specimen.

The STP file format for interoperability of the general industry, as defined by [128], was used to order the production of these components, allowing for a straightforward process. The model contains information regarding the geometry of the different components and the spatial relation between them, as well as material information and object standardized references. The components inside the restraint frame, presented in Fig. 3.4b (assembled and isolated), were defined based on the abovementioned

requirements, with specific information regarding the brand and commercial references also included in the model. For the remaining components, only information about the material was attributed, besides the geometry and spatial relation with other components.

A specific formwork/propping system was designed for the restraining device to facilitate its extraction from confined spaces and to avoid damaging the test specimens during removal operations. The formwork is divided longitudinally in two parts (connected by two metallic plates with a 5×20 mm^2 cross-section), and it is composed by eight 18mm thick plywood panels, connected with metallic L-shaped brackets screwed to the bottom and lateral sides. After the formwork is assembled, it is positioned and fixed through five timber slats, spaced not more than 650mm, bolted to the bottom face of the restraint frames. The longitudinal rebars of the slab are then duly positioned inside the formwork. The notches on the lateral panels of the formwork enable the insertion of the steel rods through the reinforcement, between top and bottom rebars. The negative of the notch that is not filled by the supporting rod is sticked to the formwork with insulating tape. The position of the moveable support is adjusted and fixed with the roller tracks and head cap screws before casting the specimen. Immediately after casting, the top roller tracking is relieved to enable longitudinal displacement. After the curing period, the formwork is removed by unscrewing the metallic plates and L-shapes, as well as the timber slats. Alternative support and formwork propping systems were devised to account for simultaneous testing of the unrestrained specimen, in which five pairs of timber slats are supported by concrete blocks and the position of the formwork is adjusted by tightening the nuts of the screwed rods that connects the timber slats.

3.3.2 Detailing of specimens

The principle for sizing the three slab specimens submitted to the long-term experimental campaign corresponds to the simulation of a one-way continuous slab, supported by transverse beams and under a high axial restraint. For the sake of slab sizing and design, permanent loads of 2 kN/m^2 (to be superimposed to the self-weight) and variable loads of 3.2 kN/m^2 (2.0 kN/m^2 regarding the live loads for a floor of Category A, plus 1.2 kN/m^2 due to movable partitions) were considered according to Eurocode 1 [129]. The slab was designed for the Ultimate Limit State (ULS) according to Eurocode 2 [6] (EC2), resulting in a 0.10m thick element, made of concrete with a strength class grade C20/25, reinforced for bending with ϕ8mm S400C rebars spaced by 100 mm, both in the top and bottom layers. The secondary transverse reinforcement is materialized with ϕ6mm rebars spaced by 250 mm, corresponding to more than 20% of the longitudinal reinforcement, as recommended by EC2.

Fig. 3.5 shows the reinforcement layout of the test specimens (0.5m wide, to ensure a width-to-height ratio of 1/5 and, consequently, a standard slab-type behaviour) inside the formwork.

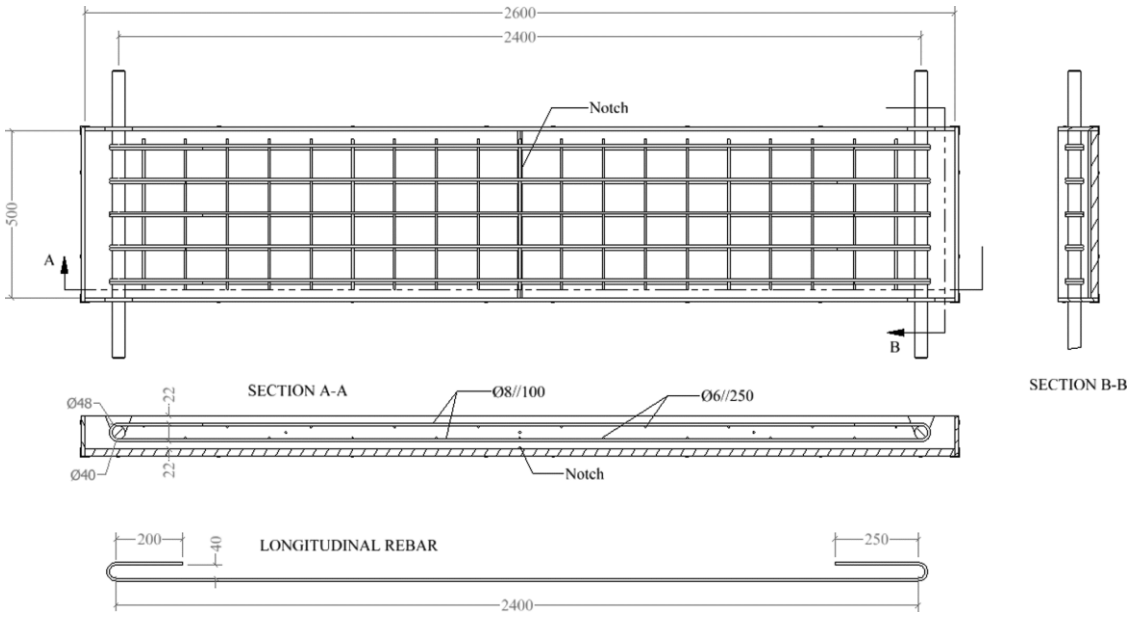

Figure 3.5 – Reinforcement layout inside the formwork.

Even though these specimens intend to simulate just the stretch of the slab with positive bending moments, no reinforcement curtailment is considered and the reinforcement on top layer is equal to the bottom layer one. The longitudinal reinforcement is anchored to the steel rods as shown on the lateral view of the reinforcement layout – see Fig. 3.5. The anchorage length varies alternately between 200mm and 250 mm, to enable a softer transition of bond stresses and, consequently, to avoid cracking of concrete in that region. The diameter of the steel rods and longitudinal reinforcement results in a concrete cover of 22 mm, which meets the requirements for buildings and other common structures (belonging to structural class S4) for an environmental exposure class X0, according to EC2. In order to ensure that the first crack is induced at mid-span, there is a bottom transversal rebar in that cross-section and a PVC angle glued to the bottom of the formwork, as to create a triangular notch 13mm wide and 8mm deep.

3.3.3 Measurements in the experiment

The monitoring of the thermo-hygro-mechanical behaviour of the slabs and companion specimens, as well as the environment of the climatic chamber during the long-term experimental campaign, was performed with the sensing devices to be described herein. In order to provide unambiguous information about the exact position of some sensors, the x-y-z axes shown in Fig. 3.2 will be considered as reference.

A wide range of sensors was used, with different systems for data acquisition, namely: (i) electrical resistance strain gages, restraining device load cells and Linear Variable Differential Transformers

(LVDTs), acquired by a National Instruments SCXI system (with modules SCXI 1314 and SCXI 1315); (ii) temperature sensors PT100, vibrating wire strain gages (VWSG) and LVDTs, acquired with a DataTaker DT80G and (iii) optical fibre Bragg grating sensors, measured with a FOS&S FBG-Datalogger 616.

Due to the lack of free channels in the SCXI 1315 module, the data of one LVDT used in the measurements was acquired with a four channel dynamic signal acquisition module (NI 9234) and an amplifier RDP S7AC. Measurements were taken continuously with a 5 min interval, except for data acquired with the SCXI system, in which the acquisition alternated between 1 Hz, during the application of restraint and vertical loads, and 1/30 Hz (i.e., at intervals of ~0.5 min) in the remaining time.

3.3.3.1. In-plane deformation and vertical displacement

Fig. 3.6 shows the position of the LVDTs used to measure the longitudinal deformations (in plane measurements - L_{IP}) and vertical displacements (out-of-plane measurements - L_{OOP}) of the slabs.

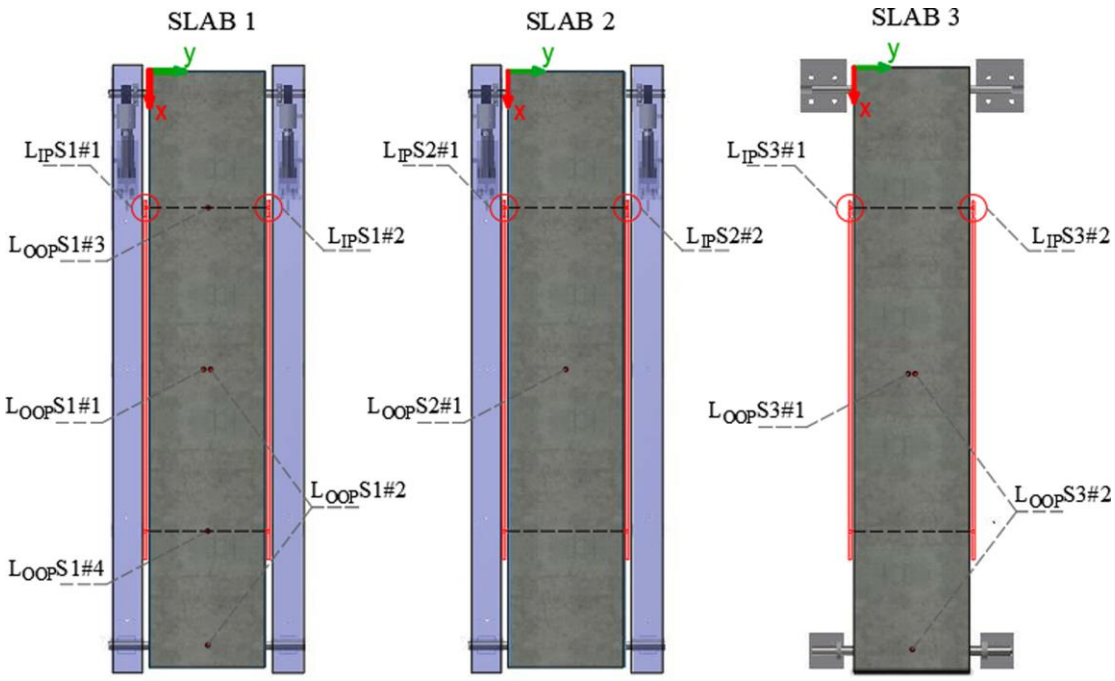

Figure 3.6 – Position of the LVDT's on the slab.

The LVDT's measurement range, the measurement system they are connected to, the commercial reference and the exact position in coordinates are displayed in Table 3.1.

Table 3.1 – Position and detailing of LVDTs.

LVDT	Range (mm)	System/module	LVDT series	x (m)	y (m)	z (m)
L_{IP}S1#1	+/- 5.0	NI SCXI 1315	RDP D5/200W	0.60	0.00	0.05
L_{IP}S1#2	+/- 5.0	NI SCXI 1315	RDP D5/200W	0.60	0.50	0.05
L_{IP}S2#1	+/- 5.0	NI SCXI 1315	RDP D5/200W	0.60	0.00	0.05
L_{IP}S2#2	+/- 5.0	NI SCXI 1315	RDP D5/200W	0.60	0.50	0.05
L_{IP}S3#1	+/- 2.5	NI SCXI 1315	RDP D5/100W	0.60	0.00	0.05
L_{IP}S3#2	+/- 2.5	NI SCXI 1315	RDP D5/100W	0.60	0.50	0.05
L_{OOP}S1#1	+/- 1.0	NI SCXI 1315	RDP GT1000RA	1.30	~0.25	0.00
L_{OOP}S2#1	+/- 1.0	NI SCXI 1315	RDP GT1000RA	1.30	~0.25	0.00
L_{OOP}S3#1	+/- 2.5	NI 9234	RDP GT2500RA	1.30	~0.25	0.00
L_{OOP}S1#2	+/- 5.0	DT80G	AML EU/10	1.30/2.50	~0.25	0.00
L_{OOP}S1#3	+/- 5.0	DT80G	AML EU/10	0.60	~0.25	0.00
L_{OOP}S1#4	+/- 5.0	DT80G	AML EU/10	2.00	~0.25	0.00
L_{OOP}S3#2	+/- 2.5	DT80G	AML EU/10	1.30/2.50	~0.25	0.00

The assessment of the average longitudinal deformation in the control region of each slab was performed with two LVDTs (L_{IP}), through a measuring system shown in Fig. 3.7, which consists of a 12mm diameter steel tube in contact with an LVDT fixed to a metallic clamp in one extremity (Fig. 3.7a). In the other extremity the steel tube is also fixed to a metallic clamp (Fig. 3.7b). Near the point of contact between the LVDT and the steel tube the latter is supported by a roller, which is fixed to the restraint frame (in the cases of SLAB1 and SLAB2) or to a concrete block (for SLAB3). To install this measuring system two hexagonal nuts M6 (onto which the metallic clamps are screwed to) are pre-embedded in the formwork of the slab on each lateral side, at mid-height and spaced 0.7m from the mid-span, allowing the measurements to be carried out on both sides of the specimen, between points A and B, and between C and D (Fig. 3.7c).

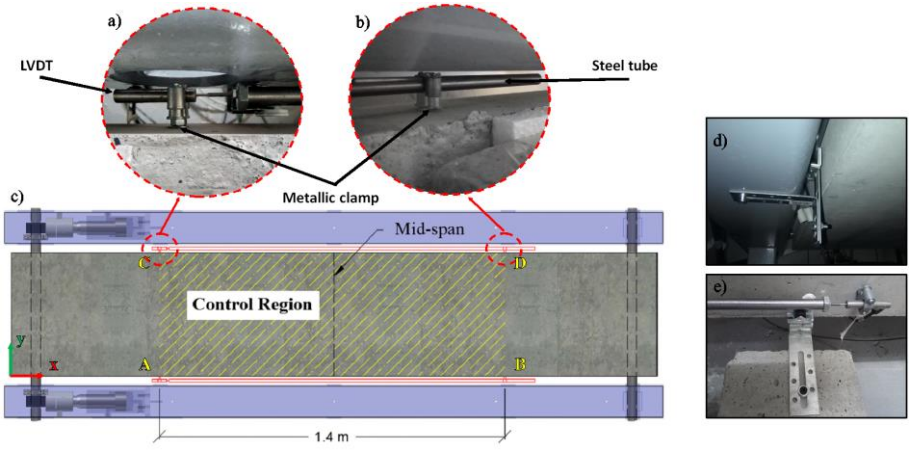

Figure 3.7 – System for measurement of the average longitudinal deformation on the control region: a) LVDT; b) fixed extremity; c) setup overview; d) detail of roller support on restrained specimen; e) detail of roller support on unrestrained specimen.

As regards the measurement of the vertical deflections, SLAB1, the most strongly loaded specimen (in terms of vertical loading plus restrained shrinkage), was monitored with the largest number of transducers: one placed at mid-span (L_{00P}S1#1), two at the extremities of the control region (L_{00P}S1#3 and L_{00P}S1#4, at x = 0.6m and x = 2.0m, respectively) and one at mid-span during the first days of the experimental campaign, the latter being moved to the support (x = 2.5 m) immediately before the application of the vertical loads, to measure the resulting settlement during and after loading (L_{00P}S1#2). The duplication of transducers at mid-span, in the first days, was adopted for redundancy reasons, to access the repeatability of the corresponding measurements.

On SLAB2, subjected to restrained shrinkage and self-weight only, just one LVDT (L_{00P}S2#1) was used to measure the vertical displacement at mid-span.

For SLAB3, subjected to vertical loads only, the transducers layout was similar to the one in SLAB1, without measuring the vertical deformation at the extremities of the control region. One LVDT (L_{00P}S3#1) was positioned at mid-span during the entire experimental campaign, whilst the L_{00P}S3#2 was used at mid-span during the first days, being moved to the support (x = 2.5 m) immediately before application of the vertical loads.

The longitudinal strain of the dummy specimens, for assessment of the concrete free shrinkage, was measured with a vibrating wire strain gage from Gage Technique, type TES/5.5/T, with a coefficient of thermal expansion of 11 ppm/°C and a gauge factor of 3.025×10^{-3}. The sensor is carefully placed orthogonally inside the dummy formwork, at mid-height, and it was fixed in that position with nylon wire (Fig. 3.8).

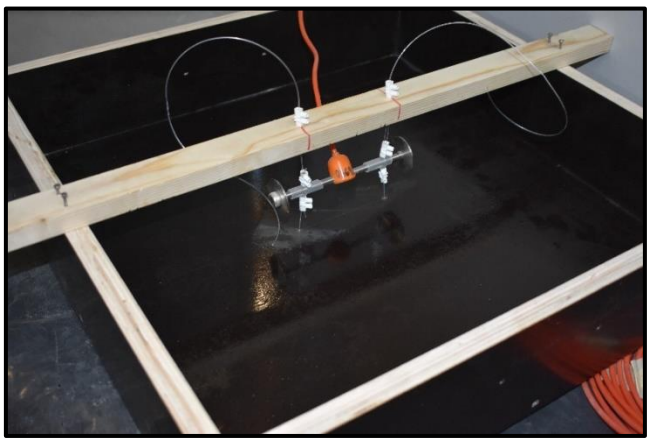

Figure 3.8 – Placement of the vibrating wire strain gage on the dummy specimen.

3.3.3.2. Strains on rebars

Fig. 3.9 and Table 3.2 shows the exact positions of the sensors used to measure the strains on the reinforcement.

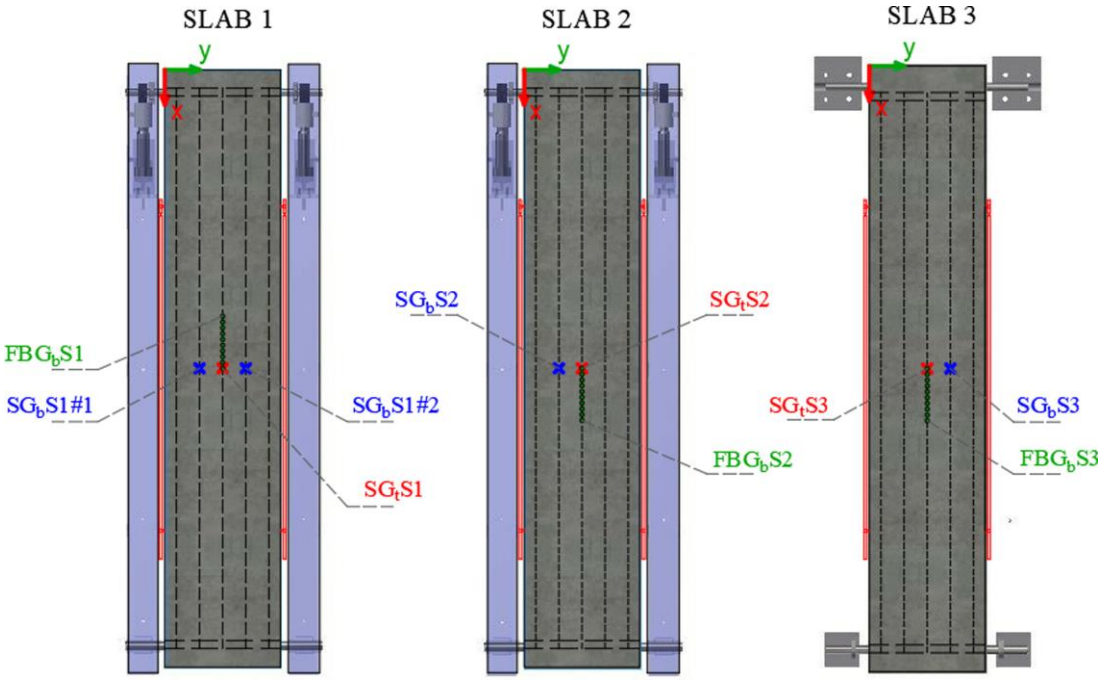

Figure 3.9 – Sensor in the rebars.

Table 3.2 – Position of the sensors in the rebars.

Position	SG$_t$S1	SG$_b$S1#1	SG$_b$S1#2	FBG$_b$S1	SG$_t$S2	SG$_b$S2	FBG$_b$S2	SG$_t$S3	SG$_b$S3	FBG$_b$S3
x (m)	1.30	1.30	1.30	1.05-1.30	1.30	1.30	1.30-1.55	1.30	1.30	1.30-1.55
y (m)	0.25	0.15	0.35	0.25	0.25	0.25	0.25	0.25	0.35	0.25
z (m)	0.074	0.027	0.021	0.026	0.077	0.022	0.024	0.071	0.024	0.024

Seven TML electrical resistance strain gauges, type BFLA-5-3, were used on both the top (SG$_t$) and bottom (SG$_b$) longitudinal rebars to measure the strain in the reinforcement at mid-span. The obtained results correspond to the average strain over a measurement basis of 5 mm. SLAB1 had two strain gages at the bottom (SG$_b$S1#1 and SG$_b$S1#2) and one at the top rebar (SG$_t$S1), whereas SLAB2 and SLAB3 were provided with one strain gage at the top (SG$_t$S2 and SG$_t$S3, respectively) and another one at the bottom rebar (SG$_b$S2 and SG$_b$S3, respectively).

In order to measure the strains at several points along the longitudinal rebar, for assessment of the transfer of bond stresses at the steel-concrete interface, an array of optical fibre Bragg grating sensors (FBG$_b$), supplied by Sylex, was used. The array comprehends ten 5mm long sensors, spaced by 25mm (wavelength between 1530 nm and 1557 nm), and was installed in the central bottom rebar of each slab. The first sensor of the array was positioned at mid-span, with all the other sensors positioned in one half of the slab. For installation of the optical fibre, a groove of 1×1 mm^2 was made along the steel rebar. The section of the optical fibre that was inside the concrete and was not glued to the rebar had to be protected

with a sealed tube and epoxy glue in order to avoid potential damage during the casting operations (Fig. 3.10).

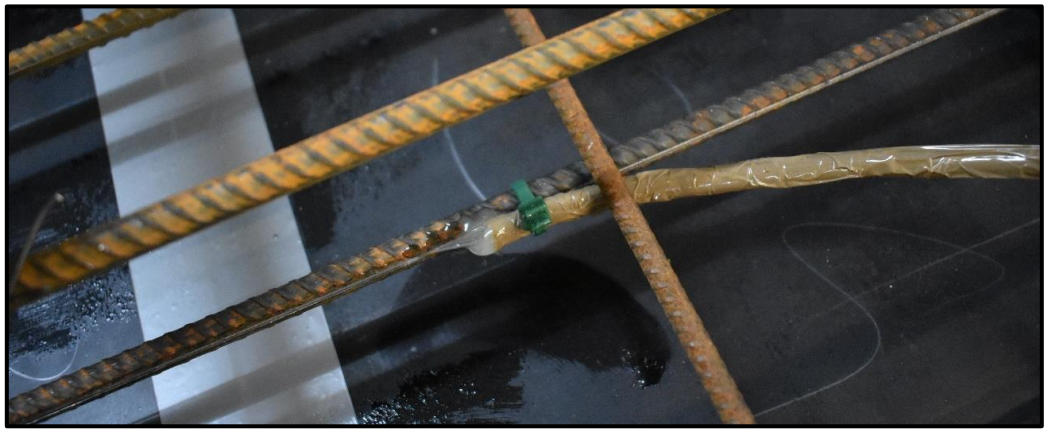

Figure 3. 10 – Detail of groove on the steel rebar and protection of the FBG array.

3.3.3.3. Crack width

Crack widths were assessed with discrete measurements made immediately before and after every time the load was compensated on the restrained slabs. The measurements were performed with a handheld USB microscope VEHO VMS-004, with an image sensor of 1.3 MegaPixels and magnification ratios of 20× and 400×.

3.3.3.4. Temperature and RH

The experimental campaign was conducted inside a climatic chamber with a controlled environment. The desired ambient T of 20°C +/- 0.5°C and RH of 60% +/- 5% was verified with discrete measurements using a Vaisala SHM4 Kit with a HMP40S temperature and humidity probe (Fig. 3.11a), with accuracies of +/- 0.2°C and +/- 1.5%, respectively. To assess the continuity of measurements, a temperature and humidity Datalogger UNI-T UT330B (Fig. 3.11b), with accuracies of ± 1.0 °C and +/- 3.0%, was used with measurement intervals of 30 min throughout the entire experimental campaign.

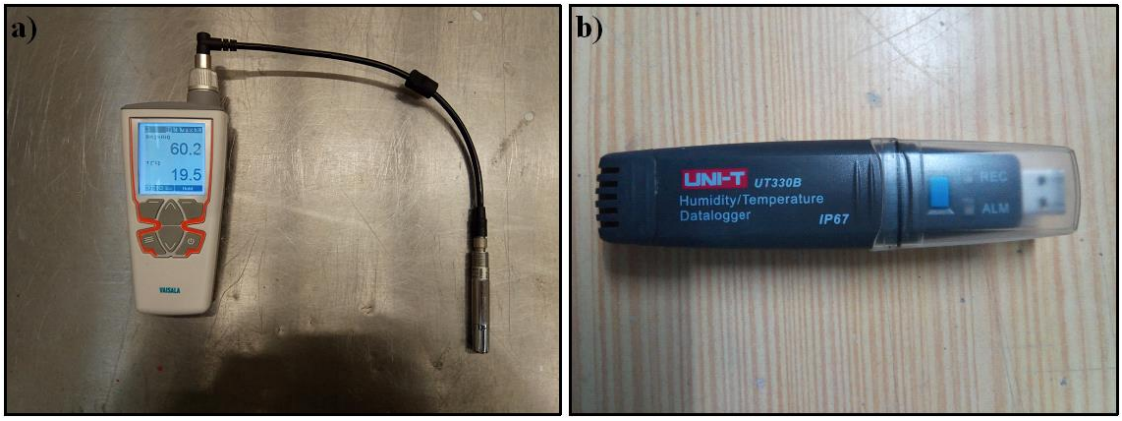

Figure 3.11 – Sensors used for measurement of T and RH: a) Vaisala SHM4 Kit with a HMP40S temperature and humidity probe; b) Datalogger UNI-T UT330B.

The temperature inside the slabs was measured with one PT100 sensor embedded on each slab at mid-height, at the coordinates x = 0.20m, y = 0.25m and z = 0.05m (Fig. 3.12). Another PT100 was placed outside, between SLAB1 and SLAB2, at the same z-coordinate of the other PT100 (z = 0.05m), to measure the environmental temperature.

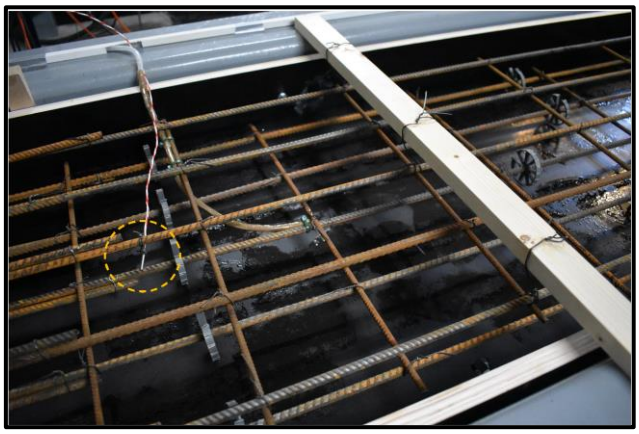

Figure 3.12 – Position of PT100 embedded in the slab.

The RH profiles of concrete were measured in complementary specimens of the same batch and subjected to the same environmental conditions of the slabs, according to the experimental procedures proposed by Granja et al. [12]. The RH at different depths were assessed through the insertion of the HMP40S probe on previously embedded sleeves within these concrete dummies (Fig. 3.13a). These specimens had the same curing conditions of the slabs: they were completely sealed during the first days after casting, and after formwork removal two faces were unsealed according to the configuration presented in Fig. 3.13b, to ensure that the drying flow on the specimens was 1D and parallel to the direction of the embedded sleeves. Two specimen geometries were considered, as shown in Fig. 3.13c: (i) 10×10×40cm^3, designated as H10, with measurement depths of 2cm, 4cm and 5cm; and (ii) 15×15×60cm^3, designated as H15, with measurement depths of 2cm, 4cm and 7.5cm. Two specimens

were cast for each geometry. The extremity of the plastic sleeve is protected with Gore-Tex® fabric (Fig. 3.13d) in order to ensure that the inner part is not obstructed by concrete during casting. This type of fabric is simultaneous impervious to water in the liquid state and permeable to water in the gaseous state. This technique for protecting the extremity of the embedded sleeve was duly validated by Granja et al. [12]

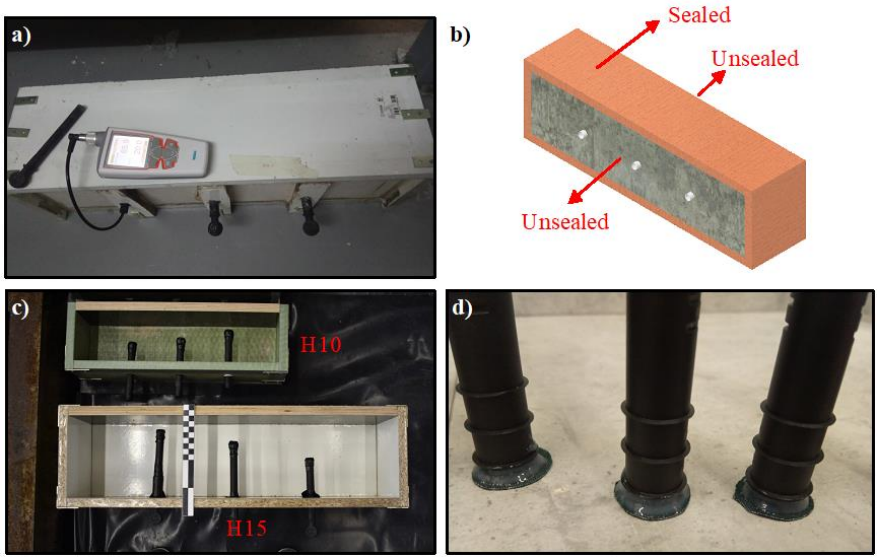

Figure 3.13 – Measurement of RH profiles: a) insertion of Vaisala probe in embedded sleeves; b) schematic representation of specimens for RH profiling; c) formwork and embedded sleeves; d) protection of sleeve's extremities with Gore-Tex®.

3.4 Experimental Procedures

3.4.1 Concrete mix and material characterization

A ready-mix concrete was ordered with a class grade C20/25, suitable for an exposure class X0(P), with a maximum aggregate size of 14mm and a slump consistency class S3. A single batch of concrete was used to cast all the slabs and companion specimens for this experimental campaign, with the mix composition indicated in Table 3.3.

Table 3.3 – Concrete composition.

Material	Quantity (kg/m³)
CEM II A/L 42.5R	291
Gravel (6/14)	763
Gravel (2/14)	220
Coarse sand	432
Thin sand	547
Plasticizer Chrysoplast 775	2.32
Water	171

In addition to the slabs and dummies for assessment of free shrinkage and RH profiles, the experimental campaign was complemented with the characterization of several concrete properties at different ages. Testing ages of 7 and 50 days were selected to get information regarding the main mechanical properties of concrete at the ages of formwork removal (instant of application of self-weight), and at the instants of application of the remaining vertical loads. Accordingly, the specimens indicated in Table 3.4 were cast with the same batch of concrete used for the slabs.

Table 3. 4 - Concrete characterization plan.

Property	Specimens (mm)	Age (days)	Norm/Ref.
Compressive strength	12× Cube 150×150×150	3, 7, 28 and ∞*	[131]
E-modulus	3× Cylinder φ150×300	7, 28 and 51	[132]
Tensile splitting strength	6× Cylinder φ150×300	7 and 28	[133]
Tensile flexural strength	6× Prism 150×150× 600	51 and ∞*	[134]
Creep	4× Cylinder φ150×300	8 and 50	[135]
Free shrinkage (creep dummy)	2× Cylinder φ150×300		

*Over 1 year.

The assessment of concrete creep in compression was performed with the hydraulic-driven creep rig depicted in Fig. 3.14, with creep specimens exposed to the same environment of slabs and companion specimens. The strains were measured with VWSG type TES/5.5/T (the same that is used to measure the strains in the dummy specimens) and the applied load was measured with a 100kN capacity C2AD1 type load cell from HBM.

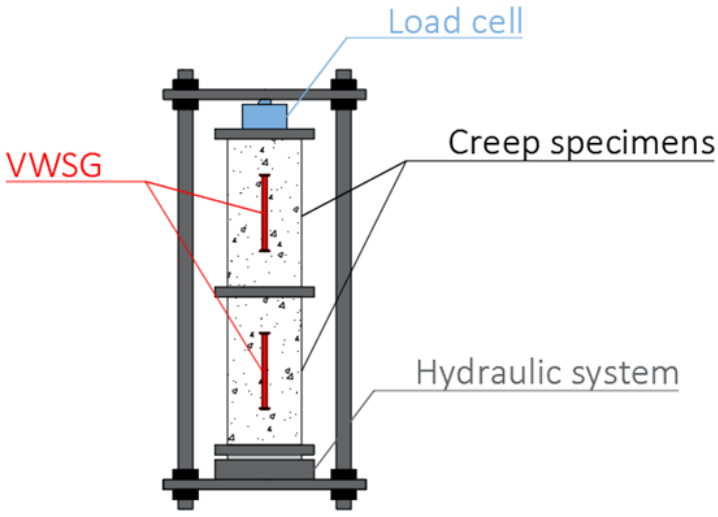

Figure 3.14 - Schematic representation of the hydraulic-driven creep rig.

3.4.2 Preparation of the experimental campaign

The preparation of the long-term experimental campaign included a pilot test, described in Gomes et al. [18], which was performed to assess the viability of the test setup, with particular concern with the

performance of the restraining device, and to verify whether further improvements might be needed. In this trial experiment, the restraining system has demonstrated its suitability to impose and control a pre-determined axial load, and the monitoring devices showed satisfactory results at key instants.

In order to eliminate the influence of ambient temperature and RH variations in the results, thus simplifying the analysis, a climatic chamber was specifically constructed for this experiment on the IB-S laboratory (University of Minho, Guimarães). The room, with a net area of 3.6×4.9 m^2, was built with double layer wood panels and 5cm thick extruded polystyrene (XPS) modules – see Fig. 3.15a. The temperature was controlled through an air conditioning device (Fig. 3.15b), whereas the RH was kept constant with a dehumidifier and humidifier devices working simultaneously – see Fig. 3.15c-d.

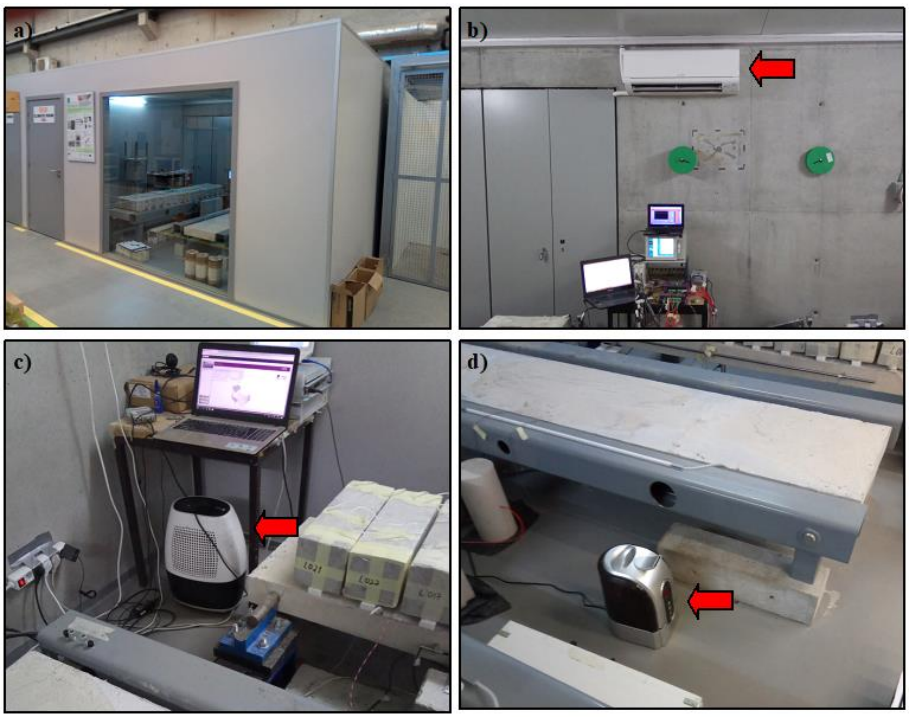

Figure 3.15 – Climatic chamber: a) view from outside; b) air conditioner; c) dehumidifier; d) humidifier.

The discrete monitoring of temperature and RH inside the climatic chamber, performed with the HMP40S probe throughout the entire experimental campaign, is presented in Fig. 3.16a. It can be observed that the desired ideal environment of T = 20 °C ± 0.5 °C and RH = 60% ± 5%, within the percentiles of 5% and 95%, was achieved. The measurements performed with the internal RH and temperature sensors of the Datalogger for assessment of continuity of results (Fig. 3.16b) show a reasonable agreement with the discrete measurements, despite the offset on the average values due to different locations of the sensors (higher temperatures at higher positions) and different calibration.

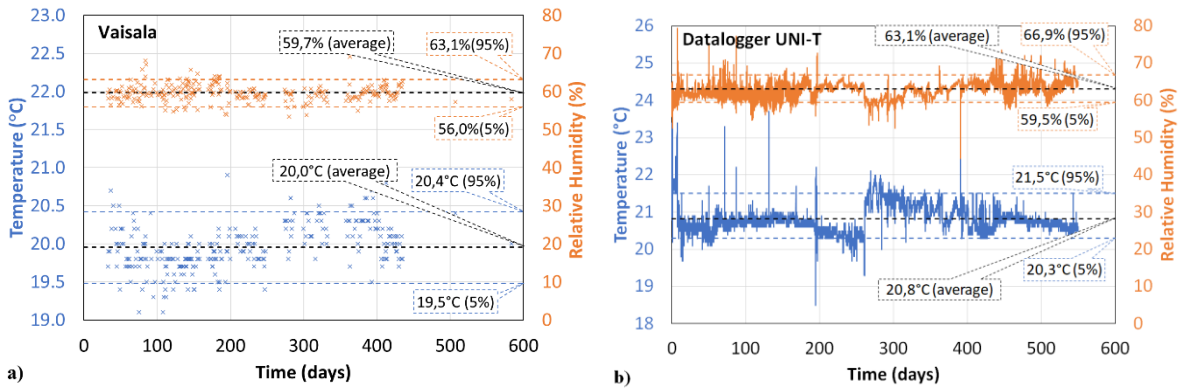

Figure 3.16 – Evolution of temperature and RH inside the climatic chamber: a) discrete measurements with Vaisala sensor; b) continuous measurements with UNI-T datalogger.

All test specimens were kept inside the climatic chamber with the arrangement depicted in Fig. 3.17. Considering the limited space inside the climatic chamber and the amount of instrumentation employed on the slabs, a micromanagement plan (involving 14 people with specific position and roles) was developed for the casting day, so that all specimens were cast in a small-time frame, during which the fresh concrete age can be considered the same. Detailed information regarding the micromanagement plan for the casting day can be found in [137].

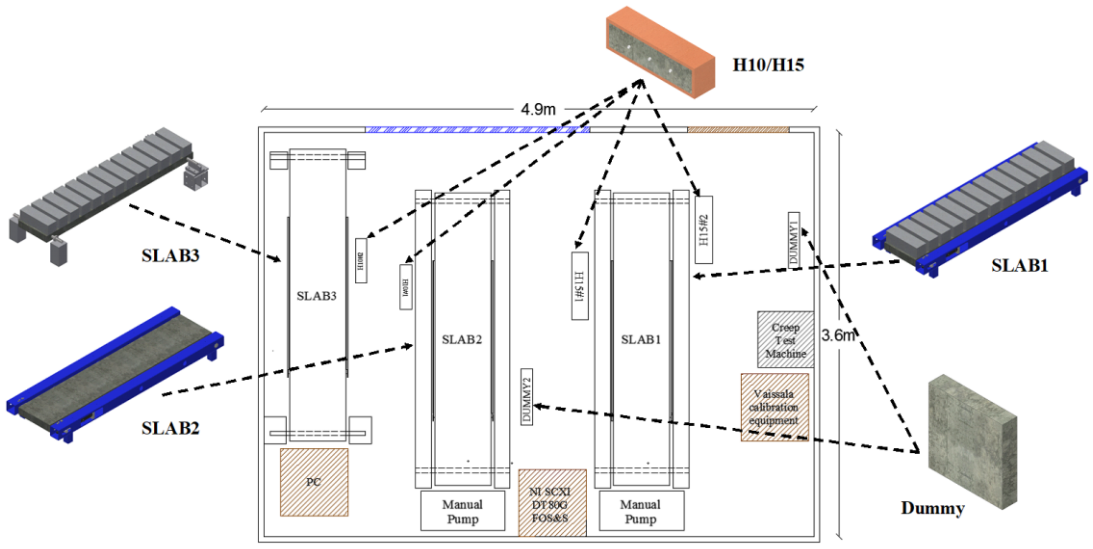

Figure 3.17 – Arrangement of test specimens inside the climatic chamber.

3.4.3 Implementation and control of restraining condition

The concrete casting took place on April 17, 2018. The mixing started at 13:54 (corresponding to the origin of time considered herein for presentation of results) and the concrete truck arrived at the site at 14:35. A slump test was performed at 14:44 to check the consistency class of the concrete, and a slump of 120mm (class S3) was achieved as intended. The casting started at 14:50 and ended at 15:40. The

filling of the moulds and the vibration of the concrete with a vibration needle was conducted according to EN 12390-2 [138]. At the end all test specimens were sealed with plastic film on the exposed face (including the slabs) and kept inside the climatic chamber. Fig. 3.18 shows the climatic chamber immediately before and after casting.

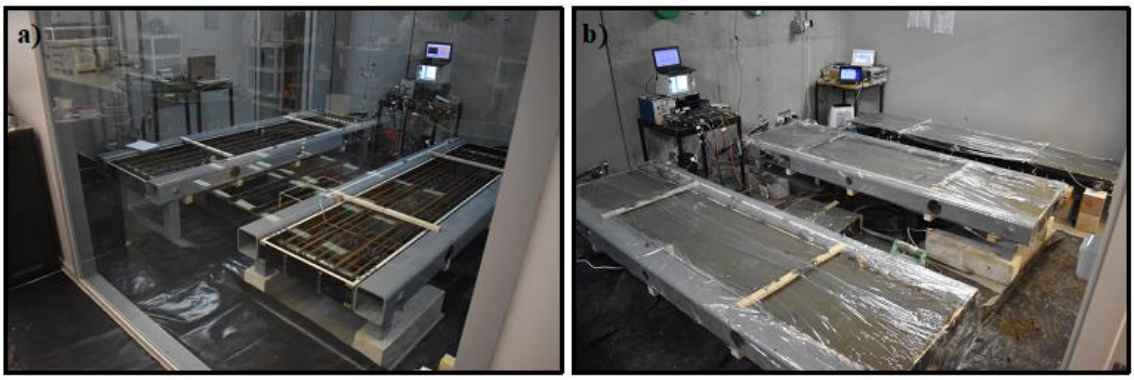

Figure 3.18 – Climatic chamber: a) before casting; b) after casting.

At the age of 7 days the formworks of all test specimens were removed and the slabs were consequently subjected to the effects of drying and their self-weight. Before demoulding the slabs, 3 LVDTs were positioned on the top surface, at mid-span, to measure the vertical deflection during formwork removal. The vertical displacements measured during the formwork removal were consistent, varying between 0.7 and 0.8mm (Fig. 3.19).

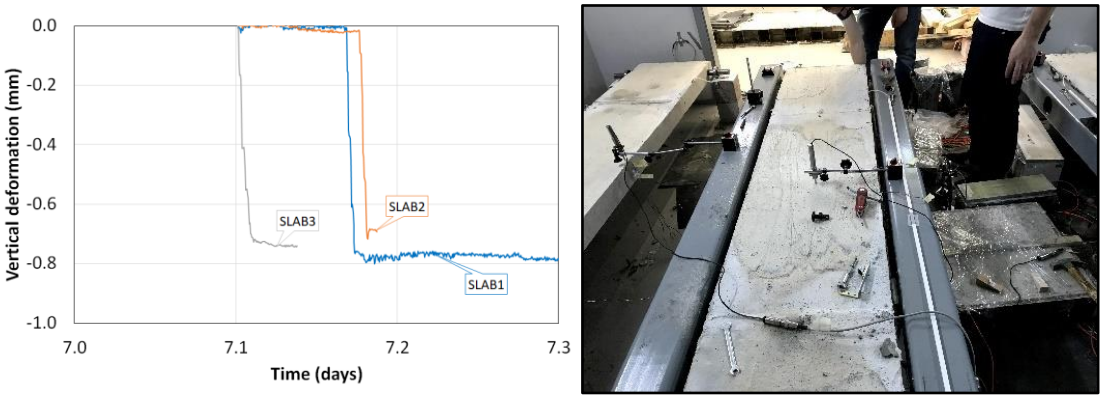

Figure 3.19 – Vertical deformation of slabs during formwork removal at 7 days.

After formwork removal, the test specimens for assessment of compressive and tensile strength and E-modulus of concrete were immediately sealed with plastic film to avoid drying until the age of testing. The cylinders used to measure the compressive creep and free shrinkage were subjected to the same drying history as the slabs and dummy specimens. The prisms for assessment of the RH profiles were also subjected to the same drying history of the slabs and dummy specimens.

After removing the formworks from the climatic chamber, the LVDTs were installed according to the protocol described in Section 3.3.3. At the age of 7.5 days, when the measuring system for measuring

deformations on the control region was installed, the estimated longitudinal strains of SLAB1, SLAB2 and SLAB3, based on the measured strains on the top and bottom rebars, were –28με, –20με and –25με, respectively. These strain measurements were considered to be representative of the average slab deformation, because no cracking was observed by that time. The initial measurements of the average in-plane deformation of the control region with the LVDTs did not show a smooth continuous variation. Instead, it varied in steps only after a certain strain variation has taken place. This behaviour was partially due to friction effects in the auxiliary metallic apparatus connecting the concrete structure to the LVDT transducer. This issue was mitigated by introducing modifications in such apparatus (mainly reducing the distance between the LVDT and the lateral slab surface), which came into effect at the age of 22 days (final form of this measuring system was presented in Section 3.3.3).

Given the initial difficulties and lack of confidence on the measured average deformation in the short term, the control of the restraint condition on SLAB1 and SLAB2 was performed with the application of an expected restraint force based on a combination of: (i) more reliable measurement results (crack width at the bottom slab surface and free shrinkage); and (ii) preliminary viscoelastic analyses with resource to the age adjusted elastic modulus (AAEM) method [139]. This procedure involves four main steps, which were followed before each increment of axial load being applied: (i) the width of all visible cracks was measured and the shrinkage strains were recorded; (ii) the AAEM method was applied to calculate the axial load increment needed to fully compensate the average axial deformation in the control region, considering the recorded shrinkage strain; (iii) the measured crack widths were used to update the concrete tensile strength values considered in the AAEM calculations, as well as the average deformation in the cracked zone considered in the same calculation; and (iv) the axial load to be applied by the hydraulic actuators was estimated using the updated model.

A total of 9 axial load increments was applied before the application of vertical loads. Fig. 3.20 depicts the evolution of the applied restraint force on both slabs until 50 days, as well as the corresponding average deformation measured in the control region. SLAB1 and SLAB2 were subjected to equal increments of axial load before the age of 50 days, because their vertical loading was also the same during that period.

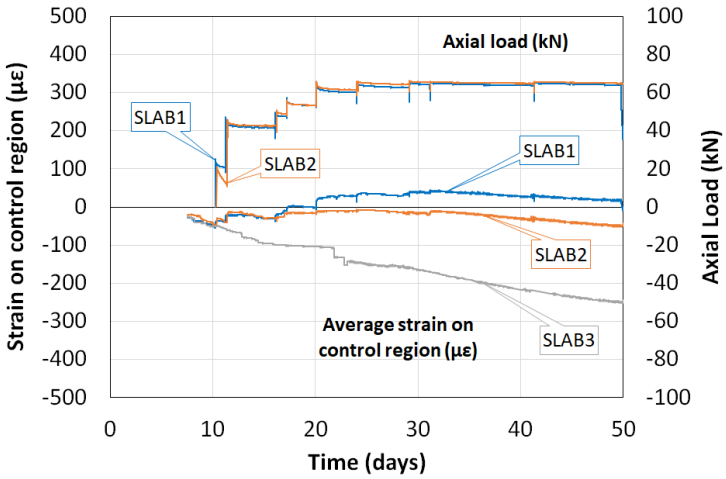

Figure 3.20 – Restraining force (SLAB1 and SLAB2) and average deformation in the control region for all slabs for the first 50 days.

At the age of 50 days SLAB1 and SLAB3 were loaded with 14 concrete blocks to simulate the quasi-permanent load combination p_{qpc} for a class A floor, according to EC1 [129],

$$p_{qpc} = g_1 + q \cdot \psi_2 = 2.0 + (2.0 + 1.2) \times 0.3 = 2.96\ kN/m^2 \qquad \text{(Eq. 3.1)}$$

where g_1 is the additional permanent load, q is the live load and ψ_2 is the reduction factor for live loads in the quasi-permanent load combination [140].

In order to enable concrete drying from the slabs' top surface, 20×40×480 mm^3 XPS stripes were used to support the loading blocks – see Fig. 3.21.

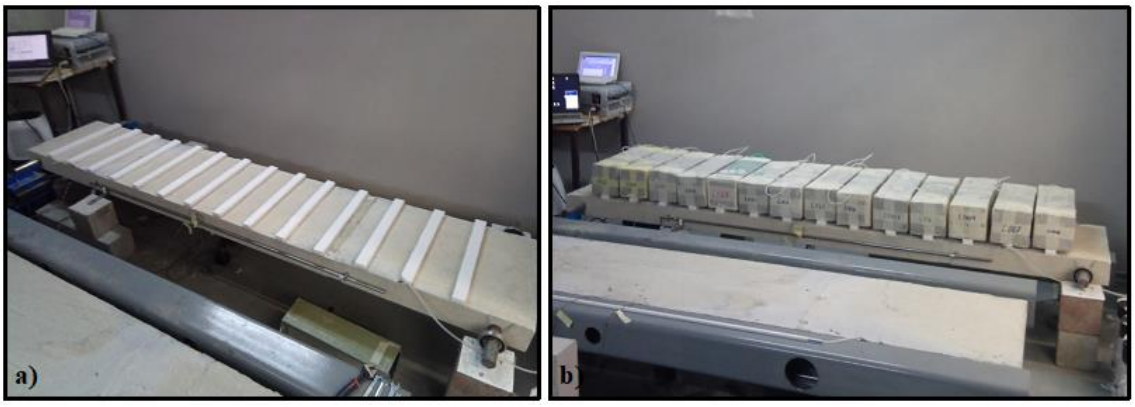

Figure 3. 21 – Application of vertical loads on SLAB3: a) XPS stripes and b) concrete block.

During the application of a vertical load to an end restrained element, the axial restraint force decreases because of the widening of pre-existing bending cracks and the formation of new ones [127]. The devised restraint system is not passive. Instead, the restraint force depends on the oil pressure in the hydraulic actuators. In order to avoid excessive positive strains due to the formation of new cracks in SLAB1, the restraint force was manually decreased during the application of vertical loads by 29kN. This value was estimated using the same type of AAEM calculation described for the previous period of time. The

application of the vertical load on SLAB1 was performed in 4 stages, to avoid abrupt variations. At each stage selected load blocks were placed, to induce an increment of bending moment in the slab of ~25% of the total increment. Also, at each stage the axial restraint force was decreased by 25% × 29 kN = 7.25 kN. After the end of the fourth stage, it was found that no new bending crack was formed (unlike the prediction of the AAEM calculations). This is because the concrete tensile strength considered in the AAEM estimate was slightly lower than the real one in the experiment. Consequently, the axial load decrease of 29 kN, given by the AAEM calculation, was overestimated. Therefore, after placing all loading blocks, the axial load on SLAB1 was progressively increased, until a situation of full restraint has been achieved (corresponding to a measure average axial strain in the control region near ~0.0 με).

From 60 days onwards the axial loads applied to the slabs were kept constant, with average values of 57 kN and 71 kN for SLAB1 and SLAB2, respectively (Fig. 3.22).

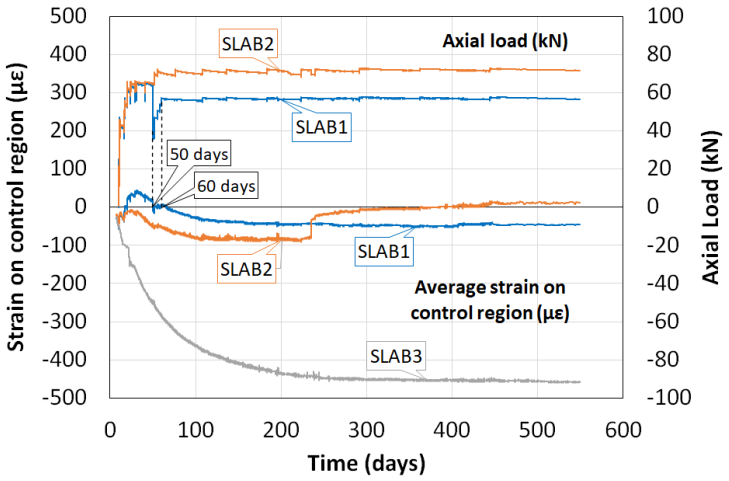

Figure 3.22 – Restraint force and average longitudinal strains in control region over 18 months.

3.5 Results

3.5.1 Mechanical characterization of concrete

The experimental results for concrete characterization are reproduced in Fig. 3.23 and Table 3.5. Fig. 3.23 also shows the prediction for the development of concrete properties over time, based on cement type and experimental values at 28 days of age, according to EC2 [6]. It can be observed that, even though these predictions are coherent with the overall experimental results for other testing ages, the evolution of modulus of elasticity during the first days is overestimated by EC2. This observation is consistent with the experimental results of modulus of elasticity obtained by other authors [141,142].

The concrete tensile strength was determined as the splitting tensile strength $f_{ctm,sp}$ at the ages of 7 and 28 days, and as the flexural tensile strength $f_{ctm,fl}$ at the ages of 51 and 499 days. An approximate value for the uniaxial tensile strength of concrete f_{ctm} may be determined by multiplying the experimental results by the conversion factor α_{sp} for the splitting test, or by the factor α_{fl} for the flexural tensile test:

$$f_{ctm} = \alpha_{sp} \cdot f_{ctm,sp} \quad \text{(Eq. 3.2)}$$

$$f_{ctm} = \alpha_{fl} \cdot f_{ctm,fl} \quad \text{(Eq. 3.3)}$$

Conversion factor α_{sp} may vary from 0.67 up to 0.95, depending on the codes and standards that are considered. However, there are in the literature comprehensive research results showing that this factor lies between 1.1 and 1.3 for normal strength concrete [10,143]. Values of α_{sp} ranging between 0.9 and 1.0 are considered in EC2 and MC10, respectively. Nonetheless, the empirical formulation proposed by Malárics and Müller [143] for calculation of α_{sp}, given by Eq. 3.4 (f_{cm} is the compressive strength in MPa, here taken as the cube compressive strength $f_{cm,cube}$ multiplied by a factor of 0.8), leads to better coherence between the values of tensile strength obtained with splitting and flexural tests – see Fig. 3.22b.

$$\alpha_{sp} = 2.08 \cdot f_{cm}^{-0.16} \quad \text{(Eq. 3.4)}$$

The value of conversion factor α_{fl} for assessment of the relationship between flexural and axial tensile strength, according to EC2 [6], is given by Eq. 3.5:

$$\alpha_{fl} = \frac{1}{1.6 - \frac{h_b}{1000}} \quad \text{(Eq. 3.5)}$$

where h_b is the height of the concrete element (in mm). Conversion of results for the splitting and flexural tensile tests, according to Eq. 3.4 and Eq. 3.5, respectively, are also presented in Table 3.5.

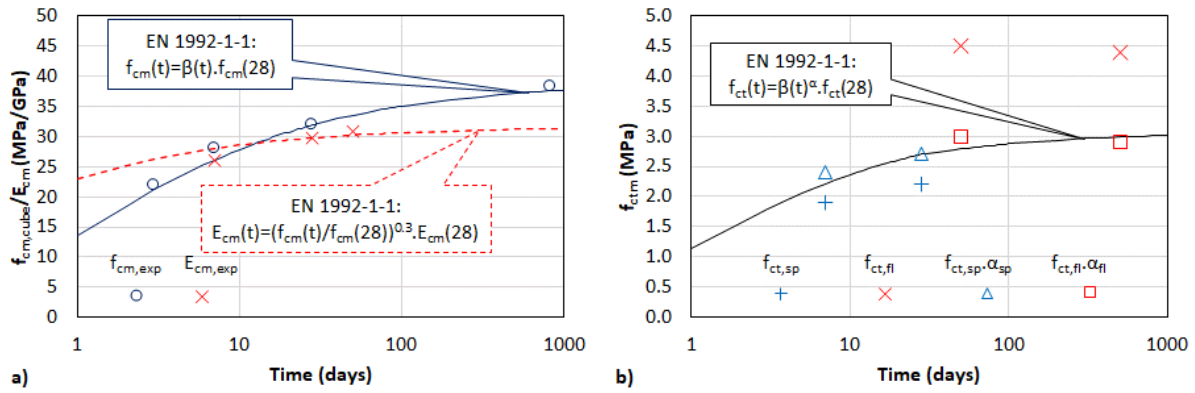

Figure 3.23 – Experimental results for concrete properties and prediction of property development over time [6]: a) compressive strength and elastic modulus; b) tensile strength.

Table 3.5 – Average values of the mechanical properties of concrete (coefficient of variation in brackets).

Property	Age (days)					
	3	**7**	**28**	**51**	**499**	**822**
Cube compressive strength (MPa)	21.9 (0.024)	28.0 (0.047)	31.9 (0.046)		-	38.4 (0.10)
E-modulus (GPa)	-	26.1 (*)	29.8 (0.013)	30.8 (0.033)	-	-
Tensile splitting strength (MPa)	-	1.9 (0.055)	2.2 (0.031)	-	-	-
Tensile flexural strength (MPa)	-	-	-	4.5 (0.052)	4.4 (0.072)	-
Uniaxial tensile strength (MPa) [6,143]	-	2.4	2.7	3.0	2.9	-

*Only one valid test was performed at this age.

The creep tests were carried out on two specimens (CT8#1 and CT8#2), loaded in compression at the age of 8 days. At the age of 50 days these specimens were unloaded, and the same equipment was used to perform the test on two different specimens (CT50#1 and CT50#2). The specimens (FS#1 and FS#2) were used to assess the free shrinkage of the cylinders, which must be subtracted from the measured strains of specimens CT8 and CT50 to obtain the elastic plus the creep deformations. A compressive stress of 5MPa was applied in both creep tests (this value was limited by the load cell capacity), representing approximately 20% of the concrete compressive strength. The resulting specific creep curves for the loading ages of 8 and 50 days, as well as the respective prediction according to Eurocode 2, are shown in Fig. 3.24. It can be observed that the experimental results for loading age of 8 days are in line with the specific creep estimated with the EC2 formulation, which does not happen for experimental results at loading age of 50 days. This can be justified by the fact that the Eurocode model does not take into account the drying that occurs before the loading age. Concrete stiffness tends to reduce with drying [144–146], whether because of microcracking around the aggregate (caused by inhomogeneous shrinkage strains between coarse aggregate and mortar) or due to loss of resistance to deformation as the water in the pores is replaced by air. For that reason, smaller strains would be expected from CT50 specimens if they were exposed to drying only at 50 days.

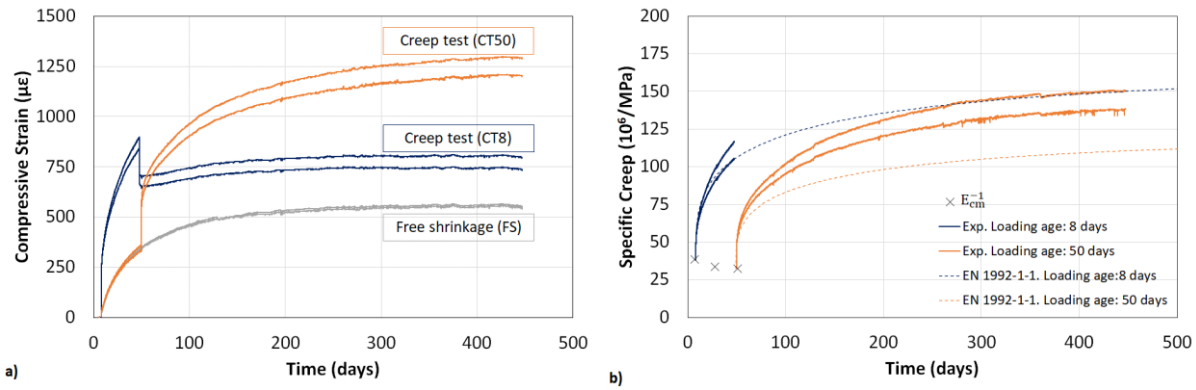

Figure 3.24 – Assessment of concrete creep: a) bulk strain and b) specific creep for loading ages of 8 days and 50 days.

3.5.2 T and RH

Temperatures at the concrete core of each slab and in the environment measured by the PT100 sensors, are reproduced in Fig. 3.25. It can be observed that the release of cement heat of hydration causes the concrete temperatures to reach peaks at approximately the age of 12h, with values ranging between 32.8 °C and 33.7 °C. At the age of 7 days the slabs' temperatures reach equilibrium with the environment. At this age, immediately after formwork removal, the slabs' T experience a sudden drop due to the evaporative cooling effect, reaching again the equilibrium with the environment within the next days.

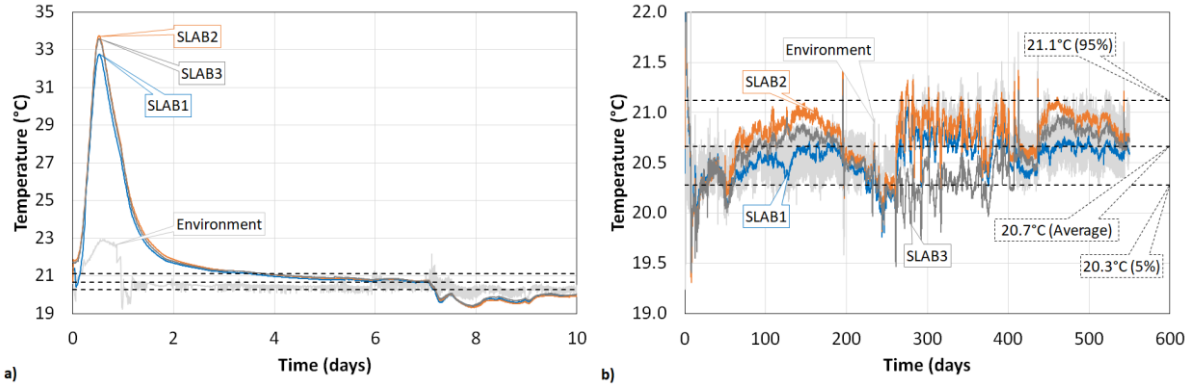

Figure 3.25 – Evolution of T: a) first 10 days and b) over 18 months.

The RH profiles measured in the two specimens H10 and H15 are shown in Fig. 3.26. The first measurements were performed at the age of 6 days, before formwork removal, at a depth of 4cm. The RH assessed on these first measurements ranged between 96% and 100% (for this level of RH, the equipment accuracy is ± 2.5%), indicating that the decrease of humidity during the first days in which the specimens were sealed was not very significant, as expected for a concrete with high water-to- cement ratio (w/c), and therefore with negligible drying due to self-desiccation [147]. The RH profiles measured on specimens H10, with the same thickness of the slabs, show that the deepest point (5cm away from the top and bottom surfaces) reached a RH < 70% at the end of measurements, that is, an almost full equilibrium with the surrounding environment, which is at a RH = 60% ± 5%. For specimen H15, however, the drying process had not yet reached its conclusion at the end of measurements. Moreover, it can be observed that thicker specimens (H15) have higher RH values, for the same depth, as a result of the water flow that occurs between the core and the surface of the specimens [141].

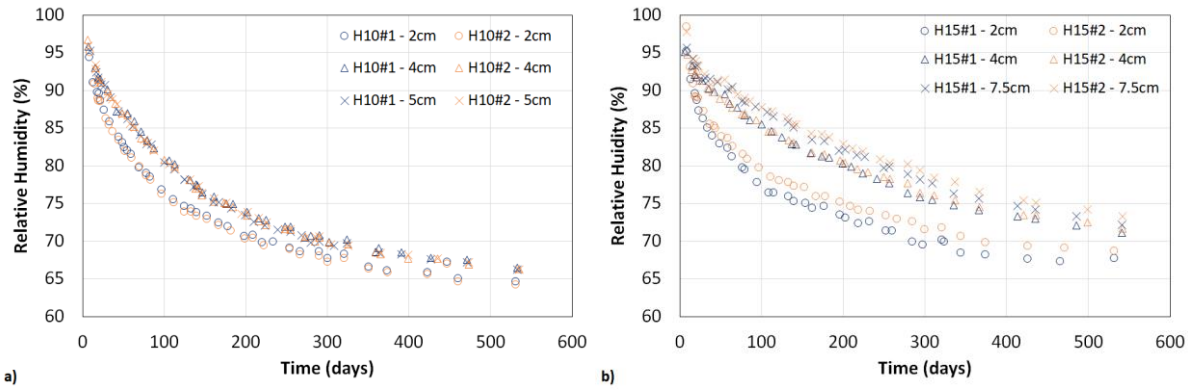

Figure 3.26 – RH profiles in specimens H10 and H15.

3.5.3 Concrete free shrinkage – dummy specimens

The longitudinal strains and core temperature measured in the dummy specimens, before and after formwork removal, are presented in Fig. 3.27.

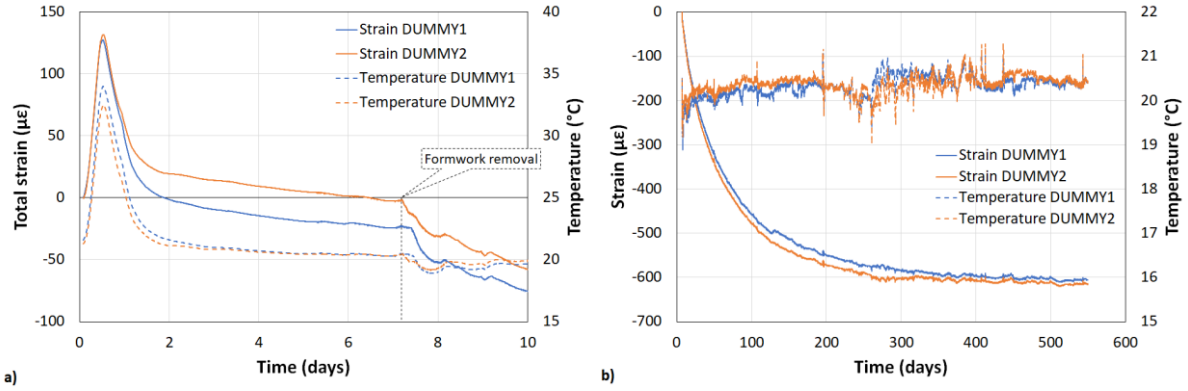

Figure 3.27 – Longitudinal strains and core temperature in the Dummy specimens: a) first 10 days; b) measurements after formwork removal.

It can be observed that the recorded temperature at the core of the specimen is very similar to what was observed for the slab specimens. The release of cement heat of hydration causes the concrete temperatures to reach peaks at approximately 12h, with values ranging between 32.5°C and 34.0°C. At 7 days, the concrete temperature is in equilibrium with the environment temperature. Immediately after formwork removal, the temperature undergoes a sudden drop due to the evaporative cooling effect, reaching again the equilibrium with the environment within the subsequent days.

The VWSG sensors embedded in the dummy specimens cannot record the concrete strains before a certain level of rigidity is achieved. For that reason, the VWSG measurements presented in Fig. 3.27a start at the instant at which the temperature begins to increase significantly (approximately 2 hours after mixing), which is associated to the end of induction period and to the initial setting of cement (loss of flowability and gain of rigidity). An average maximum strain of 130με was recorded at approximately 12h, corresponding to the thermal deformation caused by an average temperature rise of 12°C. The average

strain recorded immediately before the formwork removal is -12με. Taking into account the uncertainty related to the value of concrete's coefficient of thermal expansion and its variation at early ages, the exact instant at which the concrete is stiff enough so that the VWSG is able to truly determine the material strains, and the small order of magnitude of the recorded strains before formwork removal, the autogenous shrinkage of concrete was considered negligible and the total longitudinal strains of concrete were zeroed immediately before formwork removal, at 7 days of age (time axis and reference age are kept unchanged in all graphics of this Chapter).

The average longitudinal stains recorded in the dummy specimens between formwork removal and the end of experimental campaign is -610με (Fig. 3.27b). This value represents the concrete free shrinkage that is endured by the slab specimens.

3.5.4 Rebar strains

The strains measured with the Bragg grating sensors during the first days of the experimental campaign are presented in Fig. 3.28. The reference measurement for these early age results is the same as for the VWSG measurements presented in Fig. 3.27a (~2h after mixing) and the average results are coherent with the strains recorded in the dummy specimens: i) an average maximum strain of 120με is recorded at approximately 12h; ii) the average strain recorded immediately before the formwork removal is -22με. Even though the substantial scatter of results between sensors of the same fibre array was not expected, it can be explained by the local strains caused by pouring and vibration of concrete during the casting (which are not constant over the rebar length) and partial relaxation of these strains during concrete hardening.

The rebar strains measured with the electrical resistance strain gages during the first days are not presented. The quarter bridge system of strain gauge measurement with only two wires was used for these sensors and the temperature effect of the lead wires (which were partially embedded in the slabs) before temperature stabilization could not be compensated.

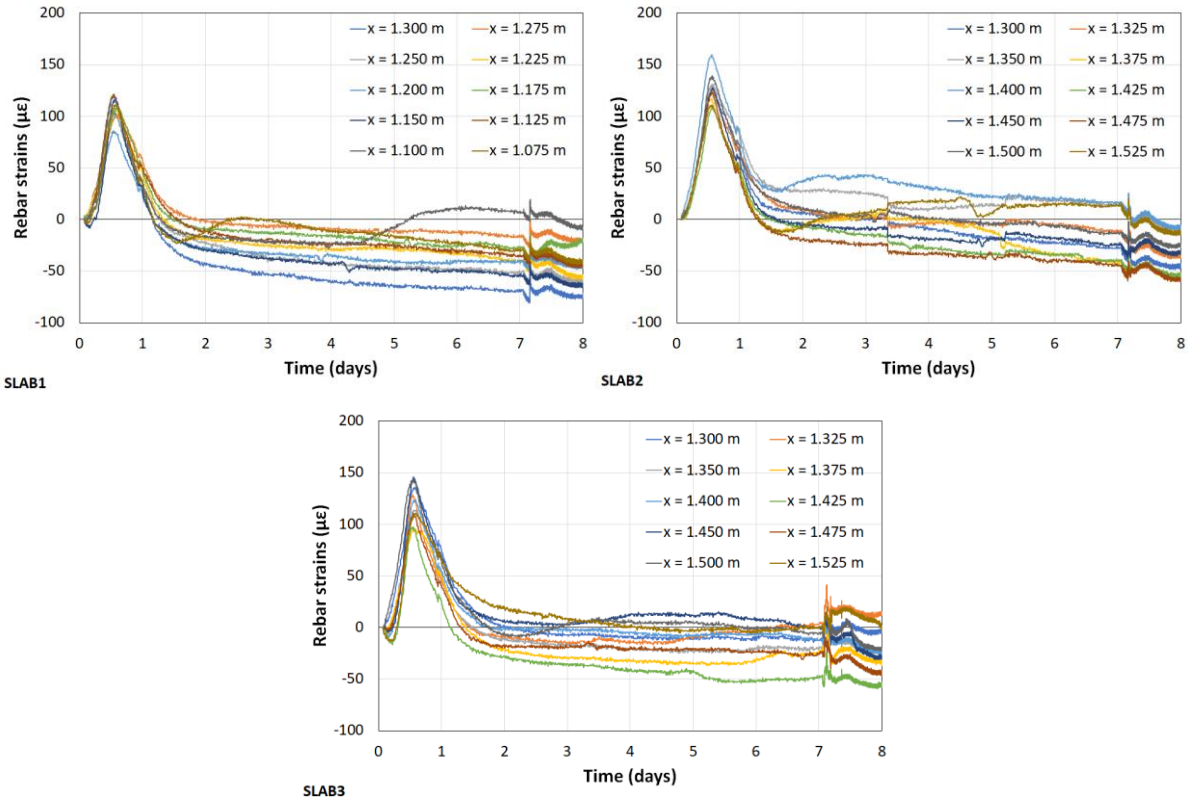

Figure 3.28 – Recorded strains with the fibre Bragg Grating sensors during the first 8 days.

Figs. 3.29-3.31 show, for the three slabs, the rebar strains at mid-span during formwork removal and over the entire experimental campaign. These results were zeroed at reference age of 7 days in coherence with the results presented for concrete strains in Section 3.3.3.

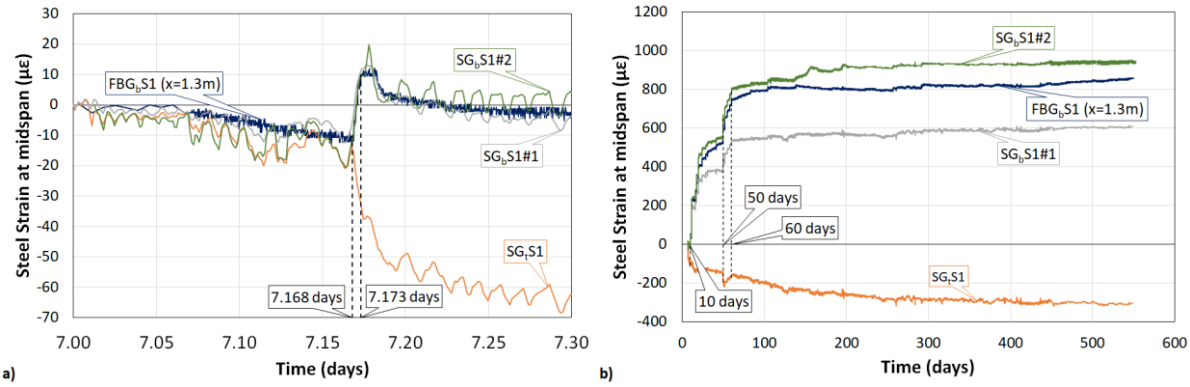

Figure 3.29 – Evolution of strains at mid-span of SLAB1: a) during formwork removal; b) over 18 months.

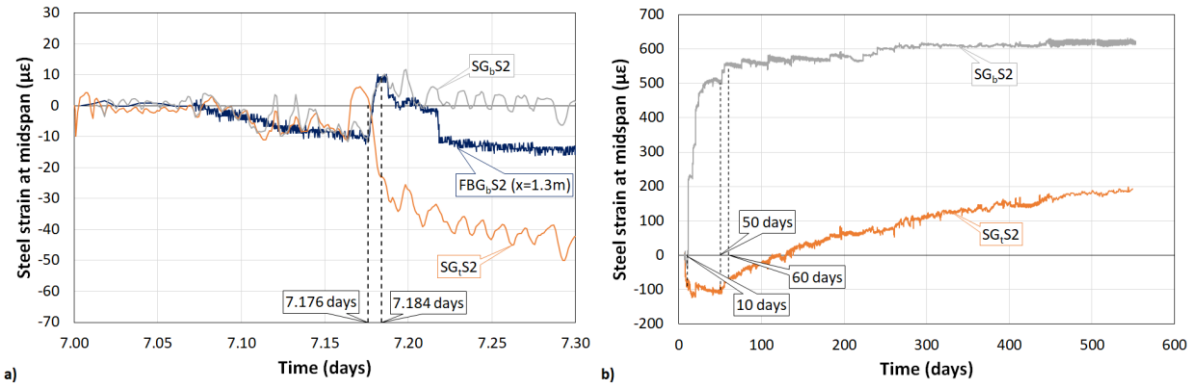

Figure 3. 30 - Evolution of strains at mid-span of SLAB2: a) during formwork removal; b) over 18 months.

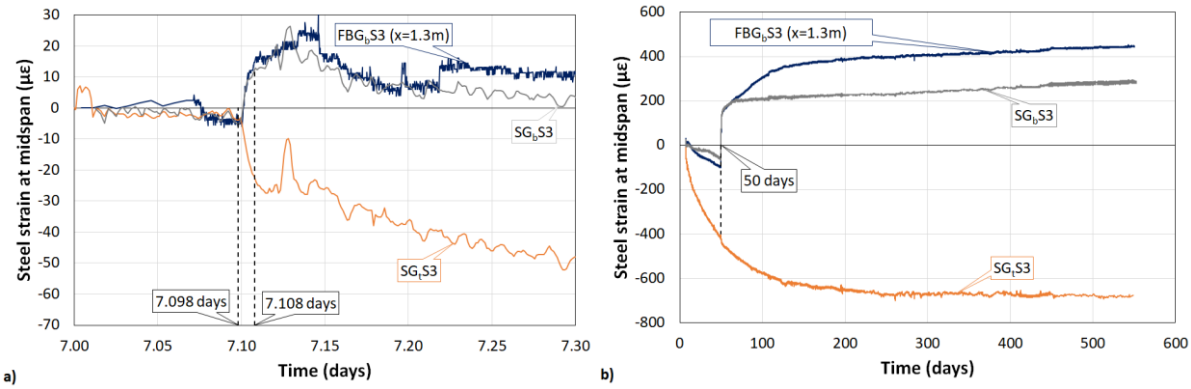

Figure 3.31 - Evolution of strains at mid-span of SLAB3: a) during formwork removal; b) over 18 months.

The results given hereinafter represent the mean strain over the measurement basis of 5 mm. The ages corresponding to the removal of the wooden slats supporting the formwork are represented by black dashed lines in Figs. 3.29a, 3.30a and 3.31a. During this period the slab was gradually subjected to its self-weight, resulting in a variation in the bottom and top rebar strains of ± 17με –23με, depending on the position of the sensor.

Since the plastic film on the top surface of the slabs and lateral planks of the formwork were removed first, top and bottom rebars presented an initial strain variation of –5με to –10με immediately before being subjected to the self-weight, due to the effects of evaporative cooling and drying shrinkage (periods: 7.07–7.17 days in SLAB1; 7.07–7.18 days in SLAB2; 7.07–7.11 days in SLAB3). After formwork removal, while the slabs are still behaving elastically (i.e., before cracking occurs), it is possible to observe a negative variation on the steel strains, more pronounced on the top rebar due to the combined effects of concrete creep and drying shrinkage.

After the instant of cracking at mid-span (at 10 days for SLAB1 and 50 days for SLAB3), significant differences were observed on the several measurements on the bottom rebars, in the same cross-section. These differences can be justified by differences between the exact position of the crack and the sensor (due to irregular development of the crack over the width and height of the slab cross-section). For SLAB2,

however, there was no redundancy of measurements on the bottom rebars at mid-span, since the Bragg grating sensor at that position stopped measuring after 11 days.

Figs. 3.32–34 show, for each slab, the strains measured with the Bragg grating sensors along the longitudinal axis of the bottom rebar. The following key instants are worthwhile to be analysed: at 7 days – before and after formwork removal (BFR and AFR, respectively); at 10 days – before and after application of restraint load (BRL and ARL, respectively); at 50 days – before and after application of vertical load (BVL and AVL, respectively); 60 days – age at which the restraint force is kept constant and 548 days – at the end of experiment.

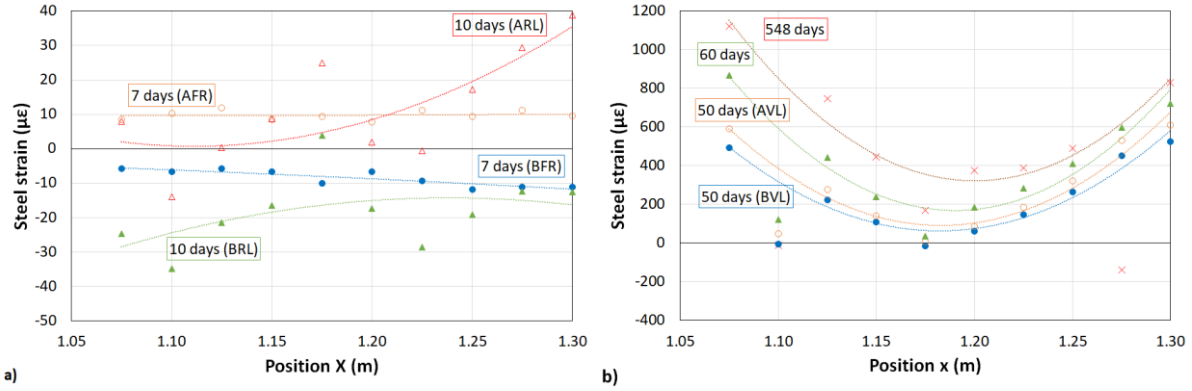

Figure 3.32 – Strains along longitudinal axis of bottom rebar – SLAB1: a) at 7 and 10 days; b) at 50, 60, and 548 days.

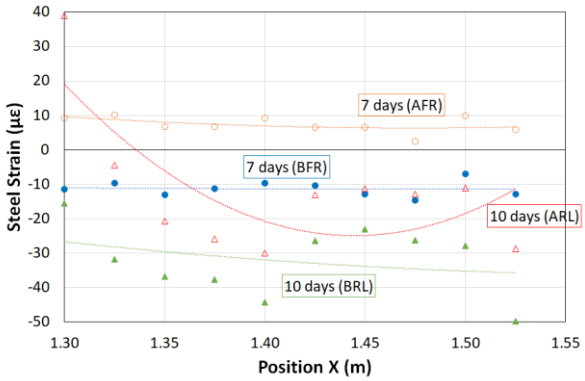

Figure 3.33 - Strains along longitudinal axis of bottom rebar at 7 and 10 days – SLAB2.

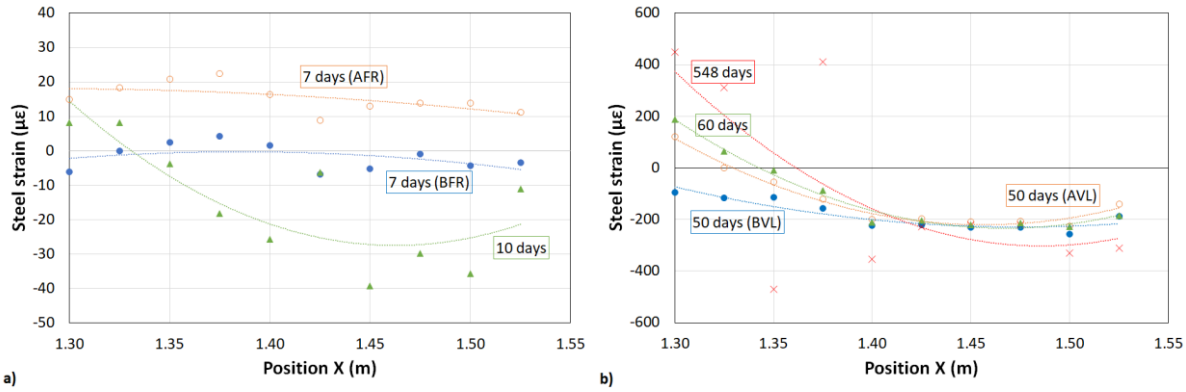

Figure 3.34 - Strains along longitudinal axis of bottom rebar – SLAB3: a) at 7 and 10 days; b) at 50, 60, and 548 days.

To facilitate the analysis of results and to understand the overall tendency of the strain variation along the rebar longitudinal axis, each set of points representing the strains measured by the sensors are accompanied by the respective polynomial trend-line. All results are presented within the monitored cross-sections: between x = 1.30m and x = 1.05m for SLAB1 and between x = 1.30m and x = 1.55m for SLAB2 and SLAB3.

During formwork removal it is possible to observe, for all slabs, a rebar strain variation of approximately 20με at mid-span (x = 1.30m), and a slightly smaller strain variation on the opposite end of the fibre array (around 15με), due to a smaller bending moment in that section.

For SLAB1 and SLAB2, the occurrence of cracking at mid-span after application of a restraining force of 25 kN, at 10 days of age, is observed on Figs. 32a and 33, where a significantly greater increase on the rebar strain is observed for the sensor at x = 1.30 m, in comparison to the other sensors.

On SLAB1, at 50 days, the parabolic shape of the trend-line denotes the development of two main cracks located near the extremities of the sensors array. As expected, the tensile rebar strains increase consecutively after application of the vertical load and subsequent compensation of the restraint force and continued to increase until 548 days, due to creep effects, with strain variations progressively greater near the cracks.

For SLAB2 some sensors stopped measuring after application of the axial load at 11 days, and the remaining ones do not show a plausible evolution after that age. Therefore, those results are not presented.

On SLAB3 the cracking at mid-span occurs at 50 days, during application of the vertical load. After that age the tensile strain on the bottom rebar increases until the end of the analysis (548 days) near the crack at mid-span, due to the effects of creep and the evolution of the crack width, accompanied by the

progression of the crack depth. The rebar strains at the opposite extremity of the Bragg sensors array remain negative, as a consequence of the concrete shrinkage deformation, which means that there are no cracks reaching the reinforcement in that zone.

3.5.5 Crack pattern and crack width

Fig. 3.35 shows the crack patterns for all slabs at 548 days. On the control region of SLAB1 and SLAB2 three main cracks (the ones with a final maximum crack width above 0.10 mm), represented by red dashed lines, develop on the bottom of the slabs during the first days after restraint of deformation: one at mid-span (Crack 1) and two spaced by 0.25m from mid-span at each half of the slab (Cracks 2 and 3). The final measured crack width is also shown in the figure, for all the main cracks, in three different positions along the transverse direction.

The position of Crack 1 is naturally determined by the notch. The position of the other main cracks is heavily influenced by the transverse reinforcement spacing, which is precisely 0.25 m. Throughout the whole experimental campaign some minor cracks (with widths always smaller than 0.10 mm) were detected (represented by black dashed lines), without significant development over time. On SLAB3 one single main crack is induced at mid-span after application of the vertical load at 50 days, and unlike the cracks observed on the restrained slabs, it develops evenly over the slab's width.

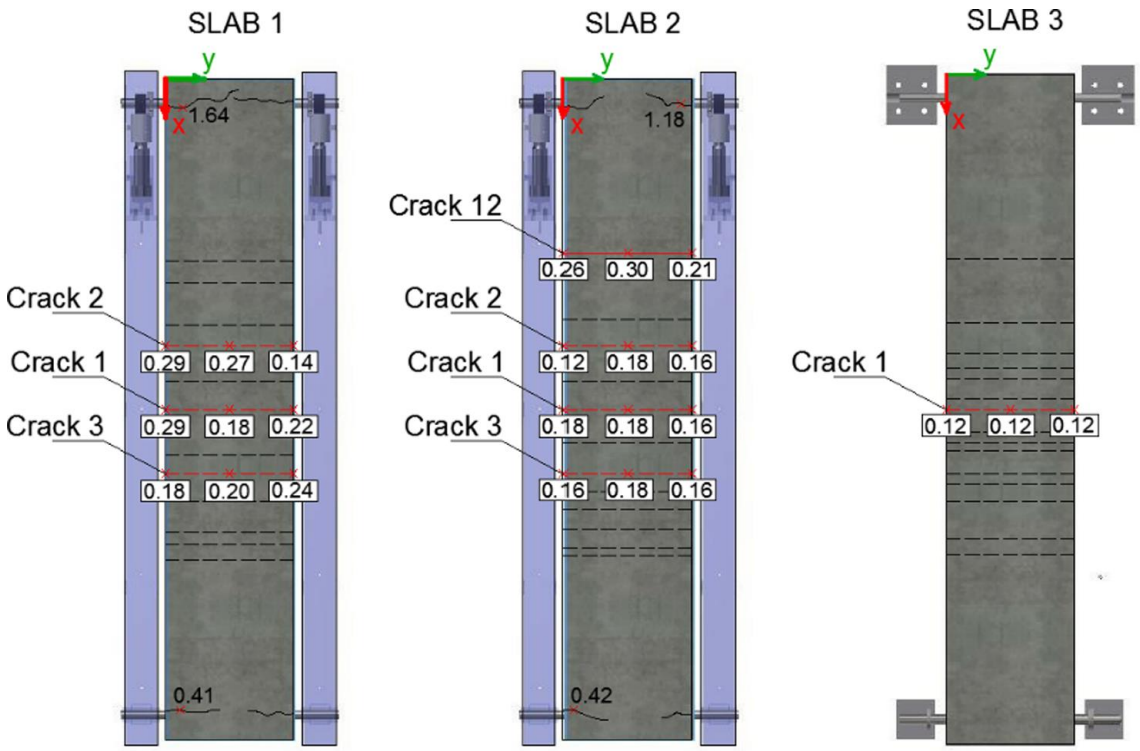

Figure 3.35 - Crack patterns and width at the end of the experimental campaign (values in mm).

Only one crack was observed on the slabs' top surface: on SLAB2: Crack 12 was formed at the age of 235 days, spaced approximately 0.60m from the mid-span. The occurrence of this crack is responsible for the sudden variation of the average deformation in the control region, revealed in Fig. 3.22. This crack does not cross the entire height of the slab (thus inducing a negative curvature in that zone). Since the applied bending moments are positive (yet small, due to the proximity to the support), the crack was not expected to appear in the top surface. It may be justified by a lower tensile strength of the top concrete layer, in that position.

SLAB1 and SLAB2 are, as expected, heavily cracked on the support region due to high tensile stresses induced by the application of the restraint load since the age of 10 days.

Figs. 3.36-3.37 show the evolution of the maximum crack width (maximum value recorded over the crack length), for all the observed cracks (except those in the supports regions) in the restrained (SLAB1 and SLAB2) and unrestrained (SLAB3) specimens, respectively.

For the restrained slabs, the main cracks at the bottom surface (Cracks 1–3) were induced after application of the restraint force and detected at the ages of 16, 23 and 42 days, respectively. The width of these cracks increases significantly (from 0.06mm up to 0.08 mm) in SLAB1 during the period between 50 and 60 days, in which the vertical loads are applied and the required axial load for a situation of full restraint is reinstalled. After 60 days, age from which the restraint force and the vertical loading are constant for both slabs, the maximum crack width continues to increase (from 0.05mm up to 0.08 mm) until stabilizing around 1 year of age. Regarding SLAB2, the crack opening stabilization takes place earlier for Cracks 1–3, around 235 days, when the top surface crack (Crack 12) is induced. After that age, crack width development on the control region of SLAB2 occurs almost exclusively on Crack 12 until roughly 1 year of age.

It should be noted that the cracking development of SLAB1 is higher than SLAB2: the difference between the summed crack widths, measured in the 3 main cracks of both slabs, varies between 0.02mm (at 16 days) and 0.08mm (at 50 days). However, the same axial load is applied on both slabs during this period. This seems to indicate that the development of these cracks can be significantly affected by the very small variation of concrete tensile strength between two different specimens of the same cast. This effect is particularly relevant during the crack formation stage, when the softening behaviour of concrete plays an important role in the structure response of the crack cross section.

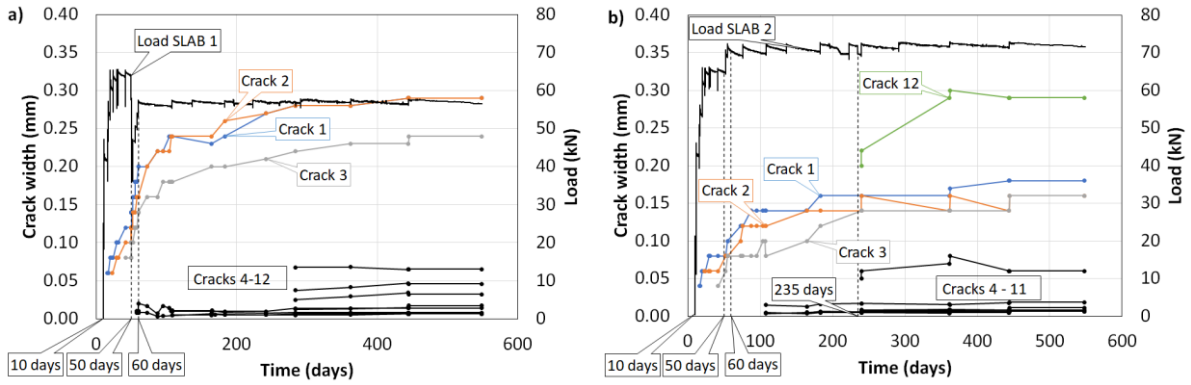

Figure 3.36 - Evolution of maximum crack width: a) SLAB1 and b) SLAB2.

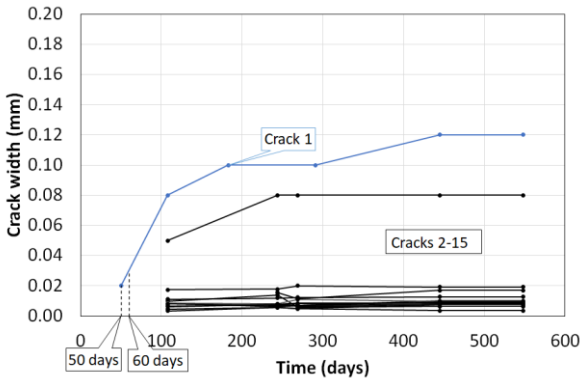

Figure 3.37 - Evolution of maximum crack width – SLAB3.

On the unrestrained slab (SLAB3), only one main crack is induced at mid-span after application of vertical loads at 50 days, developing a crack width up to 0.12mm by the end of the experimental campaign – see Fig. 3.37.

3.5.6 Axial strains in the control region

Fig. 3.38a shows the average axial strains measured in the control region of the three tested slabs (as measured by the lateral longitudinal LVDTs), as well as the average drying shrinkage measured in the dummy specimens. Even though the same axial force was applied to both restrained slabs during the first 50 days, SLAB1 exhibited wider cracks (as shown in Section 3.5.5), and consequently lower compressive strains in the control region during that period, when compared to SLAB2. From 50 days onwards SLAB2 was subjected to higher restrain loads, whereas SLAB1 was subjected to higher bending moments (due to application of the additional vertical load in SLAB1). The axial strain in the control region measured in SLAB2 was always greater than in SLAB1 until 235 days, when Crack 12 is induced on the top surface of SLAB2, resulting on a decrease of the compressive strain in the control region of 34 με.

Significant differences between measurements of the strains on both sides of the same slab were observed (Fig. 3.39b), indicating in-plane bending of the slabs. This behaviour of concrete members subjected to axial tensile loads during the crack formation stage is due to the fact that the structural response in not purely symmetrical, since the crack width is not constant over the transverse slab direction. After initial cracking, both slabs show parallel increases of the deformations at each side.

The axial strain in the control region of the unrestrained slab (SLAB3) progresses at a lower rate than the free shrinkage measured on the dummies, due to the internal restraining of the reinforcement, in a first stage, and because of the effect of the flexural cracking after application of the vertical load at the age of 50 days.

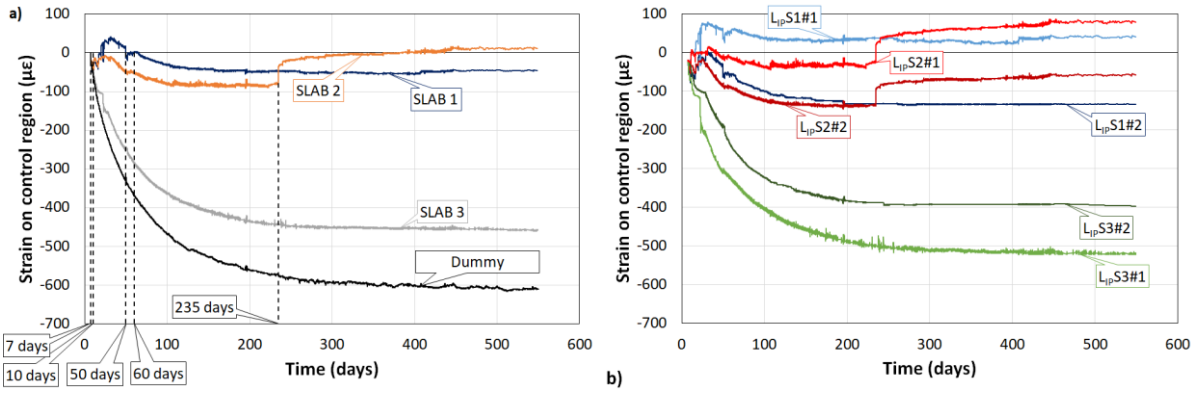

Figure 3.38 – Evolution of longitudinal strain on control region: a) average measurements and b) measurements on both sides.

3.5.7 Vertical deformation

Evolutions of the vertical displacement in different locations of SLAB1 (at mid-span and on the control region boundaries), and comparison of the vertical displacement in the three slabs is reproduced in Fig. 3.39.

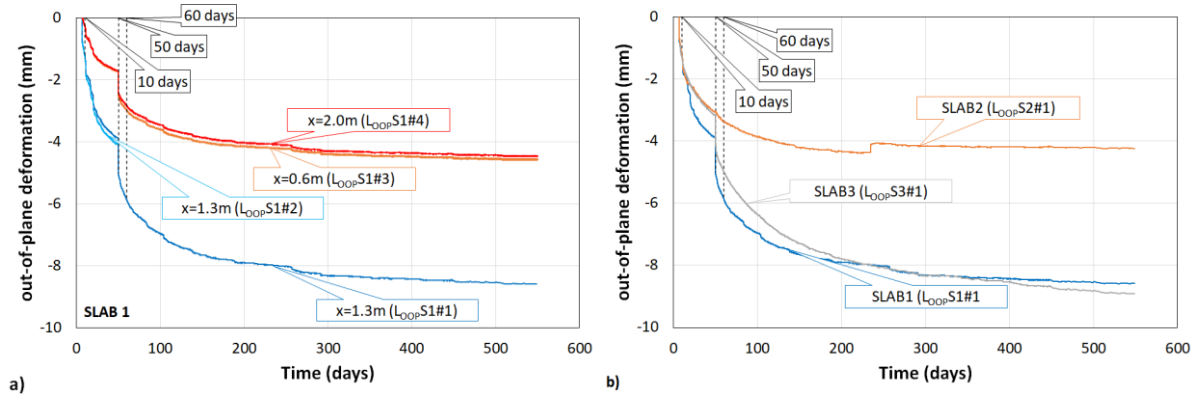

Figure 3.39 – Evolution of vertical displacement: a) SLAB1 and b) SLAB1, SLAB2 and SLAB3 (at mid-span).

During the formwork removal the vertical displacement measured on SLAB1, SLAB2 and SLAB3, at mid-span, were 0.74mm, 0.70mm and 0.80mm, respectively.

Between the ages of 10 and 50 days (i.e., between the start of the axial restraint and the application of the vertical loading), all the slabs were submitted to the same dead weight. The deflection is not equal in the three slabs because of two opposite influencing factors: on one hand, slabs with higher crack widths experience a higher stiffness reduction and consequently deflect more; on the other hand, the axial force applied to SLAB1 and SLAB2 contributes to a reduction of the deflection due to a geometric non-linear effect.

It is worth noting that, even though SLAB1 and SLAB2 are subjected to similar axial stress and vertical load during the first 50 days, a higher vertical displacement was recorded for SLAB1 during that period because of the wider cracking observed in that slab. This is corroborated with measurements of longitudinal strains in control region, as shown in Fig. 3.40, where, for both slabs, the evolution of vertical displacement at mid-span and the evolution of longitudinal strains in the control region during the first 50 days are presented in more detail. It can be observed that, for the same axial force applied in both slabs, SLAB1 starts presenting less compressive strains and higher vertical displacement at approximately 16 days, thus indicating a loss of stiffness in relation to SLAB2 at that age.

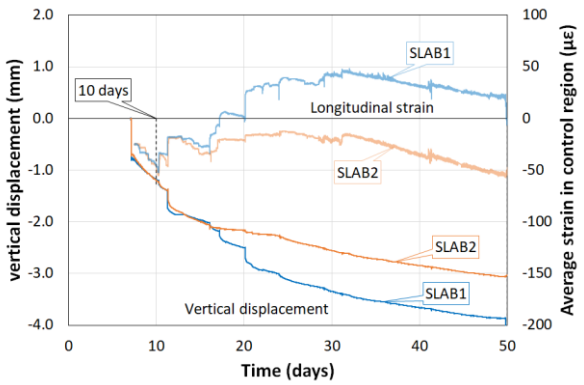

Figure 3.40 – Vertical displacement at mid-span and longitudinal strain on control region, during the first 50 days, recorded in SLAB1 and SLAB2.

During the application of the vertical loading, at 50 days, vertical displacements of 1.13mm and 0.82mm were observed at mid-span on SLAB1 and SLAB3, respectively. This difference of approximately 0.3mm can be justified by the different level of cracking observed in both slabs immediately before application of the vertical loads (i.e., higher cracking level in SLAB1, and consequent smaller stiffness in relation to SLAB3, resulted in a higher instantaneous vertical displacement during application of the vertical loading).

Results from LVDTs L_{00P}S1#2 and L_{00P}S3#2, used to assess the repeatability of measurements of vertical displacement at mid-span during the first 50 days in SLAB1 and SLAB3, respectively, showed a good

agreement with the measurements from LVDTs L_{00P}S1#1 and L_{00P}S3#1, with a maximum difference of 0.2 mm, observed in SLAB1 at 50 days. Settlement of the supports (at position x = 2.5 m), registered by the LVDTs during the application of the vertical loads on SLAB1 and SLAB3, were 0.10mm and 0.15mm, respectively, and did not increase until the end of the experimental campaign.

The vertical displacement at mid-span develops at a higher rate on SLAB3 after application of the vertical loading, and at the age of ~350 days it exceeds the deformation measured on SLAB1, even though a very small difference (0.30 mm) is observed at the end of analysis. These slabs are submitted to the same vertical loading. The results show that the highest stiffness decrease of SLAB1 due to cracking (by comparison with SLAB3) is almost entirely compensated by the geometric non-linear effect installed on this slab.

On SLAB2 a decrease of the vertical displacement at mid-span is observed at the age of 235 days, when Crack 12 is formed on the top surface of the slab, due to the negative curvature induced by that crack.

3.6 Discussion of results

In the present section the results provided by different sensor types are cross compared, for a deeper understanding and explanation of the observed structural behaviour. This discussion complements the comments written in Section 3.5 about the results provided by each sensor type.

During the first 7 days, before formwork removal, the slabs were not subjected to any kind of vertical loading or external restraint to axial deformations (the formwork system is flexible enough to allow the longitudinal deformation of the slabs). Moreover, the temperature rise due to cement hydration was small and the temperature gradient (across the slab thickness) was negligible, as shown in Fig. 3.25. Therefore, no significant concrete stresses were expected during that phase.

When the formwork was removed, at the age of 7 days, and since no cracking was induced during the activation of the self-weight, the concrete stiffness, as well as the assumed structural system, can be validated based on a comparison of the theoretical and measured responses of the slab, considering a linear elastic behaviour and a non-cracked state for the concrete. The strain variation on both the top and bottom rebars, ε_s, and the vertical displacement of the slab, δ_{slab} , both at mid-span, can be computed as [148]:

$$\varepsilon_s = \frac{\alpha \cdot M}{I_{ci} \cdot E_s} \cdot z \qquad \text{(Eq. 3.6)}$$

$$\delta_{slab} = \frac{5 \cdot p \cdot L^4}{384 \cdot E_c \cdot I_{ci}} \quad \text{(Eq. 3.7)}$$

where α is the modular ratio $\frac{E_s}{E_c}$, E_s and E_c are, respectively, the modulus of elasticity of steel and concrete (N/m²), I_{ci} is the second moment of area of the RC section of the slab (m⁴), M is the bending moment at mid-span (N.m), z is the position of the strain gages (according to Table 3.2), p is the distributed load (N/m) and L is the free span length of the slab (m).

The strain variation observed experimentally for all sensors (ranging between ~17 to ~23 με) are in line with the strain variation computed with Eq. 3.6 (assuming a concrete modulus of elasticity for concrete, at 7 days, of $E_c(7d) = 26.1\ GPa$, a modulus of elasticity for steel of $E_s = 200\ GPa$ and a distributed load due to the self-weight of $p_{self-weight} = 1.25\ kN/m$), with an error less than ± 2.5 με.

The vertical displacement measured during formwork removal ranged between 0.70mm and 0.80mm. Even though the theoretical displacement provided by Eq. 3.7 is 0.50 mm, the excess of vertical displacement measured can be justified by the filling of the slack at the support of the steel rod and the deformability of the steel rod. This additional displacement is, however, negligible when compared to the maximum value observed at long-term (8.7 mm).

After formwork removal, the average longitudinal strain of the slabs was measured in the control region, throughout the entire experimental campaign. The reliability of the devised measurement system can be assessed by comparing the measured average strain, $\varepsilon_{G,exp}$, with the calculated value based on other sensor results, as explained in the following paragraphs.

The strain at mid-height, $\varepsilon_G(t)$, can be estimated based on the strains measured at the top and bottom rebars, $\varepsilon_{s,t}(t)$ and $\varepsilon_{s,b}(t)$, assuming a linear strain variation in the mid-span cross-section (only valid before cracking):

$$\varepsilon_G(t) = \varepsilon_{s,b}(t) + \frac{\varepsilon_{s,t}(t) - \varepsilon_{s,b}(t)}{z_t - z_b} \cdot (z_G - z_b) \quad \text{(Eq. 3.8)}$$

where z_G, z_b and z_t are the z-coordinates of the measurement points in the axes system indicated in Fig. 3.2.

The theoretical longitudinal deformation $\varepsilon_G(t)$ can also be estimated based on the measured drying shrinkage of concrete, considering the effects of internal restraint due to the reinforcement [40]:

$$\varepsilon_G(t) = \frac{\varepsilon_{sh}(t)}{1 + \frac{\frac{E_s}{E_c(t_i)}}{\frac{1}{1+\varphi(t,t_i)\cdot\chi(t_i)}} \cdot \rho_s} \quad \text{(Eq. 3.9)}$$

where $\varepsilon_{sh}(t)$ is the average free shrinkage measured on the dummy specimens, $\varphi(t,t_i)$ is the creep factor (according to the EC2 formulation), $\chi(t_i)$ is the aging factor, ρ_s is the reinforcement ratio, t is the instant of analysis (days) and t_0 is the loading age (t_0 = 7 days, corresponding to the instant when slabs are exposed to drying).

Comparison of the average longitudinal strain measured on the control region throughout the experimental campaign, $\varepsilon_{G,exp}(t)$, with the estimated strains according to Eqs. 3.8 and 3.9 are shown in Fig. 3.41 for SLAB1 and SLAB2, and in Fig. 3.42 for SLAB3.

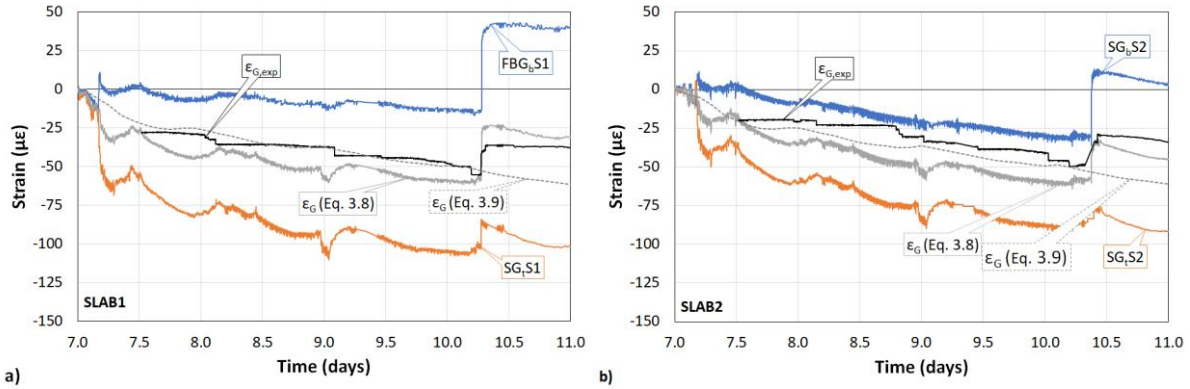

Figure 3.41 – Average longitudinal strain on the control region: experimental vs. estimated values for a) SLAB1 and b) SLAB2

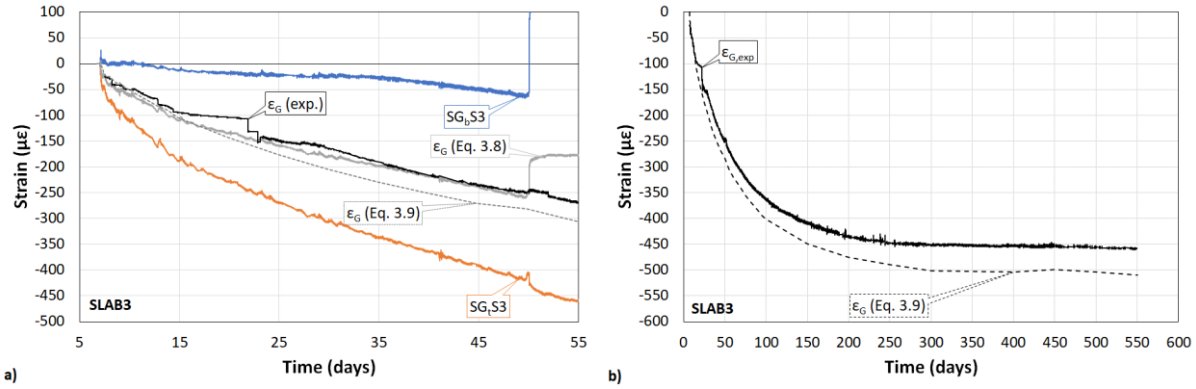

Figure 3. 42 – Average longitudinal strain on the control region: experimental vs. estimated values for SLAB3: a) between 5 and 55 days and b) throughout the experimental campaign.

It can be observed that, before cracking being induced at mid-span (10 days for SLAB1 and SLAB2, and 50 days for SLAB3), there is a reasonable correlation between the experimental and the estimated evolution of the longitudinal strains over time, which demonstrates consistency between measurements of the drying shrinkage in the dummy specimens, the rebar strains at mid-span and the in-plane deformation on the control region.

After cracking occurrence, the neutral axis at mid-span changes its position, and a comparison between the experimental strain and the estimations from Eq. 3.8 is no longer appropriate. The same applies for

the estimation of in-plane deformations according to Eq. 3.9. Fig. 3.42b shows a comparison between the aforementioned prediction and the experimental strain measured on the control region of SLAB3, throughout the entire experimental campaign. It can be observed that, as cracking develops in SLAB3 after application of the vertical loads, the experimental and estimated curves get further apart. This difference between the two curves reflects the effect of cracking in SLAB3 on the longitudinal deformation measured on the control region that is not considered in Eq. 3.9. SLAB1 and SLAB2 present an even more complex behaviour that cannot be analysed with simple calculations. The prediction of the structural behaviour of these slabs can only be performed with models that take into account the relationship between material properties (changing over time), the applied loads, the effect of cracking and the imposed deformations.

The calculation of strains at the mid-span section of SLAB1, at 550 days, considering a cross-section in the cracked state, lead to the following results (assuming an effective E-modulus $E_{c,eff} = 6.7\ GPa$, the influence of concrete in tension, with a tensile strength $f_{ct,eff} = 2.7\ Mpa$, a restraint axial force $N = 57\ kN$ and an acting bending moment of $M = 1.95\ kN.m$): (i) the neutral axis depth is 0.022 m; (ii) the compressive strain of the concrete at top surface is ε_c = -515 με ; (iii) the strains in the reinforcement bars are at the top layer ε_t = 86 με and at the bottom layer ε_b = 1195 με, respectively. These theoretical strains are significantly different from the average strains measured experimentally at mid-span of SLAB1, with sensors SG_tS1, $SG_bS1\#1$, $SG_bS1\#2$ and FBG_bS1. In detail, the strain measurements indicated a compressive strain in the top rebar of -300 με and tensile strains varying between 611 με and 941 με on bottom rebars – see Fig. 3.43.

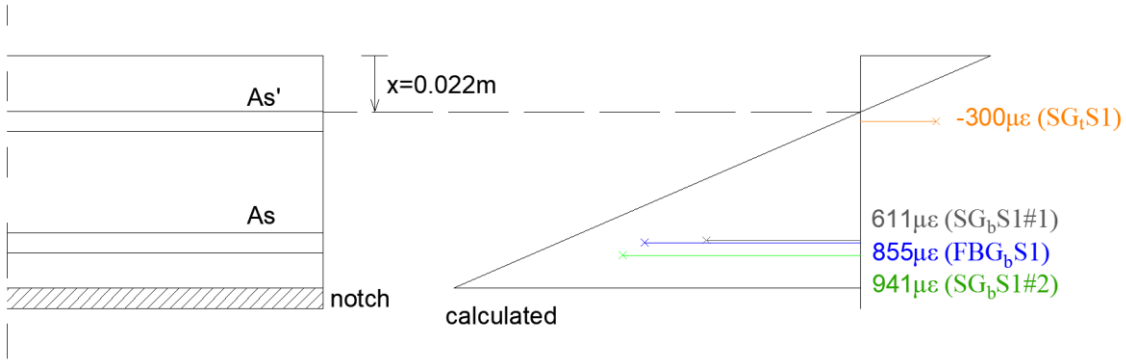

Figure 3.43 – Strain distribution over the height of SLAB1 cross-section at mid-span: experimental vs simplified analysis.

A fundamental difference between calculated strains in the analysed cross section and measured strains on the reinforcement is the difference between calculated punctual maxima (obtained with a cross-sectional analysis) and measured average strains (obtained with a strain gauge depending on the length of its measurement basis). Concluding, the measured strains are always smaller than the calculated

strains as long as the measurement basis is affected by bond action between reinforcement and concrete. In addition, the measured strains are reduced if the crack does not meet the exact location of the strain gauge. The differences between measurements of steel strains on the bottom rebars are most likely to be caused by both effects, as the crack width is only ~0.23mm compared to the length of the measurement basis of 5mm and the position of the sensor is different in relation to the crack (due to the irregular nature of a crack). Moreover, the influence of the concrete drying shrinkage on these results cannot be predicted with simplified methods. Therefore, further complex models are required to adequately analyse these steel strains, as well as to compare the consequent crack width predictions (based on relative strains between concrete and steel) with the experimental results. Such analysis is performed in the scope of Chapter 4 of this work.

A high level of restraint was imposed to both SLAB1 and SLAB2 throughout the entire experimental campaign, with periodical application of pre-defined axial loads. Considering that SLAB1 and SLAB3 have the same history regarding application of self-weight and remaining vertical loads, the evolution of the degree of restraint a on SLAB1 can either be determined based on the absolute or incremental longitudinal strains measured on the control region of both slabs:

$$a(t_n) = 1 - \frac{\varepsilon_1(t_n)}{\varepsilon_3(t_n)} \qquad \text{(Eq. 3.10)}$$

$$a(t_n - t_{n-1}) = 1 - \frac{\varepsilon_1(t_n) - \varepsilon_1(t_{n-1})}{\varepsilon_3(t_n) - \varepsilon_3(t_{n-1})} \qquad \text{(Eq. 3.11)}$$

where t is the time (days), ε_1 is the strain on the control region for SLAB1 and ε_3 is the strain on the control region for SLAB3. Fig. 3.44 shows the evolution of the absolute degree of restraint, as well as the incremental degree of restraint over periods of 30 days until 250 days (after this instant, the longitudinal strain on both SLAB1 and SLAB3 are constant). It can be observed that the axial load that was necessary to completely restrain SLAB1 was overachieved during the period between 20 and 50 days, and a maximum degree of restraint of a = 1.2 was reached. After application of the vertical loads at 50 days, the absolute degree of restraint achieved in the control region of SLAB1 was roughly constant throughout the experimental campaign, and close to a situation of full restraint (a = 0.9), even though a significant variation of the incremental degree of restraint can be observed throughout the experimental campaign.

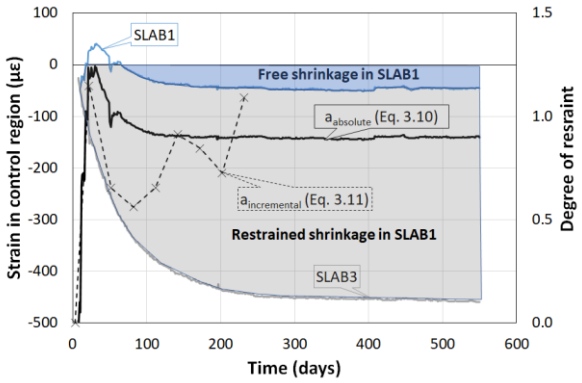

Figure 3.44 – Evolution of degree of restraint in SLAB1.

The axial load applied to SLAB1 to ensure the abovementioned restraint condition (57 kN) represents 42% of the cracking force of the concrete ($N_{cr} = A_c \cdot f_{ctm} = 0.05 \times 2.7 = 135\ kN$). This value is in line with most studies on numerical simulation of longitudinally restrained slabs subjected to service vertical loading, in which the restraint force induced on the slabs due to restrained deformation ranges between 30% and 60% of N_{cr}, for different approaches [13–17].

Chapter 4

Validation of numerical approaches

4.1 Introduction

In this Chapter, the structural behaviour of the tested slabs presented in Chapter 3 is simulated with two different approaches. Firstly, the non-linear FE based 3D multi-physics simulation presented in Chapter 2, in which the non-uniform shrinkage field of the slab's cross section is regarded, is employed. Such approach enables a detailed characterization of the specimen's stress field over time, however, it requires a comprehensive material characterization and experience regarding non-linear structural modelling, making it more suitable solution in the context of scientific investigation. A second approach based on the compatibility of deformations of a sectional analysis is then described and employed to predict both restraint force and maximum crack width.

4.2 FE based 3D multi-physics simulation

In this sub-chapter, the abovementioned FE based analysis framework is applied to simulate the hygro-mechanical behaviour of the 3 slabs tested in the experimental campaign presented in Chapter 3. Since the experiment is performed under constant ambient temperature and the slabs don't endure significant stresses until stabilization of concrete temperature with the environment, the thermal analysis is disregarded.

Firstly, the hygrometric analysis is presented in sub-section 4.2.1. The diffusion parameters are estimated with a back-analysis based on the measurements of relative humidity profiles and a formulation for assessment of relative strains as a function of the relative humidity is calibrated based on the free shrinkage measured on dummy specimens. The non-uniform shrinkage field calculated in the hygrometric analysis is then simulated with fictitious temperature attributed to the mesh nodes of the 3D mechanical model described in sub-section 4.2.2. Results and final considerations regarding the analysis performed in this sub-chapter are addressed in sub-section 4.2.3.

4.2.1 Hygrometric simulation

4.2.1.1. Calibration of diffusion parameters

Since the humidity flow is unidirectional along the specimens H10 and H15, for measurement of the relative humidity profiles, the prisms represented in Fig. 4.1, with a length equal to the specimen's depth

(10cm for H10 and 15cm for H15), were modelled considering 4 isolated planes in the longitudinal faces, across which no flux is allowed.

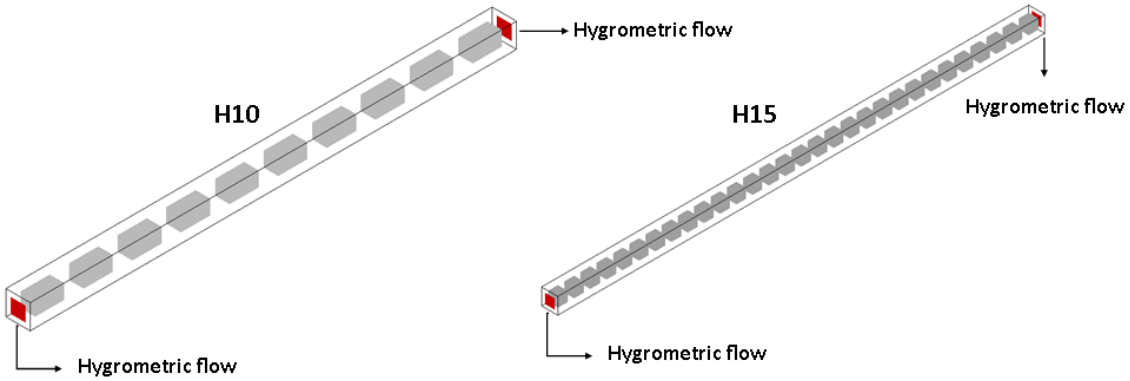

Figure 4. 1 - FE model of 1D hygrometric flow for simulation of specimens H10 and H15.

Moisture boundary conditions were applied to top and bottom surfaces of the prism, considering a constant environment relative humidity of $H_{env} = 60\%$ and a moisture emissivity coefficient h_m equal to 4.8×10^{-8}m/s, in accordance with the calibration performed by Azenha *et al.* [141] for similar concrete composition and laboratory conditions. An initial relative humidity of the concrete equal to 97% was considered in accordance with the first measurements before exposing the specimens H10 and H15 to the environment.

The mesh used in the hygrometric model is composed by eight-nodded 3D isoparametric brick FE for potential flow analysis and four-nodded 2D isoparametric quadrilateral FE to describe the boundaries, adopting a Gauss integration.

The starting iteration for simulation of the hygrometric flow was performed with the parameters proposed by MC10 [10] for assessment of the diffusion coefficient in isothermal conditions – see Fig. 4.2.

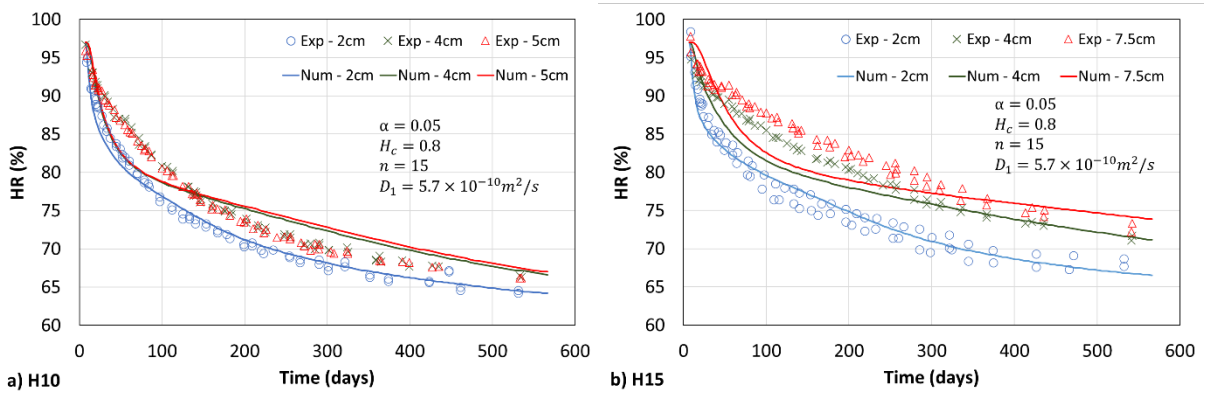

Figure 4.2 - First iteration for simulation of the humidity profiles: a) specimens H10 and b) specimens H15.

These parameters were calibrated in order to best fit the experimental humidity profiles. The final solution is shown in Fig. 4.3.

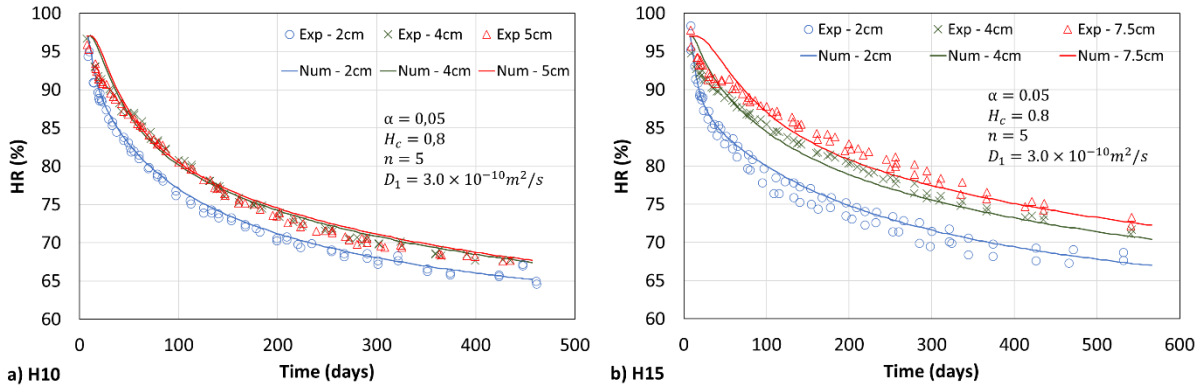

Figure 4.3 - Final iteration for simulation of the humidity profiles: a) specimens H10 and b) specimens H15.

Fig. 4.4 shows, for each depth, the numerical envelope representing the acceptable error of the numerical model. These numerical envelopes take into account the variation of the environment RH (+/-5%) and the accuracy of the Vaisala sensor probe (+/-1.5% for measurements below 90% and +/-2.5% for measurements above 90%). The numerical envelopes are limited by the numerical prediction of the relative humidity evolution over time considering $H_{env} = 55\%$ and $H_{env} = 65\%$, summed and subtracted, respectively, by the Vaisala accuracy. All experimental results should be within these limits, however, during the first month of the experimental campaign, several measurements on hight humidity profiles (above 90%) were undertaken. These measurements can impair the accuracy of the probe, which justifies the deviation of initial results from the numerical envelope, before new calibration of the Vaisala probe performed on 10 June of 2018 (see Fig. 4.5).

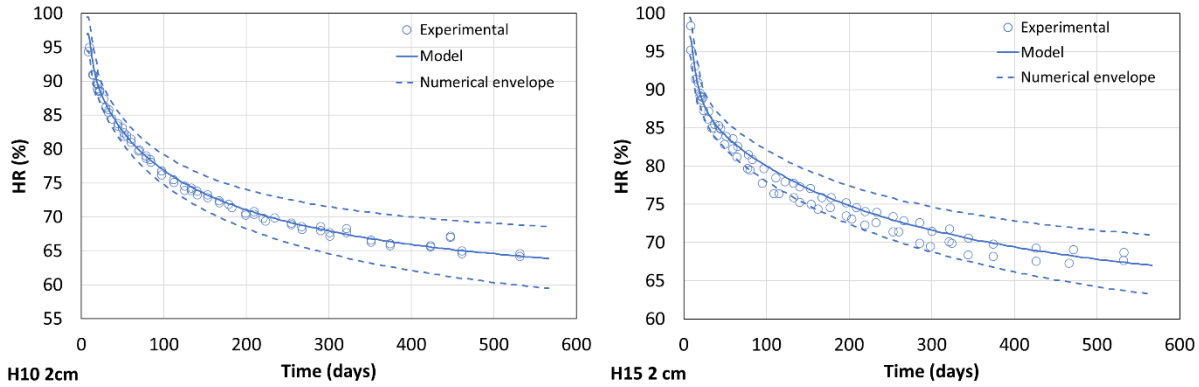

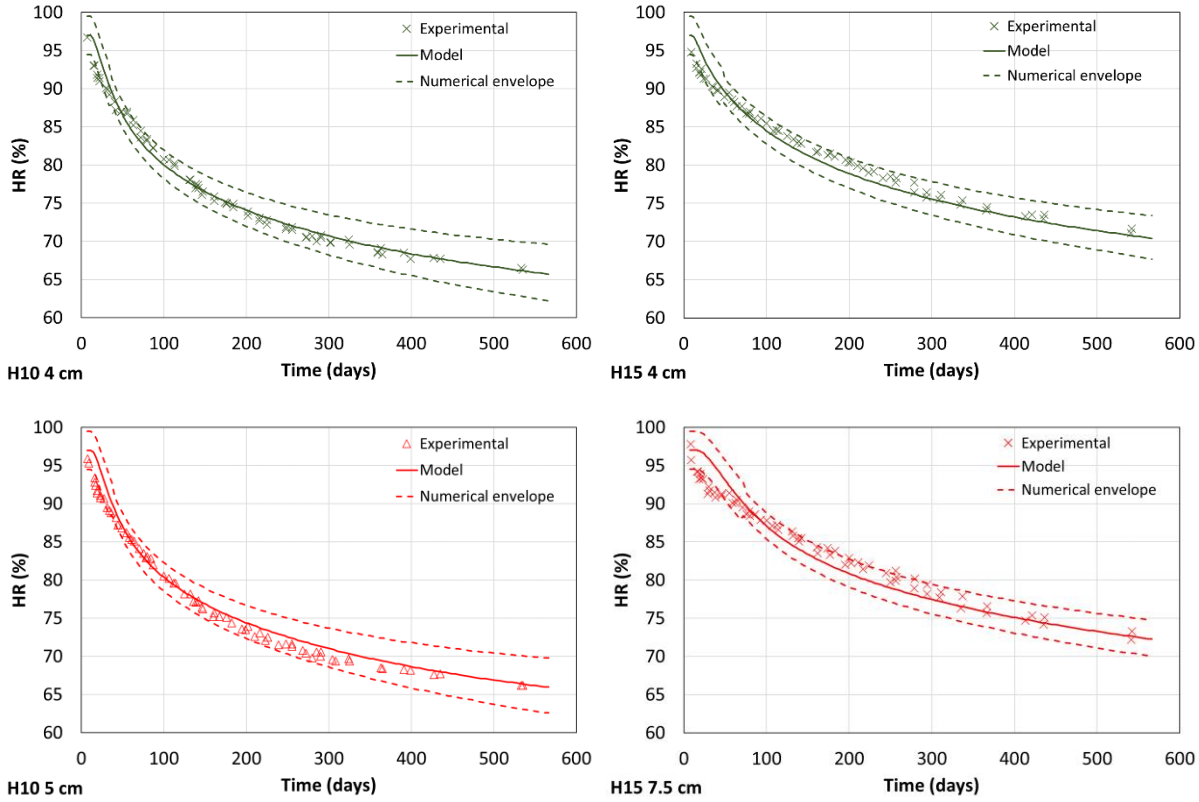

Figure 4.4 - Numerical envelope of hygrometric analysis and experimental results.

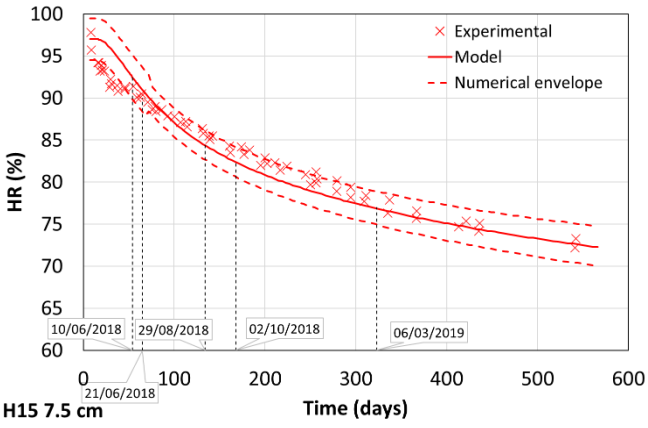

Date	Calibration salt	Measured value (%)	Considered value (%)
10/06/2018	LiCl	11.25	11.30
	K2SO4	97.34	97.60
21/06/2018	LiCl	11.60	11.30
	K2SO4	97.90	97.60
29/08/2018	LiCl	11.10	11.30
	K2SO4	97.97	97.60
02/10/2018	LiCl	11.41	11.30
	K2SO4	97.39	97.60
06/03/2018	LiCl	11.46	11.30
	K2SO4	97.54	97.60

Figure 4.5 - Calibration of the sensor during the experimental campaign.

4.2.1.2. Simulation of the specimen's relative humidity and shrinkage field

The calibrated diffusion parameters were used to simulate the hygrometric flow of the dummy and slab specimens. It was considered a 2-dimesional hygrometric flow and the humidity field of the transversal cross section of the slab (0.5×0.1m²) was simulated with the FE mesh presented in Fig. 4.6, which was envisaged to match the nodes of the mesh for the mechanical model, to be presented in the next sub-

section. It is more refined in the cross-section edges (over 5cm) as the hygrometric flow in this region is more complex (at the central region, the hygrometric flow is virtually 1-directional).

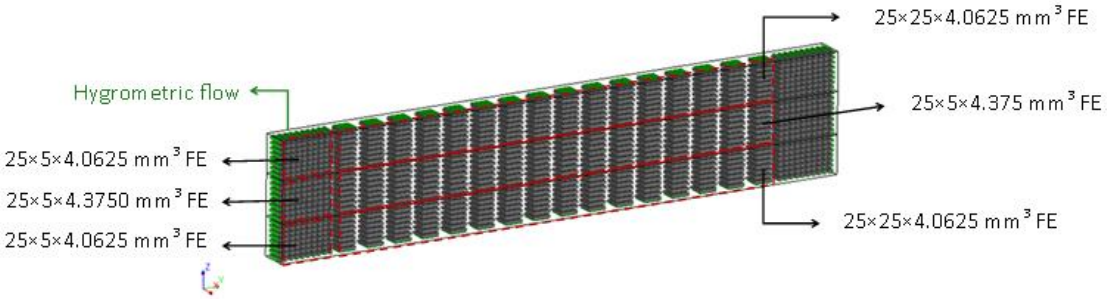

Figure 4.6 – FE mesh for simulation of the hygrometric field in the specimen's cross section.

The mesh used in the hygrometric model is composed by eight-node isoparametric brick elements for potential flow analysis and four-node isoparametric quadrilateral elements to describe boundaries in the potential flow analysis, both based on linear interpolation and Gauss integration.

The calculated evolution of the relative humidity over time at the centre of the cross-section, over its thickness (10cm) and width (50cm), is shown in Fig. 4.7 for different depths.

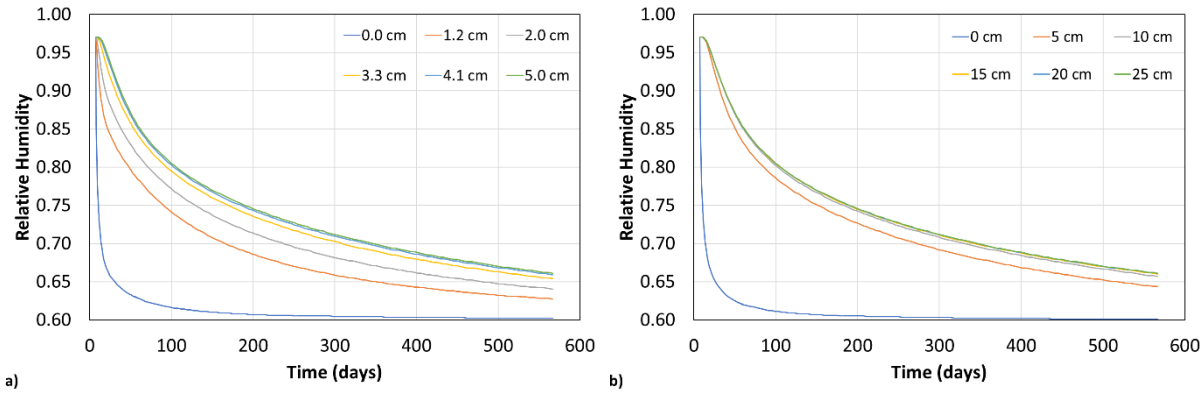

Figure 4.7 – Evolution of relative humidity over time at the centre of the cross-section, over its: a) thickness, b) width.

The internal humidity calculated at each point of the FE mesh is converted to an imposed drying shrinkage strain in accordance with the formulation proposed by Kwak *et al.* [119] (Eq. 2.9). The ultimate shrinkage of concrete upon total drying $\varepsilon_{sh,ult}$ is estimated with the Eurocode 2 formulation for determination of concrete shrinkage, adjusted to the experimental measurements of the dummy specimens by adding two calibration factors: i) time function $\beta_{ds}(t, t_s)$ is adjusted with factor k_1 according to Eq. 4.1., ii) the basic drying shrinkage strain $\varepsilon_{cd,0}$ is adjusted with factor k_2 according to Eq. 4.2.

$$\beta_{ds}(t, t_s) = \frac{(t-t_s)}{(t-t_s)+k_1 \cdot 0.04 \cdot \sqrt{{h_0}^3}} \qquad \text{(Eq. 4.1)}$$

$$\varepsilon_{cd,0} = \frac{k_2 \cdot 0.85\left[(220+110\cdot\alpha_{ds1})\cdot exp\left(-\alpha_{ds2}\cdot\frac{fcm}{10}\right)\right]\cdot\beta_{RH}}{10^6} \qquad \text{(Eq. 4.2)}$$

The values of k_1 and k_2 that best fit the experimental measurement of the average dummy shrinkage are, respectively, 1.15 and 0.96, as shown in Fig. 4.8.

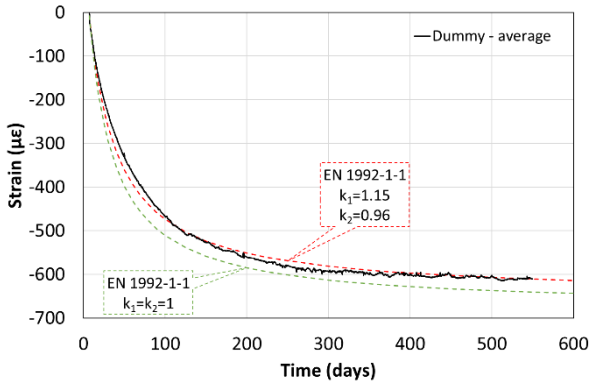

Figure 4. 8 – Average strain measured on dummy specimens and prediction according to EC2 formulation.

A value of $\varepsilon_{sh,ult} = 860\mu\varepsilon$ is then estimated as the total shrinkage at long-term, calculated with the calibrated formulation of EC2 and considering an ambient RH of 0%. The calculated evolution of shrinkage over time at the centre of the cross-section, over its thickness (10cm), is shown in Fig. 4.9 for different depths.

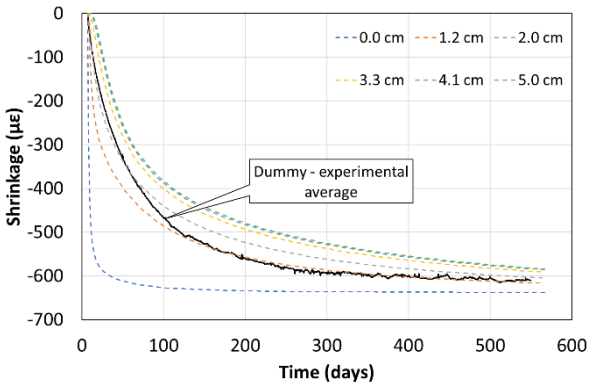

Figure 4.9 - Evolution of shrinkage over time at the centre of the cross-section, over its thickness.

4.2.2 Mechanical Simulation

The evolution of the modulus of elasticity of concrete is simulated based on the formulation of EC2 [6]: $E(t) = E(28)\cdot\left[exp\left(s\cdot\left(1-(28/t)^{0.5}\right)\right)\right]^{0.3}$, adapted to fit the results obtained experimentally ($s = 0.46$ and $E(28) = 29.8GPa$).

The viscoelastic behaviour of concrete (elastic and creep deformations) is simulated through the Kelvin chain model presented in sub-section 2.3.3.1, calibrated to fit the experimental creep curves obtained for

loading ages at 8 and 50 days, considering $N = 9$ Kelvin units with retardation times $\tau_\mu = 0.001 \times 10^{\mu-1}$ days. Fig. 4.10a shows the specific creep simulated with the calibrated Kelvin chain model compared with the experimental results and Fig. 4.10b shows the modulus of elasticity of each Kelvin unit per loading age.

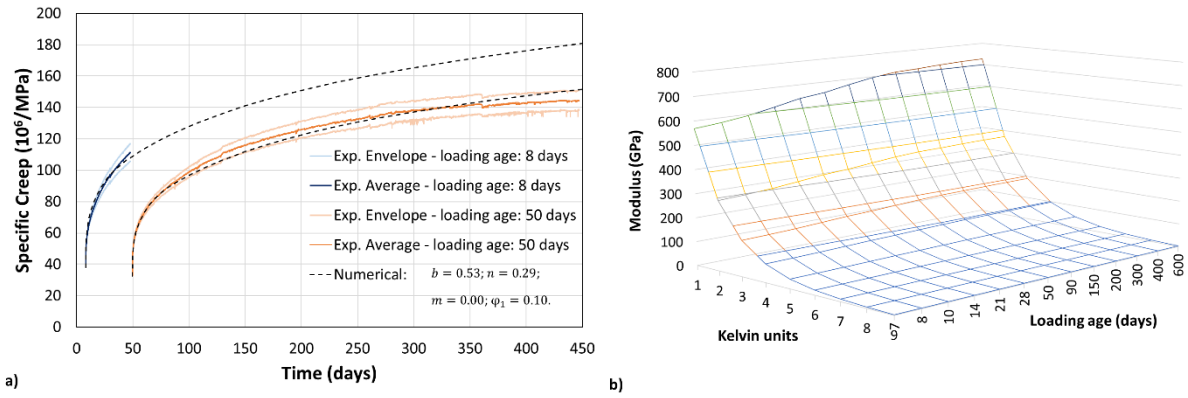

Figure 4.10 – Comparison of experimental creep functions and numerical simulation based on the adjusted Kelvin chain model (a) and three-dimensional graph depicting the modulus of elasticity of each Kelvin unit as a function of the loading age (b).

The evolution of concrete tensile strength over time is simulated with the formulation of EC2 [6]: $f_{ctm}(t) = f_{ctm}(28)\left[exp\left(s \cdot (1 - (28/t)^{0.5})\right)\right]^{\alpha}$, where $\alpha = 1$ when $t < 28\ days$, $\alpha = 2/3$ when $t \geq 28\ days$, $s = 0.2$ in accordance with a class R cement and $f_{ctm}(28)$ is the tensile strength at 28 days of age.

A value of $f_{ctm}(28) = 2.5MPa$ was determined by applying a reduction of 10% of the tensile strength value that bests fits the experimental results (see Fig. 4.11). This reduction intends to take into account the Weibull's statistical theory of size effect considering that, for both splitting tensile tests and 3 point bending tests for assessment of the tensile strength, the tension that leads to failure of the test specimen is applied on the central cross section. A 10% reduction is in line with the results from an inter-comparison undertaken in the EC Measurement and Testing Programme, under contract MAT 1-CT-94-0043, between 3 point bending tests and 4 point bending tests [149].

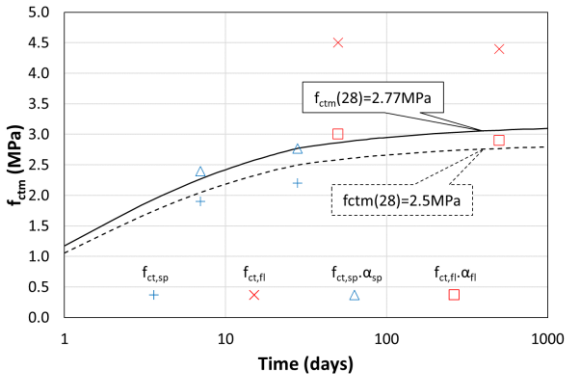

Figure 4.11 – Hypotheses for evolution of the tensile strength of concrete over time.

Table 4.1 resumes the evolution in time of the main properties of concrete considered in the crack model for the mechanical FE analyses. It should be noted that the value of the transfer length that is considered corresponds to half of the crack spacing measured experimentally

Table 4.1 – Evolution of concrete properties over time.

Property	Age (days)				
	7	**28**	**50**	**100**	**550**
Fracture Energy G_F [10] (N.m)	128	131	132	133	135
Tensile strength f_{ctm} [6] (MPa)	2.05	2.50	2.60	2.66	2.77
Transfer length L_s (m)			0.125		
Coefficient β [10]			0.4		

.The adopted FE mesh for the mechanical analyses in DIANA software, represented in Fig. 4.12, is composed by solid FE of type CHX60 [112], with 20 nodes and an integration scheme of 3×3×3 Gauss points.

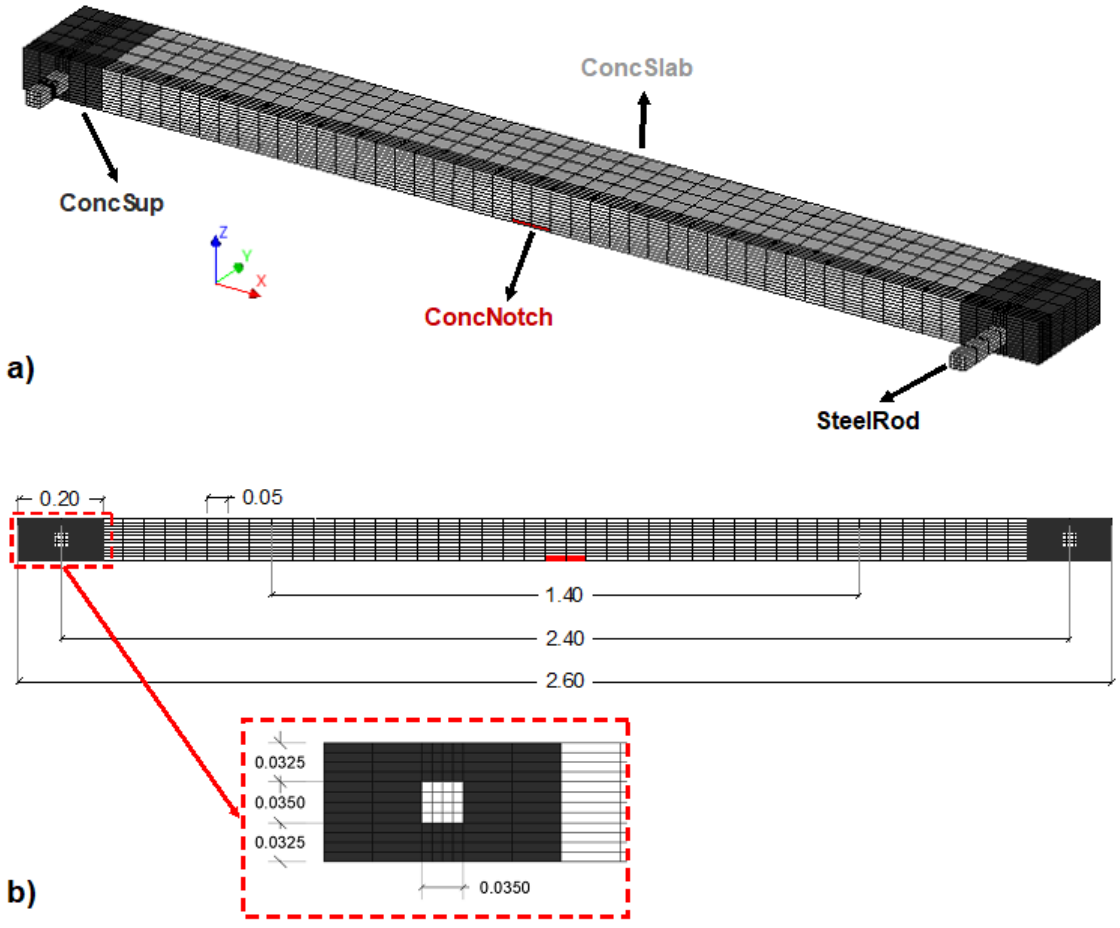

Figure 4. 12 – FE mesh of the mechanical model: a) Perspective view and b) side view.

The mesh is divided by 12 FE over the slab's thickness (4 FE with 35⁄4= 8.750mm in the centre and 8 FE with 32.5⁄4= 8.125mm at the bottom and top). The FE's length is 50mm and the width varies between

10mm (within the 5cm of the edge) and 50mm (in the central region). The 40mm diameter steel rods (supporting the slabs) are modelled with a 0.35×0.35m² cross-section parallelepiped (same moment of inertia of the 40mm cylinder) to facilitate the generation of a regular mesh.

The support region *ConcSup* has a length of 0.2m and the cracking model is disabled for the FEs in this region to avoid cracking localization near support, allowing distribution of tension over the slab's cross section (it should be noted that anchoring of longitudinal reinforcement around the steel rods is not simulated in the mechanical model). The FEs labelled *ConcNotch* have a tensile strength equal to 85% of the remaining slab material *ConcSlab*, in order to account for the 1.3cm width and 0.8cm high triangular notch at midspan. The FEs labelled *SteelRod* materialize the steel rods of the test specimen, in which a yield stress f_{sy} of 500MPa and Modulus of elasticity E_s of 200GPa are considered.

Structural symmetry of the slab is applied to optimize the numerical analysis: only half of the slab is modelled, and a symmetry plane is considered at the centre of the slab's cross-section, parallel to x and z directions – see Fig.4.13.

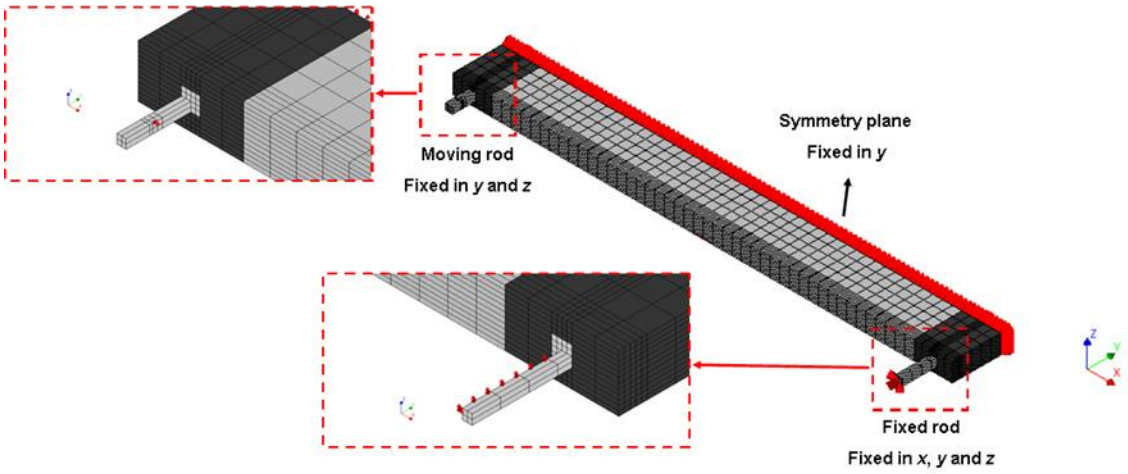

Figure 4.13 – Supports and symmetry condition of the mechanical model.

The fixed rod is fixed in x, y and z directions, over a length of 15cm, at the centre of the fixed rod. The moving rod is fixed in y and z directions, at the point of contact between the radial ball bearing and the steel rod. The axial force is uniformly applied over a line with a length of 4.5cm (width of the ring nut that connects the actuator and the moving rod).

The analyses start at 7 days of age, when the formwork is removed, and the slabs are subjected to self-weight and drying shrinkage. The loading phasing follows strictly the axial and vertical loads applied to each slab in the experimental campaign, as shown in Fig. 4.14 and Table 4.2.

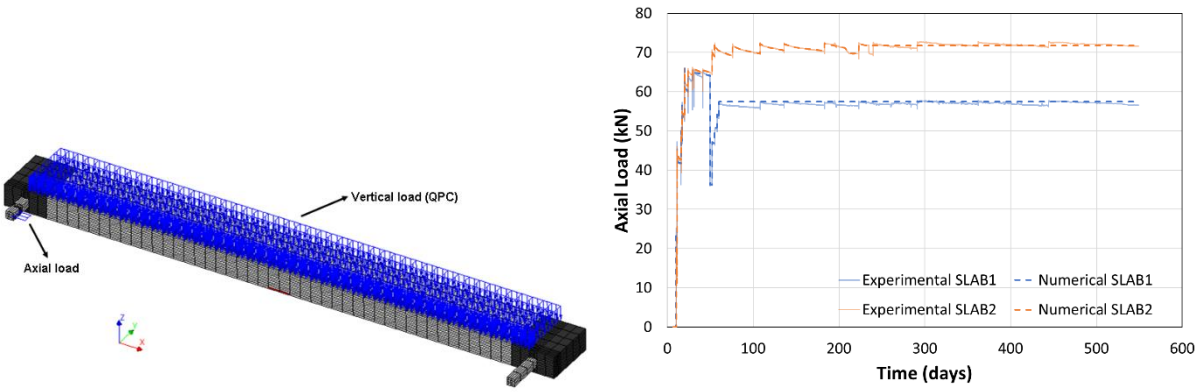

Figure 4.14 – Axial and vertical loads applied to the slab.

Table 4.2 – Time dependency of the vertical loads (self-weight SW and quasi-permanent combination QPC).

	SLAB1		SLAB2		SLAB3	
	Time (days)	Load (kN/m²)	Time (days)	Load (kN)	Time (days)	Load (kN)
SW	7.070	0	7.070	0	7.070	0
	7.168	0	7.176	0	7.098	0
	7.173	2.5	7.184	2.5	7.108	2.5
	550	2.5	550	2.5	550	2.5
QPC	7.070	0			7.070	0.0
	49.785	0			50.035	0.0
	49.790	0.74			50.085	2.96
	49.810	0.74			550	2.96
	49.815	1.48				
	49.830	1.48				
	49.835	2.22				
	49.905	2.22				
	49.910	2.96				
	550	2.96				

4.2.3 Results

In this sub-chapter, the results of the multi-physics simulation are presented and compared with experimental measurements. During the experimental campaign, a crack was observed on top surface of SLAB2 (crack 12). This crack was not expected to appear in the top surface (as the applied bending moments are positive), and it may be justified by a weakness in the top layer at that position. Since the crack do not cross the entire height of the cross section, it induces a negative curvature in that zone, affecting the remaining measurements. For that reason, the numerical analysis of SLAB2 and consequent

comparison with experimental results is restricted to 235 days. For SLAB1 and SLAB3, the analysis period is 550 days.

4.2.3.1. Dummy specimens – concrete free shrinkage

The non-uniform shrinkage field determined with the hygrometric simulation performed in sub-section 4.2.1.3 is converted to a fictitious temperature field and applied to the nodes of the mechanical FE mesh (considering that concrete's reference temperature and coefficient of thermal expansion are, respectively, $T_{c,ref} = 20°C$ and $\alpha_c = 10\mu\varepsilon/°C$). In order to access he adequacy of the calculated non-uniform shrinkage and respective fictitious temperature fields, the free shrinkage of the dummy specimens is simulated with the mechanical model described in subsection 4.2.2 (without consideration of reinforcing bars nor imposed loads).

The free shrinkage measured with the VWSG in the dummy specimens is compared with the strains calculated at the centre of the model, between to nodes spaced 14cm (measurement basis of the VWSG), as shown in Fig. 4.15. The analysis is performed with and without activation of the cracking model as to access the effect of the superficial cracking on the measured average strains.

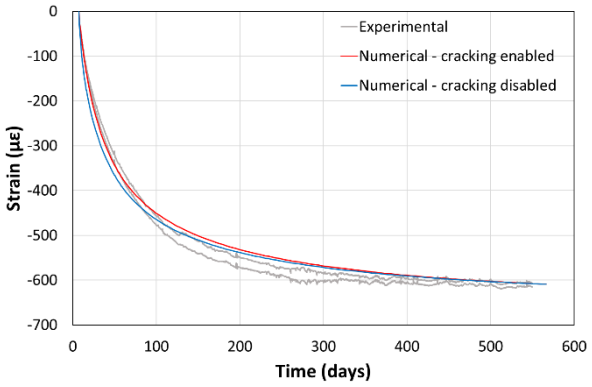

Figure 4.15 – Dummy free shrinkage: experimental and numerical results.

It can be observed that the superficial cracking has some influence on the average strains computed by the numerical model is the first days (maximum difference between analyses with and without cacking is 40με at 14 days of age). Over time, the difference of imposed shrinkage strains between different layers of the cross section diminishes (Fig. 4.16) and the influence of superficial cracking becomes negligible.

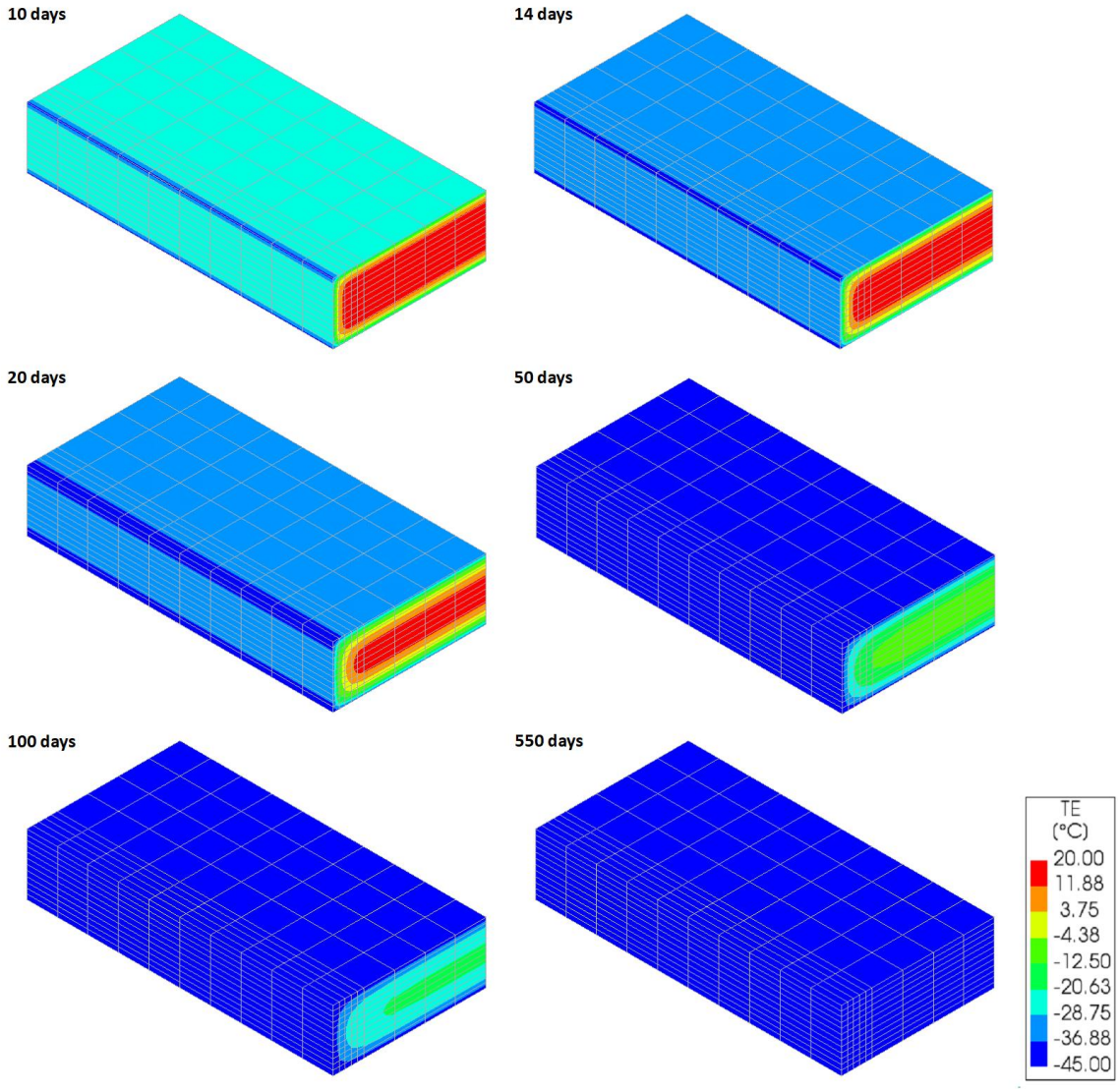

Figure 4.16 – Evolution of the imposed fictitious temperature field in the numerical analysis.

4.2.3.2 Slab specimens.

For each tested slab, the crack pattern and evolution of crack width at mid-span, the longitudinal strain in the control region and the vertical displacement at mid-span observed experimentally are compared with the results from the multi-physics simulation.

The crack pattern observed experimentally and the crack strain vectors of numerical analyses for each slab are presented in Figs. 4.17 to 4.20.

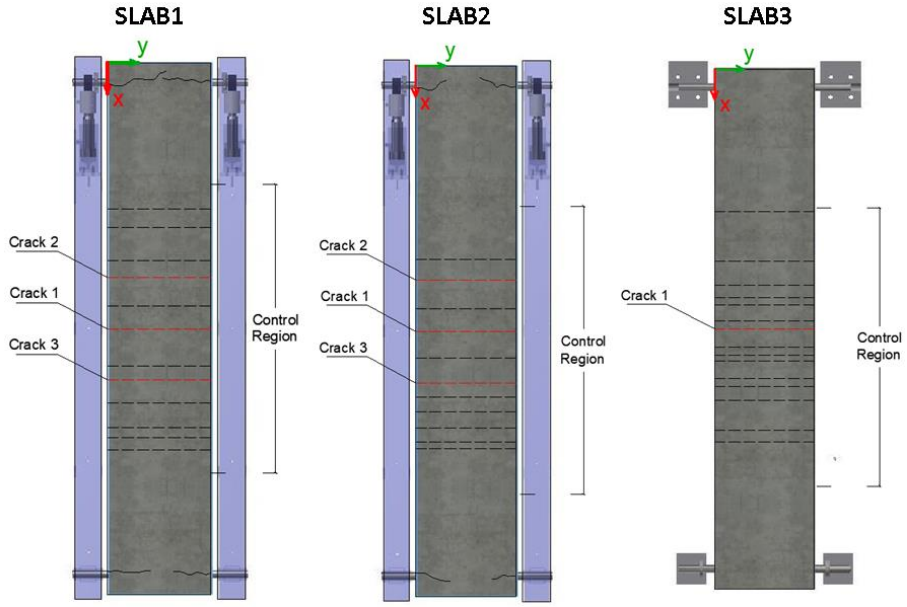

Figure 4.17 – Experimental crack pattern at the end of the analysis.

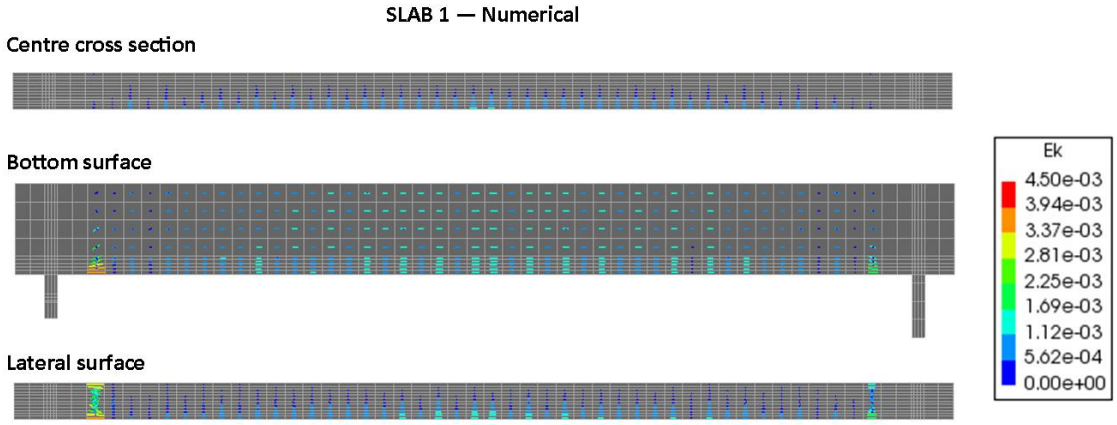

Figure 4.18 – Numerical crack pattern of SLAB1 at 550 days.

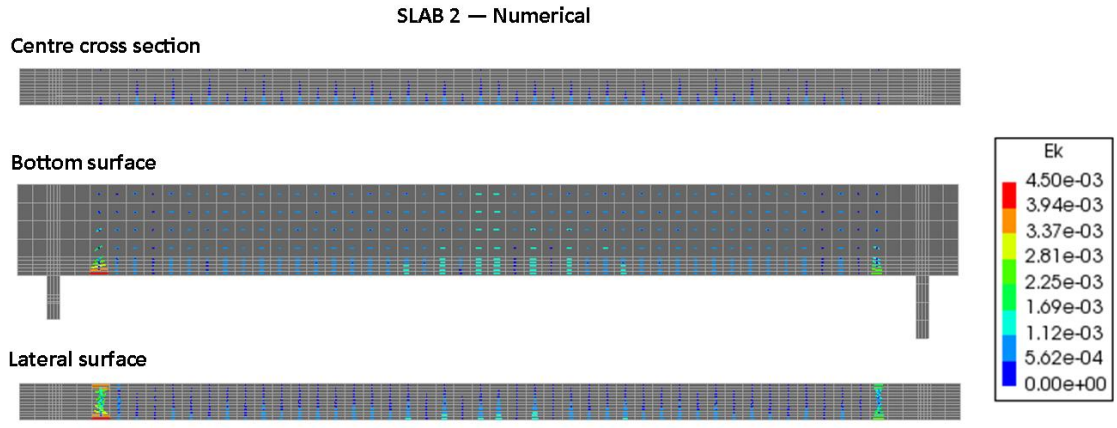

Figure 4.19 - Numerical crack pattern of SLAB2 at 235 days.

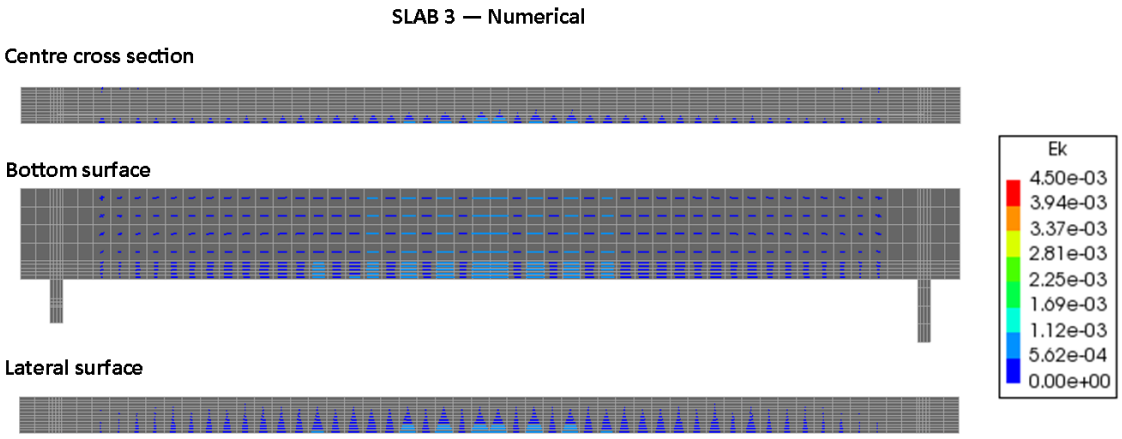

Figure 4.20 - Numerical crack pattern of SLAB3 at 550 days.

At the end of the analyses for the three slabs, crack strain are observed over the entire length of the bottom surface because of the superficial cracking caused by the self-induced stressed due to the non-uniform shrinkage field, with a concentration of higher crack strains in a central region of approximately 70cm, as a result of the flexural stresses caused by vertical loading.

For SLAB1 and SLAB2, high values of crack strains are estimated for the lateral side of the slab near the support. This effect was also observed in the experimental campaign, where large cracks (0.4 to 1.6mm) were measured over the steel rods in the lateral side of the slabs. This is motivated by localized stresses near this region caused by the application of the restraint force.

Higher values of crack width are initially estimated on the lateral side of the slabs, as shown in Fig. 4.21 in which the evolution of the crack width at mid-span is presented for each slab. This is justified with a higher contact area with the surrounding environment on the edge of the slab and consequent faster drying. This behaviour, however, was not significant enough to be perceived in the experiments. The effect of different drying rates in the centre and edge of the test specimens is overridden by the effect of in-plane bending, which is caused by a structural response of the slabs subjected to tensile stress (SLAB1 and SLAB2) that is not purely symmetrical. For the case of SLAB3, only subjected to vertical loads, the experimental crack width measured at mid-span was only observed after application of the vertical loads and is mainly induced by flexural stresses, thus being uniform over its length.

Even though the numerical analyses are not able to adequately simulate the cracking formation stage, estimations of the average crack widths at the end of the analyses are very close to the values of average crack widths measured experimentally (coincident values for SLAB1 and SLAB3 and a difference of 0.02mm for the SLAB2, which is only simulated up to 235 days of age).

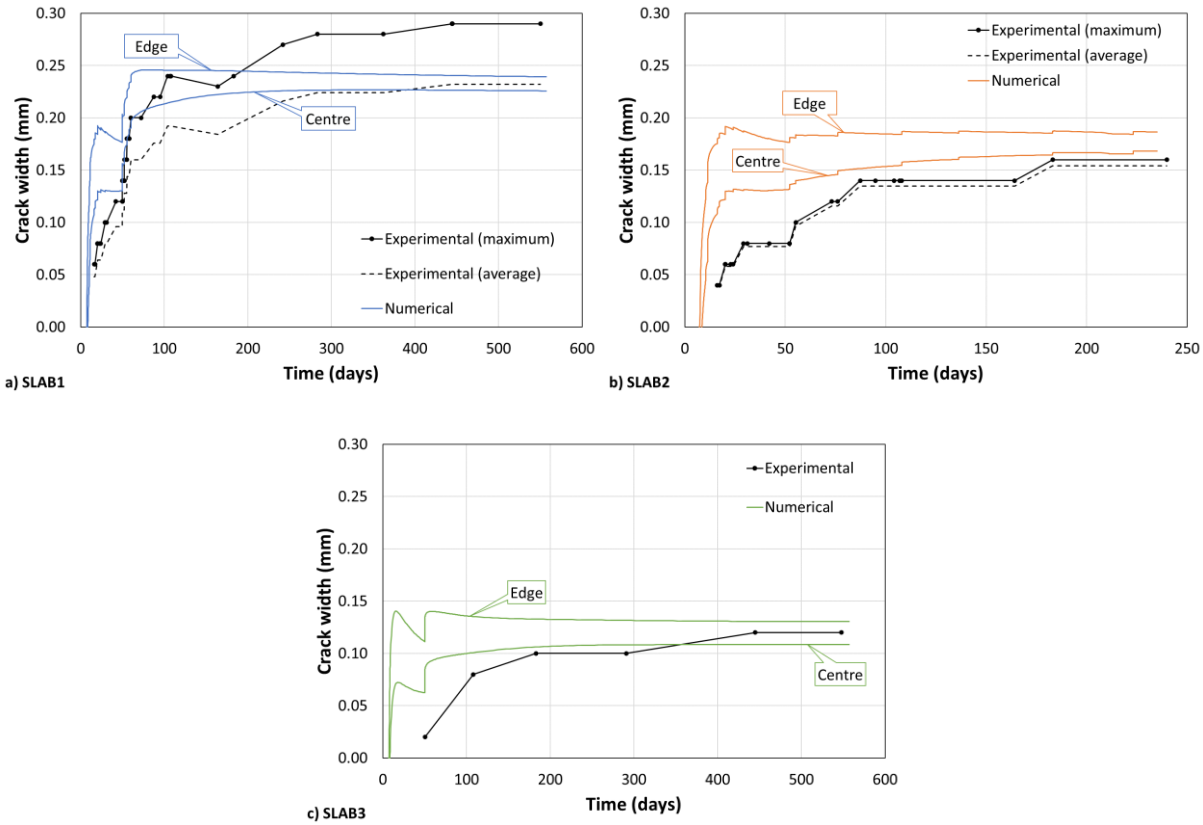

Figure 4.21 – Evolution of crack width at mid-span: a) SLAB1; b) SLAB2 and c) SLAB3.

The experimental and numerical results of strains in the control region (between position x=0.6m and x=2.0m) are presented in Fig 4.22.

The poor estimation of the crack formation stage leads to an equally poor estimation of the strains in the control region during the first days for SLAB1 and SLAB2, as the latter is significantly influenced by the former. The difference between numerical and experimental results during the first days is, however, in the same order of magnitude of the difference between the structural response observed experimentally within the first 50 days, in which both slabs are subjected to the same loading.

For SLAB3, the numerical and experimental strains on control region are almost coincident before the application of the vertical loads. During that period, there is only superficial cracking and the average axial deformation is governed by the concrete's shrinkage and internal restraint of the reinforcement. After application of the vertical loading, there is an overestimation of cracking within the control region and consequent overestimation strains.

These results might indicate some minor differences in the average tensile strength of the slabs, which in turn have a significant influence in the crack pattern and, consequently, on the global deformation of the tested slabs.

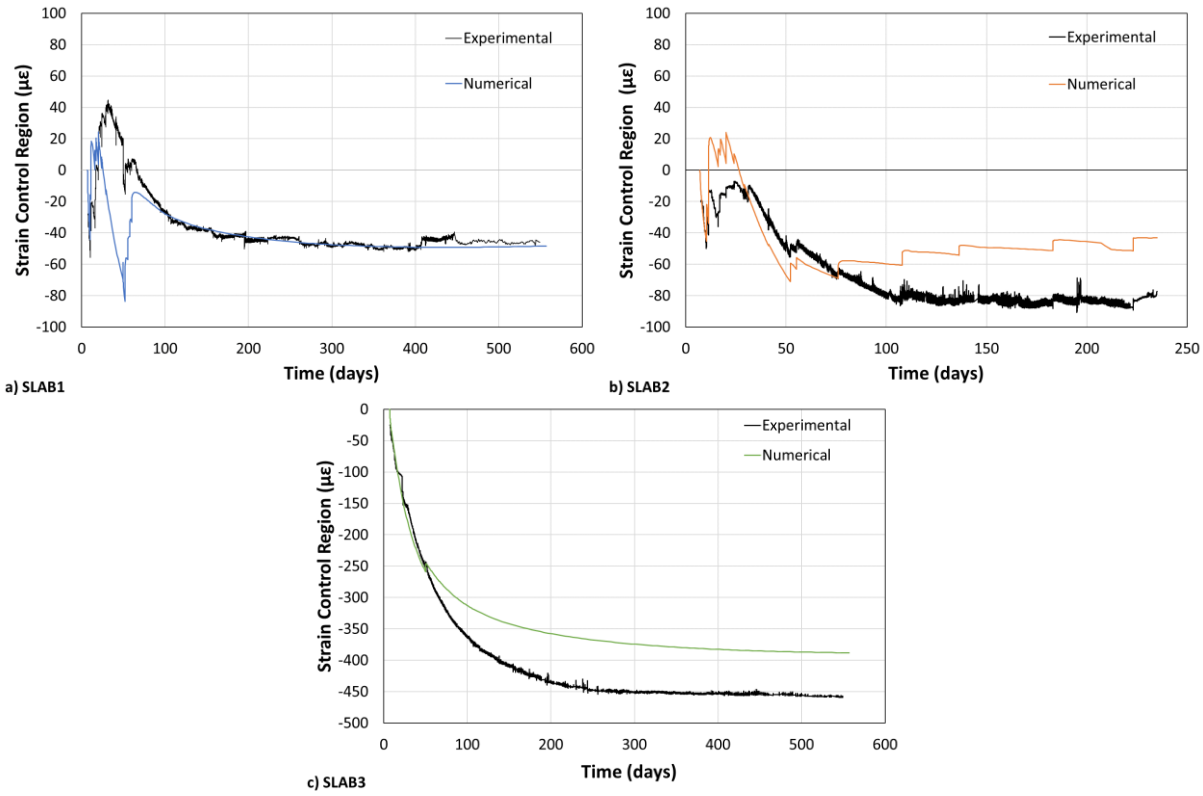

Figure 4.22 – Strains in the control region: a) SLAB1, b) SLAB2 and c) SLAB3.

The vertical displacement at mid-span and the relative displacement regarding the limits of the control region of SLAB1 are presented in Fig. 4.23.

The calculated vertical displacement at midspan does not correlate well with the experimental measurements for neither test specimen (Fig. 4.23a and Figs. 4.23c-d). This might be justified by simplifications considered in the mechanical model regarding the support region, in which only elastic deformations are considered. For SLAB1, however, the vertical displacement at the limits of the control region was measured and the deflection measured within those limits correlates well with the deflection estimated with the numerical model (Fig. 4.23b).

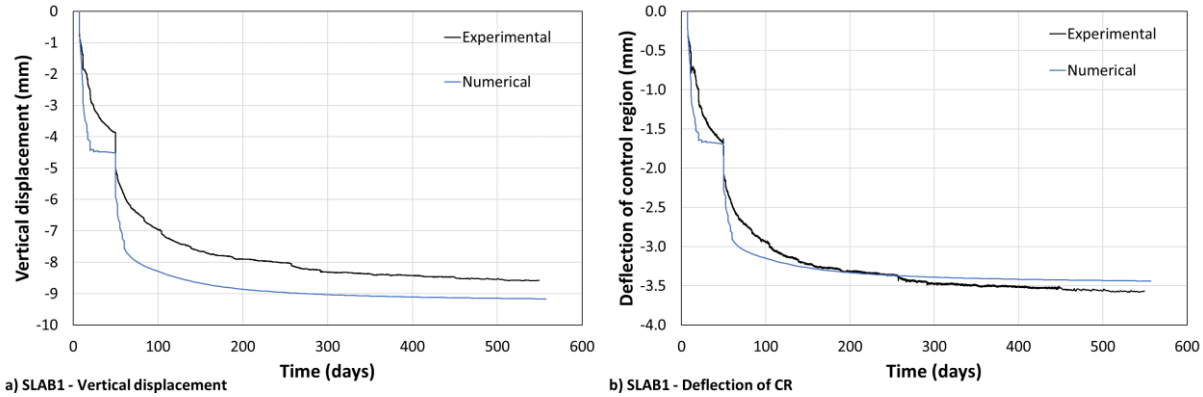

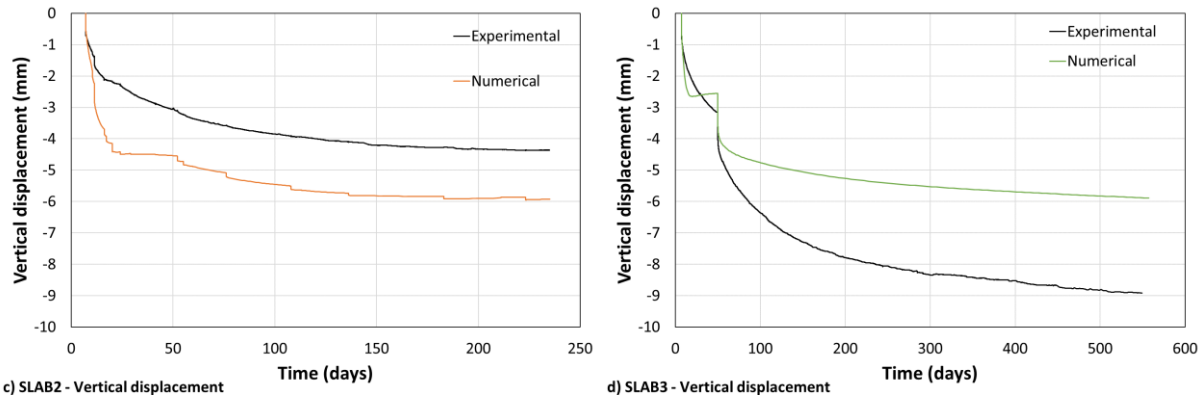

Figure 4.23 – a) Vertical displacement at mid-span of SLAB1, b) deflection within the limits of control region in SLAB1, c) vertical displacement at mid-span of SLAB2 and d) vertical displacement at mid-span of SLAB3.

4.3 Simplified analysis based on a sectional approach

The structural behaviour of SLAB1, representative of a restrained RC slab subjected to quasi-permanent combination of actions, is analysed in this sub-section with a sectional approach based on the equilibrium of forces and homogenization of RC. The assessment of the restraint force and maximum crack width is carried out by applying the available input data to the end of the experimental campaign, at 550 days, while the timely evolution of the experiment is considered in the quantification of the cracked zone. The regarded conditions at 550 days are representative for the whole service life as the evolution of shrinkage and creep strains can be considered negligible at this stage.

In the method proposed herein, the value of the restraint force applied to the RC element, for a given axial strain that is expected to occur, is determined in an iterative process with two main steps. In the first step, the RC element is divided lengthwise in several sections and the length of the cracked zones is determined based on the flexural and axial stresses caused by external loads, internal restraint of the reinforcement and a foreseeable external restraint force. The length of the cracked zones is assessed for different critical instants and the evolution of concrete's axial and flexural tensile strengths are considered. In the second step, the axial strain of each section is determined based on the internal equilibrium of forces, as described in sub-section 4.3.2, and the average strain over the RC element is compared with the expected axial strain. Steps 1 and 2 are repeated until the calculated axial strain meets the expected deformation of the RC element.

The maximum crack width is then estimated with analytical formulations based on current regulatory approach [6,10], considering the estimated restraint force for calculation of the steel stress, in a composite bending calculation.

4.3.1 Calculation principles

The calculation procedures presented herein take into account all the pertinent conditions of equilibrium and compatibility of deformations, consistently with EC2 [6] prescriptions and the analysis performed for the unidirectional behaviour in the longitudinal direction of the RC element.

For both cracked and non-cracked sections, the calculation of stresses and strains caused by shrinkage is based on the *relaxation procedure* proposed by Brasler and Selna [150], as explained in the following paragraph.

For a given time interval, if the total strain distribution is assumed to remain unchanged and the shrinkage component changes, then the instantaneous strain must also change by an equal and opposite amount. In this scenario, the stress on the cross-section varies due to relaxation and the equilibrium of the internal forces is no longer maintained. To restore equilibrium, an axial force is applied to the RC cross section. The change of strain due to shrinkage is artificially restrained with a fixation force N_f applied to the concrete's cross-section and the equilibrium is restored with an equal and opposite force $N_s = -N_f$ applied to the RC's cross-section.

For the calculation of stresses and strains caused by shrinkage, the age adjusted elastic modulus (AAEM) method, proposed by Bazant [139], is used to account for the effect of aging of concrete. The effective modulus method, introduced by Faber [151] is used for the remaining situations.

The governing equations for calculation of stresses and strains in the non-cracked and cracked sections are presented in sub-sections 4.3.1.1 and 4.3.1.2, respectively.

4.3.1.1. Non-cracked sections

The internal and external forces that are taken into account in the analyses of non-cracked sections are presented in Fig. 4.24.

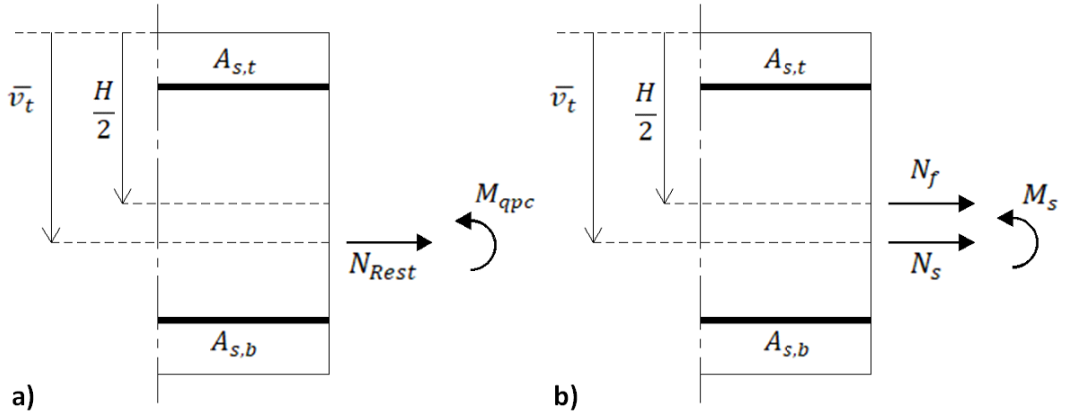

Figure 4.24 – Cross section layout with: a) forces due to vertical loads and external restraint of drying shrinkage, b) forces due to internal restraint of drying shrinkage.

The axial strain ε_G and stresses on bottom and top surface ($\sigma_{c,b}$ and $\sigma_{c,t}$, respectively) are determined by using Eq. 4.3 to Eq. 4.5.

$$\varepsilon_G = \frac{1}{E_{c,eff}(t_i,t)} \cdot \left[\frac{N_{Rest.}}{\overline{A_{eff}}} + \frac{M_{qpc}}{\overline{I_{eff}}} \cdot \left(\frac{H}{2} - \overline{v_{t,eff}}\right)\right] + \frac{1}{E_{c,adj}(t_0,t)} \cdot \left[\frac{N_s}{\overline{A_{adJ}}} + \frac{M_s}{\overline{I_{adJ}}} \cdot \left(\frac{H}{2} - \overline{v_{t,adJ}}\right)\right] \quad \text{(Eq. 4.3)}$$

$$\sigma_{c,b} = \frac{N_{Rest.}}{\overline{A_{eff}}} + \frac{M_{qpc}}{\overline{I_{eff}}} \cdot \left(H - \overline{v_{t,eff}}\right) + \frac{N_s}{\overline{A_{adJ}}} + \frac{M_s}{\overline{I_{adJ}}} \cdot \left(H - \overline{v_{t,adJ}}\right) + \frac{N_f}{A_c} \quad \text{(Eq. 4.4)}$$

$$\sigma_{c,t} = \frac{N_{Rest.}}{\overline{A_{eff}}} + \frac{M_{qpc}}{\overline{I_{eff}}} \cdot \left(-\overline{v_{t,eff}}\right) + \frac{N_s}{\overline{A_{adJ}}} + \frac{M_s}{\overline{I_{adJ}}} \cdot \left(-\overline{v_{t,adJ}}\right) + \frac{N_f}{A_c} \quad \text{(Eq. 4.5)}$$

In these equations H is the cross-section height, A_c and $\bar{A}$ are, respectively, the areas of concrete and homogenised RC sections, $\bar{I}$ is the moment of inertia of the homogenised RC section and $\overline{v_t}$ is the distance between top fibre and the centre of gravity of the homogenised RC section. The indices eff or adj indicate that calculations of the corresponding entities are performed by considering the effective elastic modulus $E_{c,eff}(t_i,t)$ or the age adjusted elastic modulus $E_{c,adj}(t_0,t)$, respectively (t is the instant of analysis, t_i is the loading age and t_0 is the age of concrete that corresponds to the beginning of drying). N_{Rest} is the restraint axial force, M_{qpc} is the flexural moment correspondent to a quasi-permanent load combination, N_f is the fixation force and N_s and M_s are the axial force and flexural moment that should be applied to the RC's centre of gravity to restore the equilibrium of internal forces after application of N_f (see Eq. 4.6 to Eq. 4.8).

$$N_f = E_{c,adj}(t_0,t) \cdot \varepsilon_{sh}(t) \cdot A_c \quad \text{(Eq. 4.6)}$$

$$N_s = -N_f \quad \text{(Eq. 4.7)}$$

$$M_s = N_f \cdot \left(\overline{v_t} - \frac{H}{2}\right) \quad \text{(Eq. 4.8)}$$

4.3.1.2. Cracked sections

For the analysis of the cracked sections, the following assumptions are considered: i) the strain distribution is linear over the depth of the section (plane section); ii) steel and concrete strains are assumed to be compatible (perfect bond between reinforcement and concrete); iii) the material behaviour is linear-elastic and iv) the tension stiffening effect is neglected and only concrete above the depth of the primary crack, both in compression and in tension, contributes to the cross-sectional properties. The

latter assumption is considered for the sake of simplification of analysis. It should be noted that for situation of short-term loading and service loading close to the cracking load, the tension stiffening effect may be significant.

The forces that are taken into account for determination of the effect of vertical loading and external restraint of drying shrinkage in cracked sections are presented in Fig. 4.25.

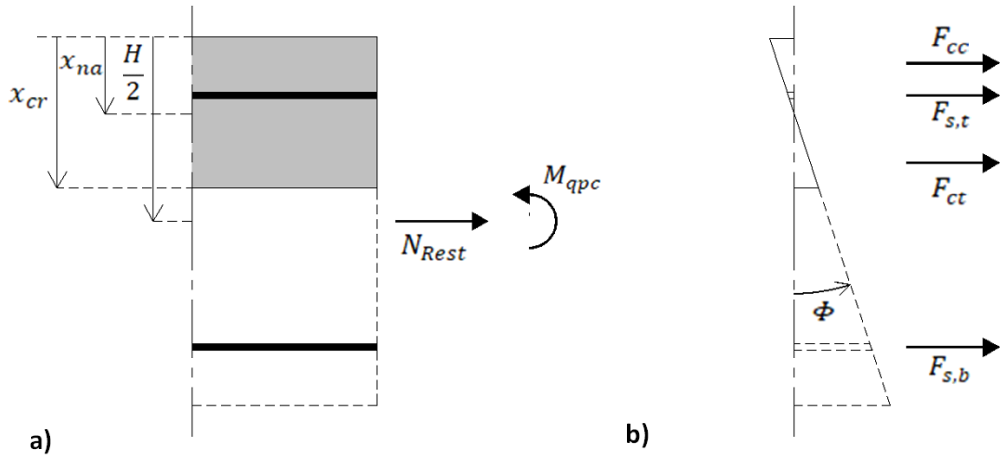

Figure 4.25 – Effect of vertical loads and external restraint of drying shrinkage: a) Cross section layout with acting forces, b) variation in the strain diagram over the cross-section and internal forces acting on concrete and reinforcement.

The neutral axis x_{na} and curvature Φ of the cross-section are calculated by complying with the following equilibrium conditions:

$$\sum F = 0: F_{s,b} + F_{s,t} + F_{cc} + F_{ct} - N_{Rest} = 0 \qquad \text{(Eq. 4.9)}$$

$$\sum M_{\frac{H}{2}} = 0: F_{s,b} \cdot \left(d_b - \frac{H}{2}\right) + F_{s,t} \cdot \left(d_t - \frac{H}{2}\right) + F_{cc} \cdot \left(\frac{x_{na}}{2} - \frac{H}{2}\right) + F_{ct} \cdot \left(x_{na} + \frac{2 \cdot (x_{cr} - x_{na})}{3} - \frac{H}{2}\right) - M_{qpc} = 0 \qquad \text{(Eq. 4.10)}$$

where $F_{s,b}$, $F_{s,t}$, F_{cc} and F_{ct} are internal forces acting on reinforcement and concrete and determined with Eq. 4.11 to Eq. 4.14:

$$F_{s,b} = A_{s,b} \cdot E_s \cdot \Phi \cdot (d_b - x_{na}) \qquad \text{(Eq. 4.11)}$$

$$F_{s,t} = A_{s,t} \cdot E_s \cdot \Phi \cdot (d_t - x_{na}) \qquad \text{(Eq. 4.12)}$$

$$F_{cc} = B \cdot \frac{x_{na}}{2} \cdot E_{c,eff} \cdot \Phi \cdot (-x_{na}) \qquad \text{(Eq. 4.13)}$$

$$F_{ct} = B \cdot \frac{(x_{cr} - x_{na})}{2} \cdot E_{c,eff} \cdot \Phi \cdot (x_{cr} - x_{na}) \qquad \text{(Eq. 4.14)}$$

The forces that are taken into account for determination of the effect of internal restraint of drying shrinkage in cracked sections are presented in Fig. 4.26.

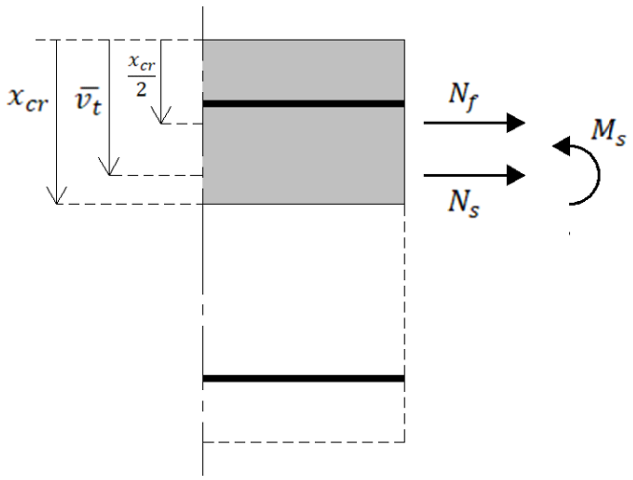

Figure 4.26 – Effect of internal restraint of drying shrinkage: cross section layout with acting forces.

The strain variation caused by drying shrinkage $\Delta\varepsilon_{G,sh}$ is determined by using Eq. 4.15.

$$\Delta\varepsilon_{G,sh} = \frac{1}{E_{c,adj}(t_0,t)} \cdot \left[\frac{N_s}{\overline{A_{adj}}} + \frac{M_s}{\overline{I_{adj}}} \cdot \left(\frac{H}{2} - \bar{v}_t\right)\right] \quad \text{(Eq. 4.15)}$$

For the analysis of cracked sections, drying shrinkage is imposed over the depth of non-cracked concrete x_{cr} and the parameters considered in Eq. 4.15 are determined with Eq. 4.16 to Eq. 4.23:

$$N_f = E_{adj}(t_0,t) \cdot \varepsilon_{sh}(t) \cdot A_c \quad \text{(Eq. 4.16)}$$

$$N_s = -N_f \quad \text{(Eq. 4.17)}$$

$$M_s = N_f \cdot \left(\bar{v}_t - \frac{x_{cr}}{2}\right) \quad \text{(Eq. 4.18)}$$

$$A_c = B \cdot x_{cr} \quad \text{(Eq. 4.19)}$$

$$\overline{A_{adj}} = B \cdot x_{cr} + A_{s,t} \cdot \left(k_{h,adj} - 1\right) + A_{s,b} \cdot k_{h,adj} \quad \text{(Eq. 4.20)}$$

$$\bar{v}_t = \frac{1}{\overline{A_{adj}}} \cdot \left[\frac{B \cdot {x_{cr}}^2}{2} + A_{s,t} \cdot d_t \cdot \left(k_{h,adj} - 1\right) + A_{s,b} \cdot d_b \cdot k_{h,adj}\right] \quad \text{(Eq. 4.21)}$$

$$\overline{I_{adj}} = \frac{B \cdot {x_{cr}}^3}{12} + B \cdot x_{cr} \cdot \left(\bar{v}_t - \frac{x_{cr}}{2}\right)^2 + A_{s,t} \cdot \left(k_{h,adj} - 1\right) \cdot (d_t - \bar{v}_t)^2 + A_{s,b} \cdot k_{h,adj} \cdot (d_b - \bar{v}_t)^2 \quad \text{(Eq. 4.22)}$$

$$k_{h,adj} = \frac{E_s}{E_{c,adj}(t_0,t)} \quad \text{(Eq. 4.23)}$$

where B is the width of the cross section, $k_{h,adj}$ is the coefficient of homogenisation and d_t and d_b are, respectively, the distance between top surface of the cross-section and top and bottom reinforcement. The axial strain in the cracked section is determined by adding the effects of the restraint force N_{Rest} and flexural moment caused by vertical loads M_{qpc} to the strain variation $\Delta\varepsilon_{G,sh}$ caused by shrinkage, according to Eq. 4.24.

$$\varepsilon_G = \Phi \cdot \left(\frac{H}{2} - x_{na}\right) + \Delta\varepsilon_{G,sh} \qquad \text{(Eq. 4.24)}$$

4.3.2 Determination of restraint force

The proposed simplified method is applied for determination of the restraint force applied to SLAB1 and SLAB2, taking into account the axial strain measured in the control region. The analysis is limited to the length of the control region, which is divided into 56 sections of 2.5cm width, as shown in Fig. 4.27.

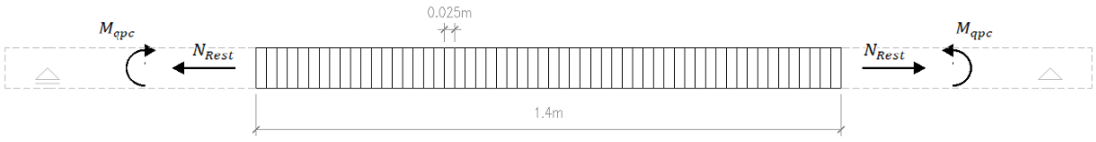

Figure 4.27 – Schematic representation of slab's control region divided into sections.

For the first step of SLAB1 analysis, the cracking length within the control region is assessed for three critical instants: (i) at 28 days of age, when the maximum restraint force is at maximum value; (ii) at 60 days of age, after application of additional vertical loads and final value of the restraint force; (ii) at the end of analysis, at 550 days of age. Regarding SLAB2, two critical instants are assessed: (i) 60 days, when the maximum restraint load is applied; (ii) at 235 days, immediately before the occurrence of superficial crack on the top fibres of the slab.

In order to take into account for the tensile softening behaviour of concrete and its effect on the redistribution of stresses in flexural cracking, a compromise between considering the flexural tensile strength or the uniaxial tensile strength of concrete is found, depending on the loading that the slab is subjected to. The value of the weighted tensile strength $f_{ct,w}$ at each section is therefore calculated with Eq. 4.25:

$$f_{ct,w=}k_M \cdot \left(f_{ctm,fl} - f_{ctm}\right) + f_{ctm} \qquad \text{(Eq. 4.25)}$$

where k_M is a coefficient that takes into account the weight of flexural moment in the maximum tensile stress and $f_{ctm,fl}$ is the flexural tensile strength calculated according to EC2 formulation [6]. For the

analysis of SLAB1 and SLAB2, which are merely subjected to positive bending moments, the value of k_M is calculated as follows:

$$k_M = \frac{1}{\sigma_{c,b}} \cdot \left[\frac{M_{qpc}}{\overline{I_{c,eff}}} \cdot \left(H - \overline{v_{t,eff}} \right) + \frac{M_S}{\overline{I_{c,adJ}}} \cdot \left(H - \overline{v_{t,adJ}} \right) \right] \quad \text{(Eq. 4.26)}$$

The axial force and vertical loads were applied between 7 and 60 days. For calculation of the effective modulus of elasticity, a loading age of 28 days is considered. For calculation of the adjusted modulus of elasticity, the aging coefficient χ is calculated according to the simplified formulation proposed by Chiorino and Lacidogna [152,153]:

$$\chi = \frac{t_0^{0.5}}{1 + t_0^{0.5}} = 0.72 \quad \text{(Eq. 4.27)}$$

Table 4.3 shows the calculated crack length $L_{cracked}$ for each instant considering, as the first iteration, the restraint force N_{Rest} applied in the experimental campaign.

Table 4.3 – Calculated crack length for the first iteration.

	Age (days)	p **(kN/m²)**	N_{Rest} **(kN)**	ε_{sh} **(με)**	$E_{c,eff}(28,t)$ **(GPA)**	$E_{c,adj}(7,t)$ **(GPa)**	f_{ctm} **(MPa)**	$f_{ctm,fl}$ **(MPa)**	$L_{cracked}$ **(m)**
SLAB1	28	2.50	65	225	28.9	12.9	2.5	3.8	*
	60	5.46	57	370	12.5	11.4	2.6	3.9	0.85
	550	5.46	57	610	8.5	8.5	2.8	4.2	0.85
SLAB2	60	2.50	72	370	12.5	11.4	2.6	3.9	*
	235	2.50	72	575	9.6	9.5	2.7	4.1	*

*Cracking occurs if cross section height is reduced to account for the notch at midspan.

At the final iteration, the axial strain in the control region is $\varepsilon_G(550) = -37\mu\varepsilon$ for SLAB1 and $\varepsilon_G(235) = -92\mu\varepsilon$ for SLAB2, as resumed in Table 4.4. The differences between experimental and calculated axial strains are within reasonable limits of +/-12με, therefore, no further discretization of the control region was pursued.

Table 4.4 – Main results of analysis of SLAB1.

		p **(kN/m²)**	N_{Rest} **(kN)**	$L_{cracked}$ **(m)**	ε_G **(με)**	$\varepsilon_{G,exp}$ **(με)**
SLAB1	First iteration	5.46	57	0.85	130	-45
	Final iteration	5.46	53	0.65	-37	
SLAB2	First iteration	2.5	72	-	-	-80
	Final iteration	2.5	83	0.35	-92	

For SLAB1, the restraint force estimated in the final iteration represents 39% to 42% of concrete's cracking force N_{cr} (considering a uniaxial tensile strength ranging between 2.5MPa and 2.7Mpa), whereas the experimental restraint force applied to SLAB1 represents 42% to 45% of N_{cr}. Regarding SLAB2, the

restraint force estimated in the final iteration represents 61% to 66% of concrete's cracking force N_{cr}, whereas the experimental restraint force applied to SLAB2 represents 53% to 58% of N_{cr}

The results show that the method proposed in this sub-section can yield an approximate value of the restraint force at long-term, for a given axial deformation, close to the real restraint force applied to the slab. The reverse calculation is not recommended though, as the value of axial strain is significantly sensitive to the calculated cracked length.

4.3.3 Determination of crack width based on regulatory approach

The formulations proposed by EC2 and MC10 for estimation of crack width in RC elements subjected o composed bending are tested and the results are presented in Table 4.5.

Table 4.5 – Crack width at end of analysis: experimental and calculated results.

					Eurocode 2			**Model Code 10**		
	w_{exp} (mm)	p (kN/m²)	N_{Rest} (kN)	$(\varepsilon_{sm}-\varepsilon_{cm})$	$s_{r,max}$ (m)	w_d (mm)	$w_{d,notch}$ (mm)	$2L_{s,max}$ (m)	w_d (mm)	$w_{d,notch}$ (mm)
SLAB1	**0.18-0.29**	5.46	57	0.00084	0.15	0.12	**0.16**	0.16	0.23	**0.30**
	(Average: 0.23)	5.46	53	0.00079	0.15	0.12	**0.15**	0.16	0.22	**0.29**
SLAB2	**0.16-0.18**	2.50	72	0.00065	0.16	0.10	**0.13**	0.18	0.22	**0.28**
	(Average: 0.17)	2.50	83	0.00078	0.16	0.12	**0.15**	0.18	0.24	**0.30**
SLAB3	**0.12**	5.46	0	0.00013	0.13	0.04	**0.05**	0.14	0.10	**0.15**

The results show that differences between calculated and experimental restraint forces did not significantly influence the value of the estimated crack width.

The EC2 formulation provided estimations that significantly underestimate the crack width measured experimentally. On the other hand, MC10 formulation provided a conservative estimations of crack width at notch level, especially for the least solicited slabs (SLAB2 and SLAB3). Differences between EC2 and MC10 derive merely from the fact that EC2 approach, unlike MC10, does not account for the time dependent increase of crack width due to shrinkage. In fact, estimation of the maximum crack spacing $s_{r,max}$ according to EC2 is coherent with estimation of the maximum transfer length $L_{s,max}$ according to MC10. These values do not comply, however, with the crack spacing and transfer length observed experimentally (with measurement of the distance between cracks and strains over the length of rebar with the fibre Bragg Grating sensors, respectively).

Even though the MC10 approach for calculation of crack width provided results that are on the safe side, the calculated transfer length is smaller than experimental observations. This means that an expected

underestimation of crack width due to consideration of a lower value of transfer length is possibly being compensated with an overestimation caused by the following phenomena: (i) overestimation of the effect of concrete shrinkage on the crack width; (ii) underestimation of the tension stiffening effect, weather by underestimating the bond coefficient β (taken equal to 0.4 for long term loading and stabilized cracking stage) or the effective area of concrete $A_{c,eff}$ for assessment of the average strain over the transfer length; and (iii) overestimation of the difference between the crack width at reinforcement w_d and at notch level $w_{d,notch}$. The additional crack width at the notch level was derived from the linear strain profile over the height of the section, with the extrapolation of $(H - x_{na})/(d_b - x_{na})$, as proposed by MC10. However, the assumption of a linear strain profile represents an oversimplification for concrete in the cracked cross-section because of the local effect caused by load transfer between reinforcement and concrete by bond.

Chapter 5

Case study: design of a fully restrained RC slab

5.1 Introduction

In this Chapter, a thermo-hygro-mechanical simulation (THMS) based on the multi-physics approach addressed in sub-section 2.3 is employed to study the structural behaviour of a fully restrained solid one-way RC slab subjected to vertical loading.

Firstly, the THMS is compared with two further strategies of analysis, based on the same FE mesh, to better discuss the behavioural differences that can be grasped through the THMS. The two strategies are: (i) a simplified thermo-mechanical simulation (TMS), in which the temperature field due to hydration heat is explicitly considered, but shrinkage is modelled in a simplified manner, by merely imposing a uniformly distributed shrinkage strain throughout the entire slab thickness (yet having variation during the time of analysis); and (ii) a mechanical simulation (MS), without computation of neither temperature nor moisture fields, in which the thermal effects are fully neglected and shrinkage strains are considered in the same manner as in the TMS model. The modelling strategies for simulation of cracking and creep, presented in Chapter 2 and validated in Chapter 4, are employed in all simulations.

The THMS is then employed considering five different scenarios of longitudinal reinforcement, regarding different hypothetically possible design approaches using the Model Code 2010 formulation for estimation of crack width, for comparison of the service life behaviour.

5.2 Overall description of the case study

The criteria defined for the selection of the structure took into consideration the most significant aspects of this study, as well as some simplifications: (i) the structure should consist of an axially restrained slab, also subjected to vertical loads; (ii) the span, material classes and structural system should be typical of small buildings; (iii) no splicing of reinforcement is considered and the geometry should be simple enough to allow advanced simulations without loss of representativeness.

Based on the abovementioned requirements, the slab schematized in Fig. 5.1 was selected as the case study. The slab reproduces an ordinary construction in Europe, with a normal strength concrete class grade (C30/37) and subjected to end restraint.

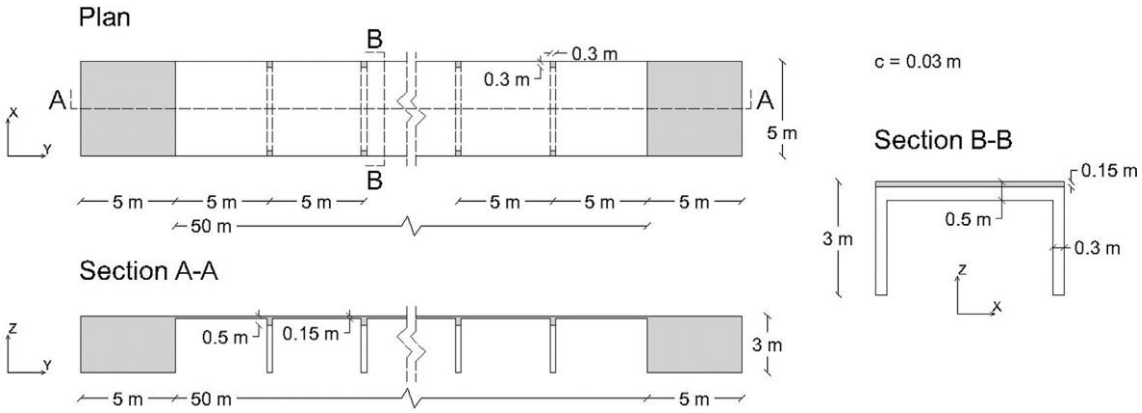

Figure 5.1 – Floor plan and cut designs of the studied slab.

Reinforcement steel was considered to be of class S500C. The slab is 0.15m thick and 5.0m wide, it develops along 50.0m, being supported at every 5.0m by transverse beams with a 0.30 × 0.50m2 cross-section. These beams are supported by columns with a 0.30 × 0.30m² cross-section, fixed at the bottom. The slab extremities (separated by 50 m) are connected to massive and extremely stiff concrete blocks, which completely restrain the longitudinal deformation. A concrete cover of 0.03m was considered for all structural elements.

All analyses start at the concrete setting time and extend along 50 years, as to infer the structural service life behaviour during the expected lifespan. In order to simplify the analyses, the thermal effects of the daily and seasonal temperature variations are disregarded and the slab is submitted to an "ideal" environment with constant temperature and relative humidity (T = 20 °C and RH = 60%).

Imposed loads for category A floors (areas for domestic and residential activities) were considered, according to Eurocode 1 [129]. Besides the self-weight, the slab is submitted to a distributed permanent load of 2.0 kN/m² and a live load of 2.0 kN/m² ($\psi_2 = 0.3$). The slab is wet cured during the first 7 days, age at which propping and formwork are removed; therefore, self-weight of the slab (3.75 kN/m² in general) is activated at this age in the simulation model. Live and additional permanent loads are applied at the age of 28 days, corresponding to a quasi-permanent load combination (2.6 kN/m²) according to Eurocode 1 [129]. Both the self-weight at the age of 7 days and the quasi-permanent load at 28 days are applied progressively, along 3h and 12h, respectively, to avoid instantaneous load effects.

The upcoming paragraphs pertain to the disclosure of the reinforcement considered for comparison between THMS, TMS and MS, and to the criteria used to adopt such reinforcement. This can be of importance upon interpretation of the simulation results. The reinforcement of the slab was designed according to standard recommendations for ultimate (ULS) and service (SLS) limit states [6,129,140], in complete disregard to the effects of restrained shrinkage (which is allowed by EC2 [6] in cases where

joints are incorporated at every 30 m), in order to understand the implications of such approach. A numerical linear analysis was performed to calculate the bending moments acting on the slab in the longitudinal direction over the columns and on the centre of the slab. For the design of the flexural reinforcement of the slab, the negative bending moments at the ULS were reduced by using a coefficient of redistribution of 0.8. Since the bending moments are higher near the free edges, it was decided to longitudinally reinforce the slab with ϕ10mm S500 steel rebars on both top and bottom layers, transversally spaced by 0.10m in the 1.0m vicinity of the columns (zone Z1), and transversally spaced by 0.15m in the remainder parts (zone Z2) – see Fig. 5.2. Top and bottom transverse reinforcement of the slab consisted in ϕ8mm rebars spaced by 0.25m (not represented in Fig. 5.2). In order to simplify the design and procedures of analysis, the alternation of live loads in different spans was neglected, and the slab has the same reinforcement in both the top and bottom surfaces, with a continuous layout.

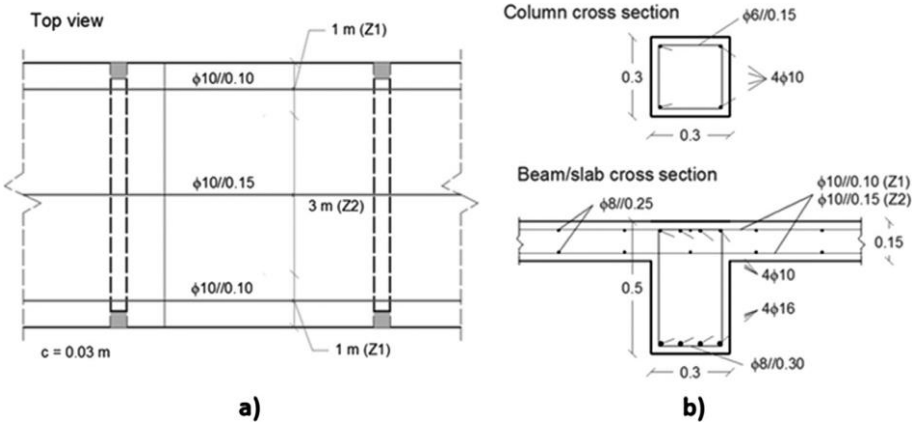

Figure 5.2 – a) Distribution of the longitudinal reinforcement on the slab; b) beam's and column's reinforcement.

A quasi-permanent combination of actions was considered in order to verify that the longitudinal reinforcement, designed for the ULS, meets the crack width requirement in the SLS ($w_d \leq 0.3\ mm$) for an exposure class XC3 [6]. Table 5.1 shows the bending moments at support and mid-span of the slab for zones Z1 and Z2, determined with a linear analysis, as well as the stress in the reinforcement and the crack width at the reinforcement level, calculated analytically according to MC10 and EC2 approaches, disregarding the axial stress due to the external restraint of shrinkage. Crack width values calculated with MC10 were considerably higher in comparison to the EC2 predictions because the former approach considers the effect of concrete shrinkage, ε_{sh} in the calculation of the relative strain between steel and concrete. ε_{sh} is herein taken as 530 με, which is the value experimentally determined for the same material and environmental conditions of the present case study [141]. For both approaches, the calculated crack width, assuming an axial restraint force equal to zero ($N_{Rest} = 0$), was below the maximum allowable value of 0.3 mm.

Table 5.1 – Verification of crack width requirements for the SLS ($N_{Rest} = 0$)

	Support Z1	**Mid-span Z1**	**Support Z2**	**Mid-span Z2**
M_{cqp} (kN.m)	19.2	8.4	9.1	6.6
σ_s (MPa)	248	108	173	125
$w_{d,EC2}$ (mm)	0.15	0.03	0.07	0.02
$w_{d,MC10}$ (mm)	0.25	0.12	0.21	0.15

5.3 3D thermo-hygro-mechanical simulation

5.3.1 Material properties

The slab's concrete corresponds to a C30/37 strength grade class, with w/c = 0.51, and it is considered to be the same as the one adopted in Azenha, *et al.* [141], where experimental tests were performed to determine the material parameters used in humidity diffusion and other mechanical properties. Table 5.2 shows the main properties of the materials considered in the analyses.

Table 5.2 – Material properties.

Mechanical properties		Thermal properties		Hygrometric properties	
Concrete: 280 kg/m³ of cement CEM I 42.5R					
Density ρ	2500 kg/m³	Specific heat c	960 J/(kg. °C)	D_0	2.98×10⁻¹¹ m²/s
Poisson's ratio ν	0.2	Thermal conductivity k	2.6 W.m/°C	D_1	3.08×10⁻¹⁰ m²/s
Young modulus E_{cm}	33 GPa	Coef. thermal expansion α_c	10 με/°C	H_c	0.8
Compressive strength f_{cm}	38 GPa	Rate constant A_T	2.645×10⁷	n	2
Tensile strength f_{ctm}	2.9 MPa	Ideal gas constant R	8.314 J/(mol °C)	$\varepsilon_{sh,ult}$	625 με
Fracture Energy G_F	76 N.m	Apparent activation energy E_a	38.38×10³ J/mol	$\varepsilon_{sh,60\%}$	530 με
Steel: S500					
Yield stress f_{sym}	538 GPa	Coef. thermal expansion α_s	12 με/°C		
Young modulus E_{sm}	200 GPa				

Average mechanical properties for a concrete class C30/37 and reinforcing steel S500 were assumed in accordance to design codes [6,10] and typical values were adopted for the thermal dilatation coeficients of concrete (with granite aggregates) and steel.

The values of n and H_c were determined based on the results reported by Kim and Lee [147], whereas parameters D_1 an D_2 were assessed by best-fitting experimental humidity curves obtained on concrete specimens [110,141].

Both thermal conductivity and specific heat of concrete were estimated on basis of a weighted average of the corresponding thermal properties of the constituents of the mix (composed by granite type

aggregates). The heat generation potential was determined based on a previous testing of the cement in an isothermal calorimeter - see Azenha [110].

The evolution of the concrete tensile strength and modulus of elasticity over time is simulated using the EC2 formulations (Eq. 5.1 and Eq. 5.2, respectively) for a C30/37 class R cement ($s = 0.2$, $\alpha = 1$ when $t < 28$ days and $\alpha = 2/3$ when $t \geq 28$ days). Since the EC2 model does not adequately predict the evolution of the modulus of elasticity at very early ages, especially right after setting, the mathematical model represented in Eq. 5.3 [46] was used for such purpose, yet being able to fulfil the development of E-modulus after 7 days of age, according to EC2. Parameters τ_1 and β_1, which define the first inflection point of the curve, were determined to fit experimental results derived from classical cyclic compression tests performed in 3 research centres for a C30/ 37 (class R cement) concrete at very early ages [142,154,155].

$$f_{ctm}(t) = f_{ctm}(28) \cdot \left[e^{s\left(1-\sqrt{\frac{28}{t}}\right)} \right]^{\alpha} \qquad \text{(Eq. 5.1)}$$

$$E_{cm}(t) = E_{cm}(28) \cdot \left[e^{s\left(1-\sqrt{\frac{28}{t}}\right)} \right]^{0.3} \qquad \text{(Eq. 5.2)}$$

$$E_{cm}(t) = \alpha_1 \cdot e^{-\left(\frac{\tau_1}{t}\right)^{\beta_1}} + \alpha_2 \cdot e^{-\left(\frac{\tau_2}{t}\right)^{\beta_2}} \qquad \text{(Eq. 5.3)}$$

Based on the model used to characterize the evolution of the modulus of elasticity (exceptionally in Eq. 5.3, the time is measured from the instant of contact of water with the dry components of the mixture), the setting time of concrete was calculated following the procedure proposed and validated by Granja [154]. This procedure consists in determining the first derivative of the E-modulus evolution, being the setting time the instant at which dE/dt reaches 50% of its maximum value – see Fig. 5.3. It is noted that for implementation in the numerical models (either THMS, TMS or MS) the time axis of Fig. 5.3 was shifted in such a manner that the setting time corresponds to “0”, to be consistent with the strategy adopted in the modelling.

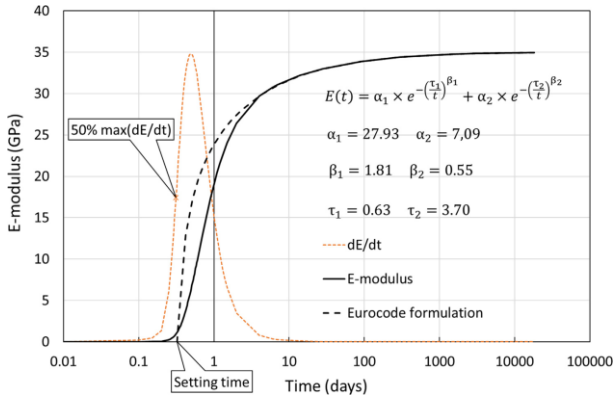

Figure 5.3 – Elastic modulus evolution and setting time of concrete.

A similar strategy was adopted to characterize the viscoelastic behaviour of the concrete, where the EC2 formulation (known to perform well at long term) is combined with the Double Power Law (DPL) [120,156], which shows good agreement with experimental data at early ages [157]. Concrete creep was determined according to the EC2 formulation for loading ages ranging from 7 days to 50 years, whereas the creep functions for loading ages between 0.01 and 7 days were determined with the DPL, expressed as follows:

$$J(t,t_0) = \frac{1}{E_0(t_0)} + \frac{\varphi_1}{E_0(t_0)} \cdot (t_0^{-m} + \alpha) \cdot (t - t_0)^n \qquad \text{(Eq. 5.4)}$$

where $J(t,t_0)$ is the creep compliance function at time t for a load applied at instant t_0, $E_0\ (t,t_0)$ is the asymptotic elastic modulus and φ_1, m, n and α are material parameters, calibrated based on the creep functions determined according to EC2 for loading ages of 7 to 50 years (with the values of 1.81, 0.19, 0.13 and 0.10, respectively). These creep functions were used to adjust the parameters of the Kelvin chain adopted in the mechanical simulation of the slab, according to the approach described in sub-section 2.3.3.1. Fig. 5.4 shows the modulus of elasticity of each Kelvin unit per loading age, considering a chain with 9 units with retardation times $\tau_u = 0.001 \times 10^{\mu-1}$.

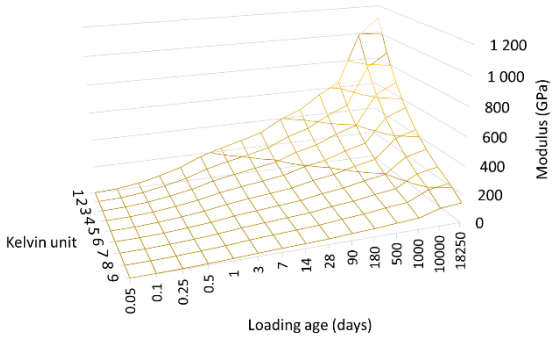

Figure 5.4 – Three-dimensional graph depicting the modulus of elasticity of each Kelvin unit as a function of loading age.

5.3.2 F.E. models

5.3.2.1 Thermo-hygrometric modelling

Since the temperature and humidity flows are unidirectional along the slab thickness, the prism represented in Fig. 5.5, with a height equal to the slab's thickness (0.15 m), was modelled considering symmetry planes (across which no flux is allowed) in the four longitudinal faces. No thermal nor drying shrinkage strains were considered in the concrete beam section bellow the slab. This simplifying assumption does not affect the main results of the analysis (crack widths and restraint forces) because the highest crack strains occur in the direction perpendicular to the girder axis (the restrained direction) and the highest crack widths are observed out of the girder.

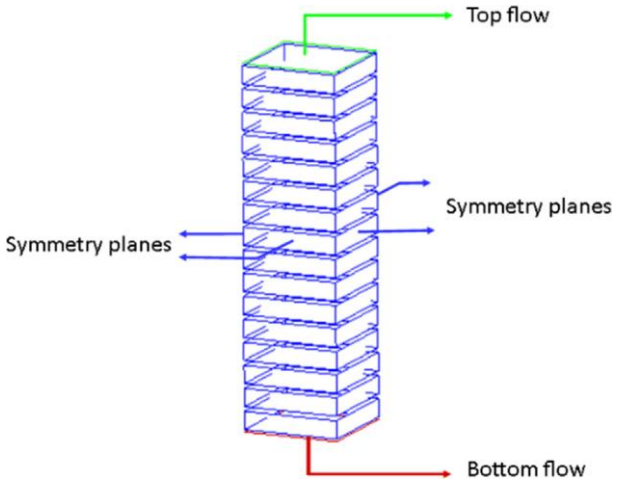

Figure 5.5 – FE mesh and boundaries of thermos-hygrometric model.

Moisture and thermal boundary conditions were applied to the top and bottom surfaces of the prism with due attention to two distinct situations: before and after formwork removal. During the first 7 days, before formwork removal, the slab is considered completely sealed ($h_m = 0\ m.s^{-1}$) on both the top and bottom surfaces (in correspondence to the existence of a formwork on the bottom surface and adequate curing measures in the top surface). During the same first 7 days, the following thermal boundaries apply: for the top surface the convection radiation coefficient is taken as $h_{cr} = 10\ W.m^{-2}.°C^{-1}$, duly calibrated by Azenha *et al.* [158] for similar environmental conditions ($T_{env} = 20$ °C); for the bottom surface, covered with a 18mm thick plywood formwork ($K_{plywood} = 0.15\ W.m.°C^{-1}$), the electrical analogy detailed by Azenha [110] and Jonasson [115] was used to calculate the convection-radiation coefficient, which takes the value $h_{cr,formwork} = 5\ W.m^2.°C^{-1}$. After removing the formwork, the same thermal boundary conditions were admitted for both the top and bottom surfaces ($h_{cr} = 10\ W.m^2.°C^{-1}$). The direct contact of both surfaces with the surrounding environment leads to the

adoption of a moisture emissivity coefficient of $h_m = 4.81 \times 10^{-8}\ m.s^{-1}$, experimentally determined by Azenha *et al.* [141] . The T and RH of the environment were considered constant throughout the analysis ($T_{env} = 20$ °C and $H_{env} = 60$ %, respectively). Initial temperature and humidity in the concrete are $T = 20\ °C$ and $H = 100$ %, respectively.

The nodes along the height of the prism for thermo-hygrometric simulation are coincident with the ones along the slab thickness in the mechanical simulation. Thus, the temperatures from the thermo-hygrometric model can be applied to the mechanical model in coincident points of the slab FE mesh. The mesh defined for the prism in the thermo-hygrometric model is composed by 16 eight-nodded solid FE along its height. This refinement is adequate for the intended accuracy of results and allows the slab in the mechanical model to be divided into 8 layers of twenty-nodded solid FE (quadratic integration) along its thickness.

Based on the evolution and gradients of humidity, the drying shrinkage along the thickness of the slab was computed and discretized into 8 depths, to be imposed to the corresponding slab layers in the mechanical model.

5.3.2.2 Mechanical modelling:

The FE mesh adopted for the mechanical model, represented in Fig. 5.6 (where axes *x*, *y*, *z* are labelled), is composed by solid FE's (type CHX60 [112]), with 20 nodes and an integration scheme of 3×3×3 Gauss points. The beam and column are composed by cubic FE with an edge length of 100 mm, whereas the slab was divided along the thickness in 8 FE sized as 100×100 ×18.75 mm^3 each. Structural symmetry was applied to optimize the numerical analysis: only a quarter of two adjacent slab panels was modelled, as well as half of the beam that connects with those panels and one column. In this way, two symmetry planes were considered at the half spans of the slab, parallel to the *x* and *z* axes, as well as a symmetry plane parallel to the *y* and *z* axes.

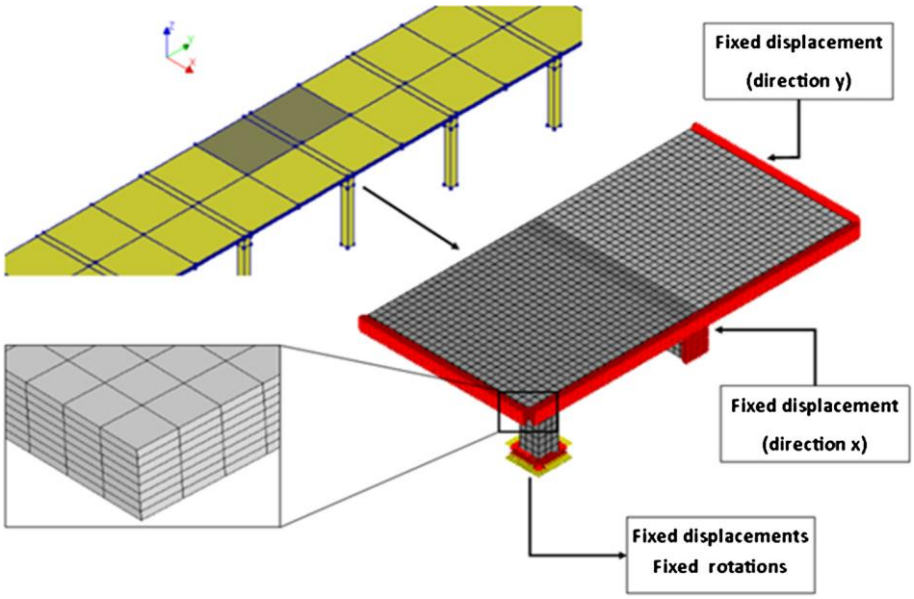

Figure 5.6 – FE mesh and symmetry conditions of the mechanical model.

The constitutive models of concrete and steel for simulation of the tension stiffening effect in the cracking behaviour, as detailed in sub-section 4.2.2.2, are determined by considering the MC10 formulation for calculation of maximum transfer length $L_{s,max}$. Calculation of $L_{s,max}$ is dependent on the percentage of reinforcement in the effective area $\rho_{s,eff}$, which varies over time and over the slab geometry, depending on the area of reinforcement and axial and bending stresses combination at each instant and position. However, the variation of L_s has a small influence on the constitutive model for concrete in tension because it only affects the inclination of the descending branch. The influence of $\rho_{s,eff}$ on the constitutive model of steel is only noticed when there is yielding, which does not happen in the analyses performed in this service limit state. Therefore, the constitutive models of the materials are determined considering $L_s = 0.1\ m$ and $\rho_{s,eff} = 1.9\ \%$ (equivalent to the average values calculated for the two reinforced zones and disregarding the effect of the axial stresses). Crack widths are calculated by integrating crack-inducing strains over a distance equal to twice the transfer length L_s. The transfer length is calculated for each position, according to MC10 formulation, taking into account the local axial and bending forces at long term, and the local reinforcement ratio.

The thermal strains imposed in the nodes of the TMS and THMS models, resulting from the temperature field determined in the thermo-hygrometric analysis, are based on the assumption of a constant coefficient of thermal dilation α_c since the setting time of concrete. In fact, most of the significant initial evolution observed in the coefficient of thermal expansion of concrete at very early ages occurs before setting. It remains fairly constant after that, except for concrete compositions with very low w/c ratios [159], which

is not the case of the concrete composition considered in this study. The uniform drying shrinkage strain imposed on the slab for the MS and TMS was determined experimentally by Azenha *et al.* [141]

5.3.3 Analysis of results

The main results of THMS are addressed in this chapter, with focus on the findings obtained due to the specific nature of the inherent multi-physics approach, and on the main differences with more simplified approaches (TMS and MS). To facilitate the comprehension of the results presented herein, some key points of the analysis are shown in Fig. 5.7: (i) two points P1 and P2 (near the support and at mid-span, respectively) of the reinforcement zone Z2, located at 1.25m from the outer border of the slab, and (ii) two points P3 and P4 (near the support and at mid-span, respectively) of reinforcement zone Z1, located over the longitudinal axis of the supporting column, where the bending moments are higher. Points P1 and P3 were located strategically at the centre of the first slab finite element, immediately adjacent to the edge of the supporting column.

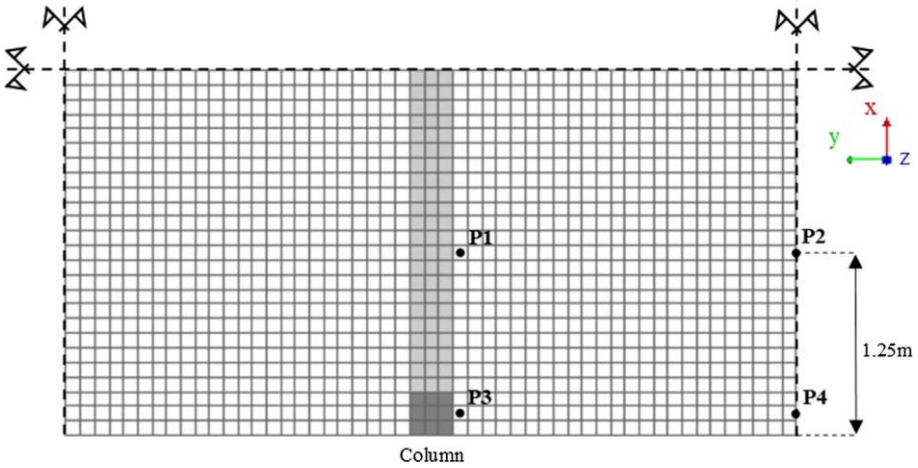

Figure 5.7 – Top view of the slab and points considered in the discussion of the results.

5.3.3.1. Evolution of temperature and drying shrinkage

Results from the thermo-hygrometric analysis (temperature and drying shrinkage strains along the slab thickness) are presented in Fig. 5.8, with reference to several key instants, labelled as A to K.

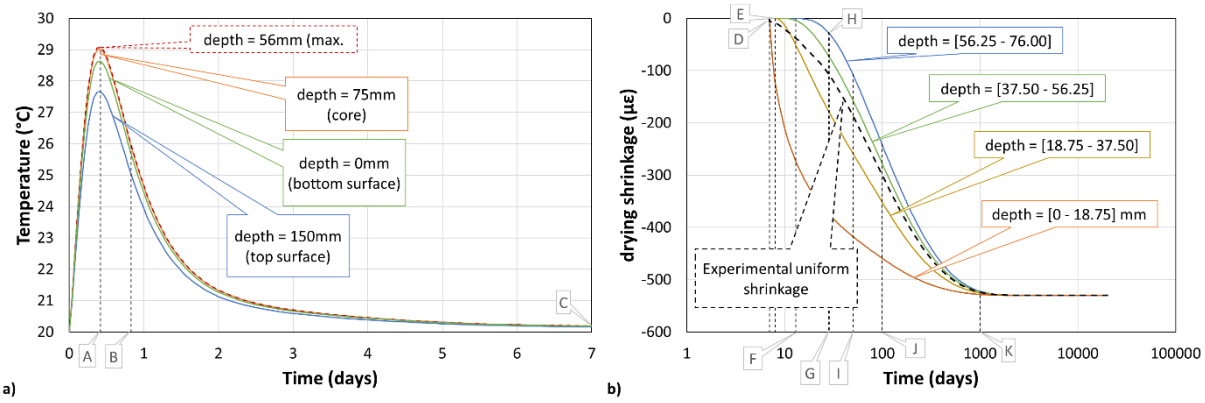

Figure 5.8 – Results from the thermos-hygrometric analysis: a) T during the first 7 days (linear scale of time); b) drying shrinkage over 50 years (log scale of time).

Due to the small thickness of the slab, the temperature rise induced by the cement hydration heat release is relatively small, as it can be observed in Fig. 5.8a. Starting from a fresh concrete temperature of 20 °C the maximum T (29.1°C) is reached near the core of the slab at the instant A (10h), corresponding to a maximum gradient of 1.4°C between the core and the top concrete surface. At 7 days (instant C), before formwork removal, the equilibrium of temperature between the slab and the environment (at 20°C) is already reached. Although the gradient of temperature induced in the slab due to heat of hydration is small, non-negligible stress levels are expected at early ages, due to the high restraint to deformation caused by the adopted support conditions.

Fig. 5.8b shows the drying shrinkage strains, based on the evolution of the humidity field of the slab, in 4 different depths considered in the THMS analysis, as well as the uniform shrinkage to be imposed in the TMS and MS analyses (which represents the evolution of the bulk shrinkage strain of a specimen with a thickness of 0.15 m, without any restraint to deformation). The slab is completely sealed until 7 days of age and is exposed to an environment with a RH of 60% after formwork removal. In the THMS a significant gradient of the drying shrinkage strains between the surface and the core of the slab is observed during the first days of analysis, motivated by a slower decrease of humidity in the interior layers. For instance, at 28 days (instant G) the drying shrinkage has already reached 70% of its maximum on the slab's surface, but only 5% in the core. The equilibrium of moisture between the slab and the environment is reached around 1000 days, corresponding to the instant K when the drying shrinkage becomes uniform and constant with a final value of 530 με.

5.3.3.2. Restraint force and crack pattern

The evolution of the global longitudinal axial force (calculated from the y-direction reactions at an x-z symmetry plane), averaged along the slab width, is shown in Fig. 5.9 for all analyses. The axial force

acting in the slab is constant along the transversal and longitudinal direction, except for the longitudinal profile over the axis of the supporting column, where the force is higher near the column and smaller at the mid-span (with differences up to 40% of the average axial force).

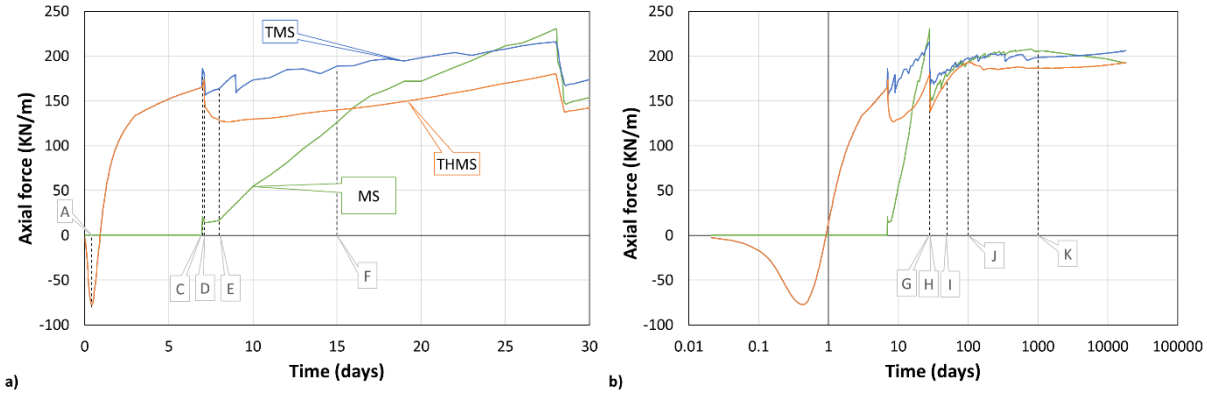

Figure 5.9 – Evolution of axial force for different simulations: a) first 30 days (linear scale of time); b) 50 years (log scale of time).

During the first hours of the THMS and TMS analyses, the restriction of the thermal deformation caused by the heat of hydration induces an axial compression force in the slab. The axial force applied to the slab increases until the instant A (approximately 10 h), when the temperature reaches the maximum value, up to a value equal to −80kN/m. As the slab temperature decreases and reaches equilibrium with the environmental temperature (20 °C), the axial force acting in the slab decreases, inverts the sign at instant B (approximately 20 h) and reaches a tensile force of 165kN/m at 7 days, immediately before the removal of propping and formwork (instant C). This tensile force is induced by the cooling that occurs subsequently to the initial temperature peak, being strongly influenced by the early age viscoelastic behaviour of the concrete.

After removal of propping and formwork at instant D (7.125 days), corresponding to the application of the self-weight and beginning of the drying shrinkage, two distinct behaviours are observed between simulations with non-uniform (THMS) and uniform shrinkage (TMS), regarding not only the evolution of axial force, but also the evolution of the crack pattern. Fig. 5.10 shows, at four instants, the crack patterns along the slab thickness for both the THMS and TMS, which are representative of the overall behaviour observed in the simulations with non-uniform and uniform drying shrinkage. The vectors displayed on the FE represent in-plane principal components of the crack strains (E_k) along the longitudinal section over the P3-P4 axis, where the bending moments are maximum. Additionally, the figure depicts the bending moment diagrams calculated by integrating the primary Cauchy stresses in the FE's located on the axis P3-P4 [112].

The self-induced stresses due to differential shrinkage on the THMS generate cracking near the support and at mid-span (where bending moments are higher) after formwork removal and cause the top and bottom surfaces of the slab to be almost integrally cracked, along the entire slab's longitudinal development, only a few days after formwork removal (Fig. 10a). This superficial cracking pattern is responsible for a stiffness decrease, and consequently, a decrease of the axial restraint force. On the other hand, the cracking pattern on the TMS (where a uniform drying shrinkage strain is imposed along the thickness) is limited to the regions of maximum negative bending moments, and cracks are induced at later ages (Fig. 10b). For this reason, the axial tensile force acting in the slab due to restraining of the drying shrinkage after formwork removal reaches higher values in the TMS and MS analyses (216 kN/m and 230 kN/m, respectively), during the period when the slab is only subjected to its self-weight.

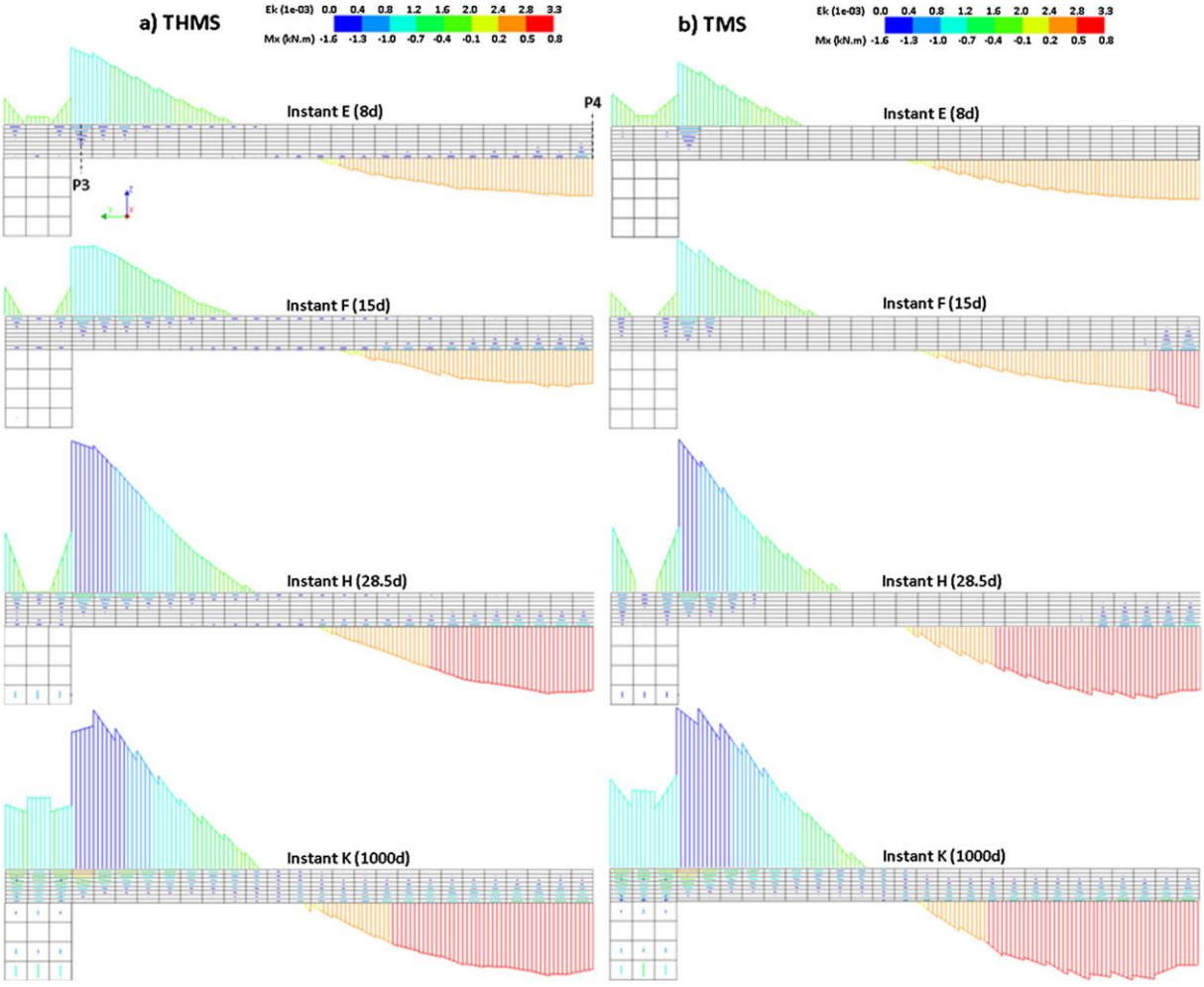

Figure 5.10 – Crack pattern and bending moments on a longitudinal section over P3-P4 axis (y direction): a) THMS; b) TMS.

At the age of 28 days (instants G and H), live and the additional permanent loads are applied, resulting in an increase of cracking, and consequently a relief of axial force acting in the slab. The drop of the restraint force is conditioned by the degree of cracking on the slab at the time of application of load, being

considerably smaller in the THMS and TMS (42 and 47 kN/m, respectively), in comparison to the MS (84 kN/m). Even though the differences of the restraint force acting in the slab are mitigated after application of the live and the additional permanent loads, this value is still smaller for the THMS.

As the drying advances towards the slab core, the restraint force in the THMS increases up to a value of 193 kN/m at instant J (100 days), slightly decreasing afterwards, due to the dominance of creep effects in comparison to the imposed shrinkage strains that have developed significantly at such age. At long term, the crack pattern and restraint force acting in the slab is very similar for the 3 analyses (THMS, TMS and MS).

On account of the lack of more explicit recommendations, designers are often inclined to consider a restraint force equal to the cracking force of the concrete ($N_{cr} = A_c \cdot f_{ctm}$) as a conservative approach for this kind of structures. However, it is possible to observe that, for the 3 simulations performed, the maximum value of the restraint force throughout the entire analysis is considerably smaller than $N_{cr} = 0.15 \times 1 \times 2900 = 435\ kN/m$. The maximum restraint force observed in the THMS, TMS and MS represent 44%, 49% and 53% of N_{cr}, respectively, and the restraint force acting in the slab at the end of the analyses represent 44%, 47% and 44% of N_{cr}, respectively.

5.3.3.3. Concrete stress profile

Fig. 5.11 shows, for the THMS and TMS, the relation between the longitudinal stress and the imposed drying shrinkage strains along the slab thickness, over a representative point of the slab at mid-span (P2), for several instants after formwork removal.

At the age of 7 days the slab is subjected to the actions of self-weight and restrained drying shrinkage, and 3 hours after beginning of concrete drying (instant D) the effect of the self-induced stresses due to the differential drying in the THMS is already noticeable, with higher tensile stresses on the surface in relation to what is observed in the case of the TMS.

At instant E (8 days) the top surface of the slab is already cracked near the support in the THMS, resulting in the reduction of the tensile stress to a value equal to $\beta \cdot fctm = 0.96\ MPa$, in compliance with the considered material behaviour.

At instant F (15 days) cracking in point P2 for the TMS is already noticeable (induced at the age of 9 days). As the restrained imposed shrinkage increases for both simulations, an increase of tensile stresses in non-cracked depths is noted (instants F and G), which is in correspondence with the increase of the restraint force observed in Fig. 5.9, during this period. After application of the live and additional

permanent loads at instant H (28.5 days), the compressive stresses at the top of the slab are increased for two main reasons: (i) the growth of bending moments due to the external loading increase; (ii) the decrease of the tensile restraint force, due to the progression of cracking in the slab induced by the additional loads.

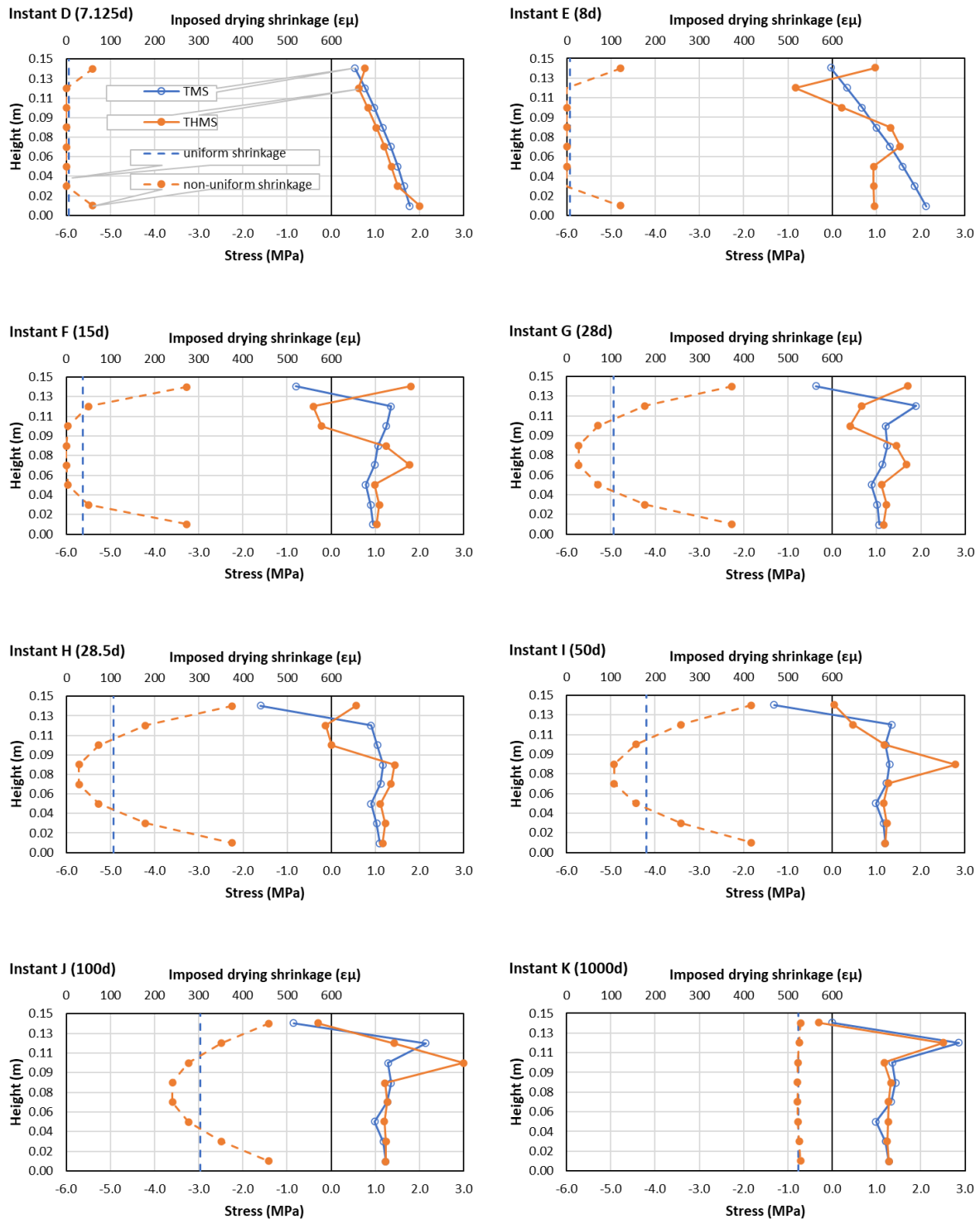

Figure 5.11 – Stress profiles over point P2 for different instants of the THMS and TMS.

The main differences between stress profiles of the THMS and TMS took place during the first 100 days of analysis (instant J). As the imposed drying shrinkage reaches its final value, stresses along the slab thickness for both simulations get closer, and the differences observed for the final value of the axial force acting in the slab can be interpreted as a result of different creep histories.

5.3.3.4. Crack width and SLS design

The evolution of crack width at the surface and at the reinforcement level, for points P1 to P4, are presented on Fig. 5.12 and Fig. 5.13, respectively. These points represent the location of maximum crack strains observed on top (P1 and P3) and bottom (P2 and P4) layers of the slab for each reinforcement zone (Z1 and Z2).

It can be observed that immediately after removing the formwork (instant D) cracks are induced in the slab, near the support (points P1 and P3) for the THMS and TMS. The surface crack on the THMS develops faster in the first 100 days, however, as the imposed drying shrinkage reaches its final value, the effect of creep on crack development becomes more predominant and the crack on the THMS is exceeded or matched by the crack on the TMS. In points P2 and P4, at mid-span, cracking arises on the TMS at a later age, as it would be expected from the crack pattern presented in Fig. 5.10. Since the effect of heat of hydration is disregarded on the MS, the cracks near the support and at mid-span are induced at much later ages, and it is observed that, in general, the final width is smaller than in the THMS and TMS, where thermal deformations at early ages were considered.

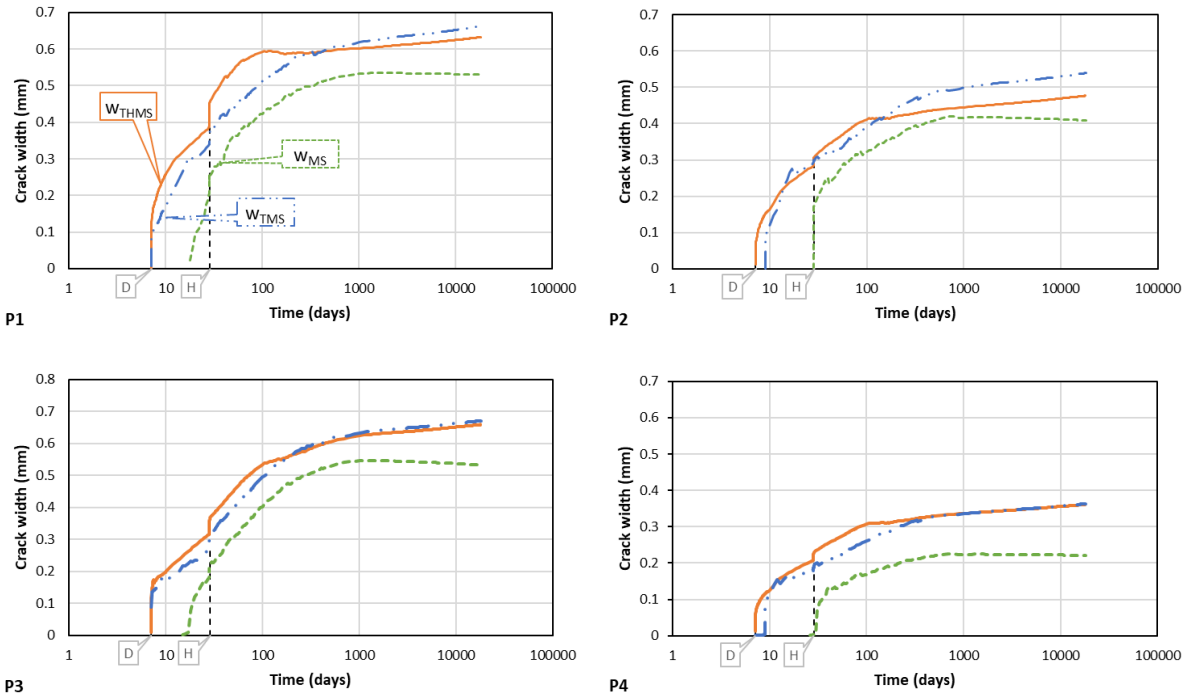

Figure 5.12 – Evolution of crack width at the slab surface.

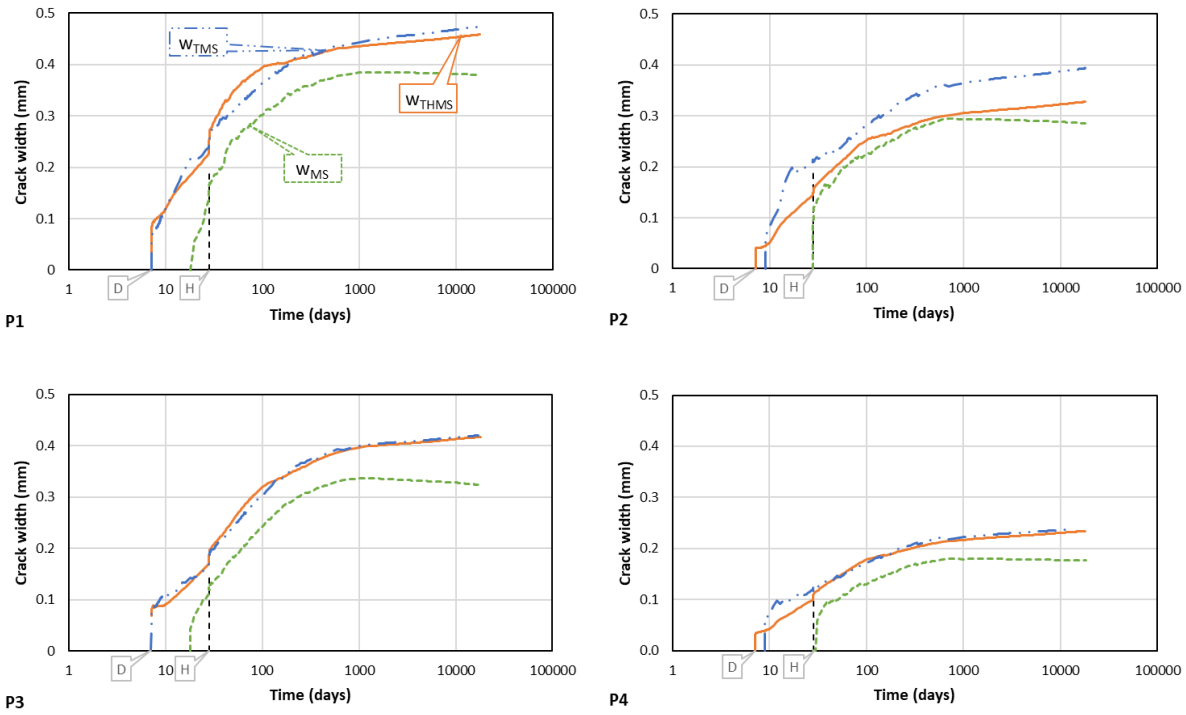

Figure 5.13 – Evolution of crack width at reinforcement level.

The crack opening at the surface level is significantly higher than at the reinforcement level. In RC members subjected to bending this difference is higher for thinner members. However, the limit crack width ($w_d < 0.3\,mm$ for an exposure class XC3 according to EC2) is the value which should not be exceeded at the reinforcement level, as indicated implicitly in the norm. For the THMS (Fig. 5.13), this

limit value is largely exceeded in several points. Therefore, the design approach considered in Section 3.1 is not on the conservative side, and the required quantity of reinforcement must be determined so that $w_d < 0.3\ mm$ at the critical positions: mid-span and support, in zones Z1 and Z2 (Fig. 5.2).

The SLS design procedure proposed by Sousa, et al. [160] can be used for that purpose. It consists of three steps: (i) a first non-linear analysis is performed with a plausible, yet not accurate, amount of reinforcement; (ii) based on the bending moments and axial forces determined in the first analysis it is possible to quantify a new reinforcement solution for controlling the crack width; (iii) considering the reinforcement determined in the step (ii) a second non-linear analysis is performed. With this last analysis it should be possible to conclude that the bending moments and axial forces acting in the slab do not change significantly with the new reinforcement, hence, the crack width should be within the limits considered in the reinforcement design. If not, steps (ii) and (iii) have to be repeated.

The first step of the procedure was attained with the THMS, whose results were shown before. For the second step, a new reinforcement solution (shown in Table 5.3) was designed with the MC10 formulation, in order to control the crack width of each representative point (P1 to P4) under a maximum value of 0.3 mm. The design was performed in accordance with the bending moments and axial forces determined for each point in the THMS, for the last step of analysis.

Table 5.3 – Design of new reinforcement ($N \neq 0$)

	Support Z1	**Mid-span Z1**	**Support Z2**	**Mid-span Z2**
Reinforcement zone	Z2 - top	Z2 - bottom	Z1 - top	Z1 – bottom
M_{cqp} **(kN.m/m)**	9.9	5.5	15.9	7.7
N_{Rest} **(kN/m)**	189	196	247	181
$A_{s,req}$ **(cm²/mm)**	8.70	7.54	11.3	7.54
A_s	Φ12//0.13	Φ12//0.15	Φ12//0.10	Φ12//0.15
$w_{d,MC10}$ **(mm)**	0.28	0.29	0.27	0.3

Finally, the third step was attained by performing a second thermos-hygro-mechanical simulation (THMS#2), with the longitudinal reinforcement shown on Table 3. Fig. 5.14 shows the evolution of crack width over time, for points P1 to P4, determined with both the THMS and THMS#2.

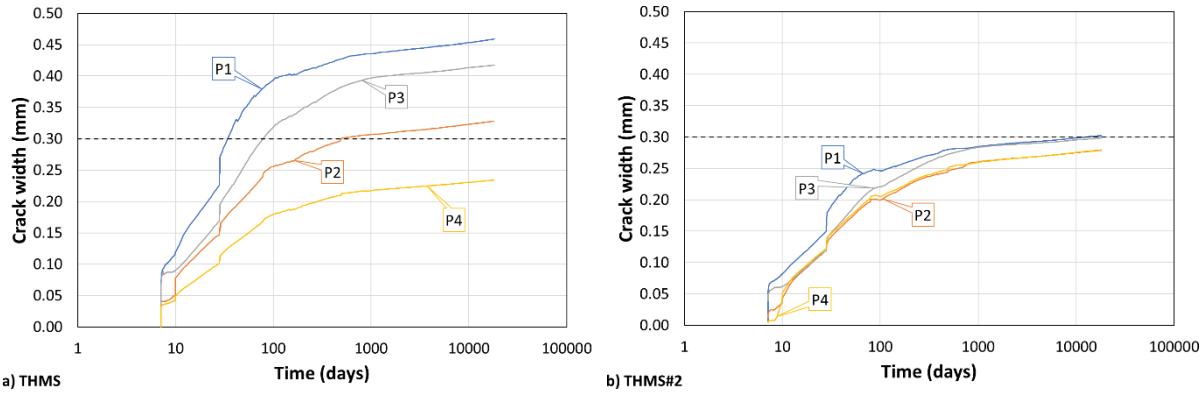

Figure 5.14 – Evolution of the crack width at the reinforcement level using the MC10 formulation: a) THMS; b) THMS#2.

It is observed that the method deployed here is suitable, allowing the quantification of the reinforcement necessary to control the crack width under 0.3 mm, at long term, without over-design. It was validated that minor changes on the reinforcement solution have very little influence on the internal forces acting in the slab, hence, one single non-linear analysis should be enough to design the reinforcement solution for the control of crack width.

5.3.4 Influence of reinforcement ratio

In this subsection, the structural behaviour of the slab, simulated with the thermo-hygro-mechanical model, is compared for 5 distinct quantities of longitudinal reinforcement, according to Table 5.4

Table 5.4 – Reinforcement solution for 5 different scenarios.

Scenario	Z2 - top $M_{cqp} = 9.1\ kN.m$	Z2 - bottom $M_{cqp} = 6.6\ kN.m$	Z1 - top $M_{cqp} = 19.2\ kN.m$	Z1 – bottom $M_{cqp} = 8.4\ kN.m$
1 – THMS	Φ10//0.15	Φ10//0.15	Φ10//0.10	Φ10//0.10
2 - THMS#2	Φ12//0.13	Φ12//0.15	Φ12//0.10	Φ12//0.15
3	Φ12//0.16	Φ12//0.18	Φ12//0.12	Φ12//0.15
4	Φ10//0.18	Φ10//0.25	Φ10//0.11	Φ10//0.20
5	Φ16//0.15	Φ16//0.15	Φ16//0.13	Φ16//0.15

Scenario 1 ($\rho_s = 0.8\%$) and scenario 2 ($\rho_s = 1.2\%$) are the reference scenarios, analysed in the previous subsections as THMS and THMS#2, respectively. The former model was designed for ultimate limit state, disregarding the effect of restraint force, and the latter was designed to meet crack requirement ($w_d \leq 0.3\ mm$) in service limit state, considering the restraint force and bending moments determined with THMS.

Scenario 3 ($\rho_s = 1.0\%$) is the reinforcement solution that corresponds to the average reinforcement area between Scenario 1 and Scenario 2. Scenario 4 ($\rho_s = 0.6\%$) and Scenario 5 ($\rho_s = 1.9\%$) are, respectively, the lower and higher boundaries of the parametric analysis, in which the design criteria is the same as for Scenario 2, but considering the extreme situations where the restraint force acting on the slab is equal to zero ($N = 0$) and equal to the cracking force of the concrete ($N = N_{cr}$), respectively.

Fig. 5.15 shows the evolution of the global longitudinal axial force, averaged along the slab width, for all considered scenarios of reinforcement.

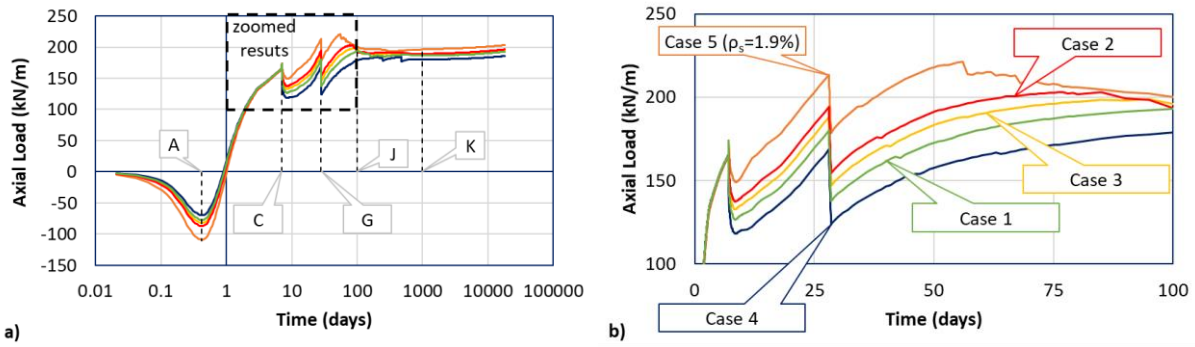

Figure 5.15 – Evolution of restraint force for different scenarios: a) over 50 years (log scale of time); b) zoomed results for the first 100 days of analysis (linear scale of time).

As already observed in sub-section 5.3.3.2, during the first hours, the restraint of the thermal strains caused by heat of hydration induces an axial compression force in the slab that reaches its maximum value at 10 h (instant A). Due to the additional self-induced stresses caused by different thermal strains acting on concrete and steel reinforcement, the maximum axial force reached at instant A is higher for higher reinforcement ratios and varies between –70 kN/m for Scenario 4 ($\rho_s = 0.6\%$) and –109 kN/m for Scenario 5 ($\rho_s = 1.9\%$).

Before formwork removal at 7 days (instant C), the tensile force that is induced by the cooling that occurs after the temperature peak at instant A is approximately the same for all scenarios. Even though the development of this tensile force depends on the early age viscoelastic behaviour of the concrete at early ages, the differences regarding the peak compressive force induced in the slab at instant A do not significantly influence the value of the tensile restraint force observed immediately before instant C, which varies between 164.6 kN/m for Scenario 5 ($\rho_s = 1.9\%$) and 165.4 kN/m for Scenario 4 ($\rho_s = 0.6\%$).

After formwork removal and consequent activation of the self-weight and drying of concrete, cracking is induced near the support and at mid-span (where bending moments are higher), which is responsible for the stiffness decrease and consequent reduction of the restraint force. This is also observed at 28 days (instant G), when live and additional permanent loads are applied, resulting in an increase of cracking

and consequent relief of the restraint load. These drops of restraint force and further evolution over time are conditioned by the degree of cracking and consequent loss of axial rigidity, therefore, the axial load acting on the slab during the crack formation stage is higher for higher reinforcement ratios.

As the concrete drying advances, the restraint force continues to increase up to an instant that varies between 56 days (for Scenario 5) and 240 days (for Scenario 4), slightly decreasing afterwards until 1000 days (instant K) when the drying shrinkage becomes uniform and constant. This decrease of restraint force can be justified by the dominance of creep effects in comparison to the imposed deformations and by the specific nature of concrete shrinkage (as opposed to a global imposed deformation).

At long term, the restraint force observed for all reinforcement scenarios tend to converge until instant K, being approximately constant afterwards, in correspondence to the stabilization of loads and drying, and the fact that creep effects are already very small at these late ages. The restraint force observed at the end of the analysis (50 years) varies between 186 kN/m (43% of N_{cr}) for Scenario 4 and 203 kN/m (47% of N_{cr}) for Scenario 5. These values are at the same magnitude as the maximum restraint force, observed for Scenario 5 (with higher reinforcement ratio), which reached a value of 221 kN/m (51% of N_{cr}).

The evolution of the crack width, at reinforcement level, is presented on Fig. 5.16 for points P1 to P4.

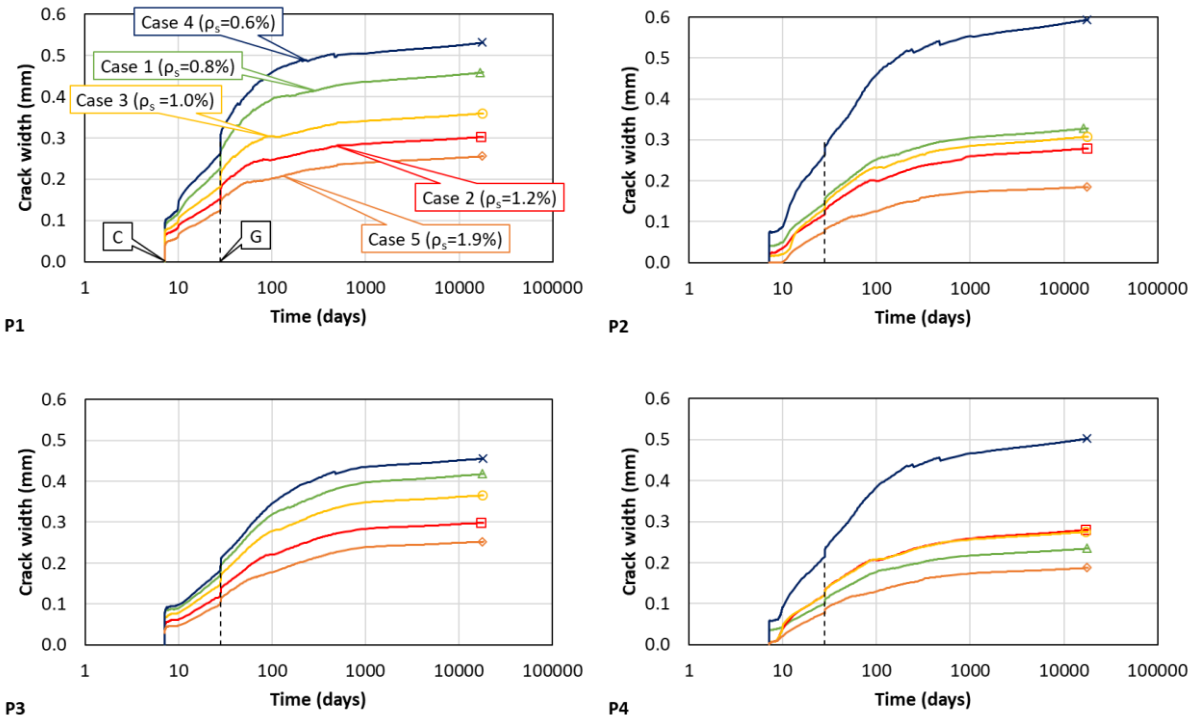

Figure 5.16 – Evolution of crack width at the reinforcement level.

For all the analyses, cracking is induced at support (P1 and P3) and mid-span (P2 and P4), in both reinforcement zones, immediately after removal of formwork at instant C due to the combined effect of the slab's restrained shrinkage and self-weight. At instant G, when live and additional permanent loads are applied, the growth of bending moments causes a sudden increase of the crack width that is, as expected, more pronounced for Scenario 4 ($\rho_s = 0.6\%$) with lower reinforcement ratio.

At the end of the analysis, the maximum crack width observed in all representative points was below the limit crack width value only for Scenarios 2 ($\rho_s = 1.2\%$) and 5 ($\rho_s = 1.9\%$), in which the design was performed taking into account a restraint force caused be imposed deformation.

Whereas for Scenario 5 a very conservative approach was followed, in which a restraint force equal to the axial cracking force of the concrete ($N_{cr} = 435kN/m$) was considered, the reinforcement for Scenario 2 was designed taking into account the exact restraint force determined with the numerical THM simulation (considering the amount of reinforcement previously quantified for Scenario 1). The maximum crack width observed for Scenario 2 is close to the expected crack width according to Model Code formulation and not much higher than the maximum crack width observed for Scenario 5 (differences of 0.05mm at the support and 0.1mm at mid-span).

5.3.5 Prediction of restraint force with simplified approach

In this sub-chapter, the sectional approach proposed in Chapter 4 is applied to predict the service life restraint force endured by the slab of the presented case study.

For simplification of calculations, the analysis is limited to the length of the free span, which is divided in 47 sections of 5cm width, as shown in Fig. 5.17. The reinforcement that is considered is the same as for the THMS. The bending moments are calculated with a linear analysis by integrating the primary Cauchy stresses in the FE's over the slab's width, considering the same FE mesh and quasi-permanent combination of loads of the THMS.

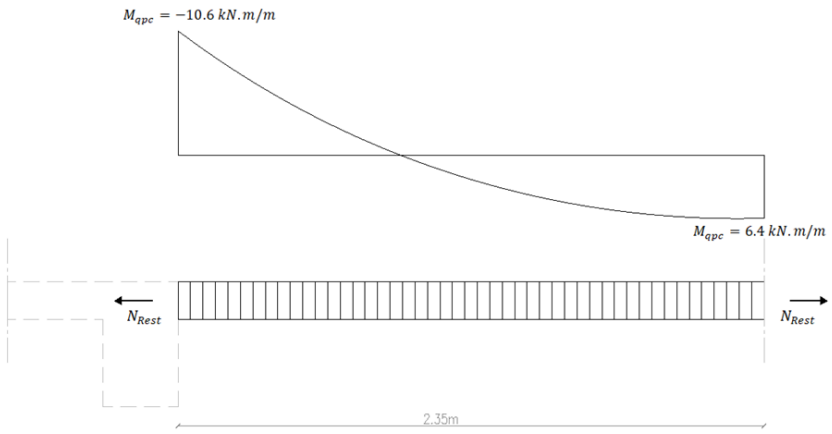

Figure 5.17 – Schematic representation of the slab's free span divided into sections.

The cracking length within the free span is assessed for the following instants: i) at 28 days, immediately after application of vertical loads; ii) at 100 days of age, when, according to the analysis performed in sub-chapter 5.3.3, the effect of creep on the slab's axial stress starts to override the effect of restrained shrinkage; iii) at the end of analysis, 10000 days.

Table 5.5 shows the calculated cracked length $L_{cracked}$ for each instant, considering a restraint force N_{Rest} of 200 kN/m in the first iteration.

Table 5.5 – Calculated cracked length in the first iteration.

Time	p	N_{Rest}	ε_{sh}	$E_{c,eff}(28,t)$	$E_{c,adj}(7,t)$	f_{ctm}	$f_{ctm,fl}$	$L_{cracked}$ (m)		
(days)	**(kN/m²)**	**(kN/m)**	**(με)**	**(GPA)**	**(GPa)**	**(MPa)**	**(MPa)**	M^-	M^+	**Total**
28	6.35	200	100	33.0	17.6	2.9	4.2	0.15	0	0.15
100	6.35	200	300	15.0	14.5	3.1	4.5	0.10	0	0.10
10000	6.35	200	530	10.3	10.6	3.3	4.8	0.05	0	0.05

At the final iteration, the calculated axial strain in the free span is $\varepsilon_G(10000) = -10\mu\varepsilon$, as resumed in Table 5.6, which is close to full restraint. Therefore, no further discretization of the free span was needed.

Table 5.6 – Calculated restraint force: first and final iterations.

	p **(kN/m²)**	N_{Rest} **(kN)**	$L_{cracked}$ **(m)**			$\varepsilon_{G,calculated}$ **(με)**	$\varepsilon_{G,expected}$ **(με)**
			M^+	M^-	**Total**		
First iteration	6.35	200	0.15	0	0.15	-278	0
Final iteration	6.35	276	0.35	0.20	0.55	-10	

The calculated restraint force of $N_{Rest} = 276\text{kN/m}$ represents 63% of the concrete's cracking force N_{cr}, which is a conservative estimation regarding the maximum restraint force observed in the analyses performed in sub-chapter 5.3 with the FE based models (220kN/m). These differences are motivated by simplifications adopted in the proposed model (e.g., tension stiffening effect is disregarded and the criteria for crack initiation is not based on the softening behaviour and fracture energy of concrete, but in a weighted value $f_{ct,w}$ instead, as explained in sub-chapter 4.3.2. Nevertheless, the calculated value significantly lower than N_{cr}, leading to a safe but still economical design of the reinforcement.

It is also worth comparing the restraint force obtained in the analyses performed in sub-chapter 5.3 with the value estimated with the simplified method of Camara and Luís [13]. In this method, the restraint force can be estimated as $\xi \cdot N_{cr}$, where ξ is a reduction coefficient given in Table 5.7.

Table 5.7 – Reduction coefficient ξ as proposed by camara and Luís [13].

Reinforcement ratio	Shrinkage imposed deformation		
	200με	**300με**	**500με**
0.5%	0.40	0.45	0.50
0.8%	0.40	0.40	0.45
1.0%	0.35	0.35	0.40

Considering a restrained shrinkage deformation of 500με and a reinforcement ratio of 0.8%, the estimated restraint force is $N = \xi \cdot N_{cr} = 0.45 \times 435 = 196\ kN$. This is close to the average axial force acting in the slab in the THMS (see Table 5.3), with the exception of point P3, near the column (the simplified method does not account for local effects in discontinuity regions).

Even though the methods applied in this sub-chapter do not account for the effects of heat of hydration and non-uniform drying shrinkage, both give a decent estimate for the restraint force in this kind of structure (solid, thin, slab), because the force at long-term is not very sensitive to such effects, as shown in Figs. 5.12.

Chapter 6

Conclusions and further developments

6.1 Conclusions

The work presented in this thesis contributes to a deeper understanding of the complex interaction that occurs between self-imposed deformations (particularly due to drying shrinkage), concrete viscoelasticity and cracking in the service life behaviour of RC slabs. This was achieved with the employment and comparison of simulation models, with different levels of complexity, in the analysis of a fully restrained solid slab. These models were validated with a long-term experimental campaign on RC slabs subjected to restrained shrinkage and bending stresses in correspondence with a realistic service load. Additionally, a simplified approach for prediction of the long-term restraint force installed in the slab was proposed and validated with the experimental data.

In Chapter 2, the two main topics addressed in this work were introduced. The main experimental techniques, existing in current literature, for testing concrete or RC behaviour under restrained deformation were resumed. It was shown that each experimental setup has its limitations and purposes, therefore, the restraint device should be built accordingly to the type of information that is intended. Additionally, a multi-physics framework based on FE method for analysis of the thermos-hygro-mechanical behaviour of RC structures was presented. Such method enables the simulation of self-induced stressed caused by non-uniform distribution of moisture and temperature, thus providing more accurate results. However, it requires an extensive material characterization of concrete regarding thermal and hygrometric properties, being less suitable for applications outside scientific investigation.

In Chapter 3, the long-term experimental campaign undertaken in this thesis for simulation of the combined effects of restrained shrinkage and vertical loads on RC slabs was presented. A new experimental method was applied, in which a restraint device is used to constrain the drying shrinkage-induced axial deformations of slab-like specimens, while allowing the simultaneous endurance of bending and shear stresses.

The preparation of the experimental campaign proved to be successful, in the sense that most problems associated to experiments of this nature were overcome: (i) the micro-management plan for the casting day was of paramount importance to enable the adequate casting of three slabs and two dummy specimens, highly instrumented, in a very confined environment and without equipment failure; (ii) the adopted formwork and propping solution allowed a smooth assembling, demoulding and removing of the formwork from the climatic chamber, without significant deformation of the slab during casting and curing

periods; (iii) an economical solution for the construction of a climatic chamber, with a net area of 3.6×4.9 m^2, was able to control the environmental conditions under a desired limited variation of T and RH.

The monitoring devices showed satisfying results at key instants. The slabs showed an expectable behaviour before cracking, and the overall differences between the structural behaviour for the three slabs were consistent with the respective level of restraint and vertical loading. The reliability of the devised measuring system for determination of the longitudinal strains on the control region was demonstrated for the period before significant cracking has been induced. Estimation of in-plane deformations of the slabs, based on the measured steel strains and drying shrinkage of concrete, during the aforementioned period, showed a good correlation with the experimental measurements.

Temperature measurements at the core of the slabs allowed the detection of the evaporative cooling effect, during formwork removal at 7 days, when the temperature of the slabs (already in equilibrium with the environment) underwent a sudden drop to values bellow the environmental temperature. This effect had a nonnegligible influence on the compressive strains observed in the rebars, during the same period of time.

Measurements of the concrete RH profiles showed that drying due to self-desiccation was negligible, as would be expected for a high w/c ratio mixture [147]. The natural tendency for thicker specimens to present higher RH values, for the same depth, as a result of the water transportation from the core to the surface of the specimens [141], was also confirmed.

Results regarding the characterization of the tensile strength of concrete were in line with the most recent state-of-the-art. The adoption of a conversion factor α_{sp} higher than 1 (following Malárics and Müller [143], formulation) for the splitting tests performed at 7 and 28 days resulted in tensile strength values coherent with the flexural tests performed at 51 and 499 days (taking into account that a cement for high early strength concrete was used).

Different crack widths measured in restrained slabs, during the period in which both slabs were subjected to the same loading, indicates that the crack width development is sensitive to the variation of concrete properties within two different specimens of the same cast. This difference in the behaviour during the crack formation stage had significant impact in the stains observed in the control region of each slab, for the same period of time.

Substantial differences between the strains calculated in the cross section at mid-span and the measured strains on the reinforcement were observed. These differences were most likely to be caused by: (i)

influence of the bond action between reinforcement and concrete and the length of the strain gauge on the measured average strain (which will always be smaller than the calculated punctual maxima); (ii) discrepancies between the exact location of the sensor in relation to the crack (which is irregular by nature).

The percentage of the cracking force N_{cr} that was necessary to apply to SLAB1 in order to restrain its deformation is within the range observed for most studies on numerical simulations for assessment of the structural behaviour of longitudinally restrained slabs subjected to a service vertical loading.

The presentation of experimental conditions and results was thoroughly made in this thesis for two reasons: (i) to contribute for a successful implementation of the same type of complex programs in the future in other laboratories; (ii) to allow the wealth of results and observations to be used in the context of further numerical/analytical research, for which very clear information on experimental conditions, characteristics and results is of paramount importance.

In Chapter 4, the hygro-mechanical behaviour of the tested slabs presented in Chapter 3 is simulated with the multi-physics approach described in Chapter 2. Additionally, a simplified approach based on the compatibility of deformation is proposed and employed to calculate the restraint forces endured by the restrained sabs.

The measurement of RH profiles, performed in the experimental campaign, provided fundamental data for adjustment of the diffusion parameters of the slab's concrete. It was necessary to change the value of two parameters ($n = 15$ to $n = 5$ and $D_1 = 5.68e^{-10}\, m^2/s$ to $D_1 = 3.0e^{-10}\, m^2/s$), in relation to the values proposed by Model Code 2010 [10], so as to adequately simulate the evolution of the RH over time and for different depths of the tested specimens. The final set of values for the diffusion parameters were in the same order of magnitude with the values adopted in other hygrometric analyses performed on concrete specimens [141,147].

A 2D hygrometric analysis of the dummy specimens was performed with the adjusted diffusion parameters and the average experimental strains were adequately predicted by the numerical model in which the original formulation proposed by Kwak *et al.* [119] for determination of the drying shrinkage as a function of the relative humidity was considered.

The simulation of the tested slabs with the FEM 3D mechanical model, considering the two-dimensional non-uniform drying shrinkage field, enabled the validation of the multi-physics approach proposed by

Azenha [110], as well as the modelling strategies for simulation of creep and cracking of concrete described in Chapter 2.

The simplified method founded on the compatibility of deformation, employed for estimation of the long-term restraint forces in SLAB1 and SLAB2, based on the measured longitudinal strain on the control region, showed a good agreement with the experimental axial forces applied experimentally. The final crack width at mid-span was then estimated with EC2 and MC10 formulations for RC elements subjected to composed bending. In both design codes, the maximum value of crack spacing $s_{r,max}$ and transfer length $L_{s,max}$ is underestimated for all tested slabs, in which the aforementioned values are influenced by the position of the transversal reinforcement. Despite that, estimations of maximum crack with performed with the MC10 formulation (in which the effect of shrinkage between cracks is considered) were conservative.

In Chapter 5, a multi-physics numerical framework was applied for the analysis of the serviceability behaviour of a continuous solid slab, under the combined effect of external loads and restraints to imposed deformations (heat of hydration and drying shrinkage). The structural response was simulated from the setting time of concrete until the long-term (50 years). The case study considered is a housing floor, under a realistic serviceability load scenario, and unable to deform axially due to its connection to rigid walls. The slab was simulated with the full thermo-hygro-mechanical framework (THMS), with direct consideration of the non-uniform progress of drying shrinkage, as well as the early stresses caused by restrained thermal deformations. In order to understand the structural consequences of the aforementioned effects, two further simplified analyses were considered: firstly, the analysis TMS, that explicitly considers the T fields caused by hydration heat, but simplifies the modelling by considering a uniform distribution of shrinkage strains throughout the slab's thickness; secondly, the analysis MS that is similar to the TMS, but further neglects the temperature field and the corresponding imposed thermal deformations. Based on these analyses, the following conclusions can be drawn:

- Even though the slab is constituted by a normal strength concrete, with a small thickness (0.15 m), the restraining of the deformations due to the cement hydration heat release is not negligible. The tensile stresses observed in the THMS and TMS analyses, already acting on the slab at the time of formwork removal, significantly decreases the concrete capacity to resist further stresses in latter stages of the structural life.
- The analyses allowed to understand the structural implications of explicitly considering non-uniform drying shrinkage strains. In the THMS high superficial tensile stresses developed after

the end of the curing period and instant of formwork removal. Consequently, the superficial layer of concrete becomes cracked in almost all of the slab area, both at the top and bottom surfaces. Despite the fact that these superficial cracks reach the reinforcement, they do not fully penetrate into the slab depth before the remaining loads are applied at the age of 28 days.

- Even after these loads are applied, the crack patterns obtained in the THMS were significantly different from those obtained through the simplified analyses: in the latter, the cracks propagated deeper in the slab thickness, but they existed only in the regions of higher bending moments. Despite these differences, it is interesting to observe that, after applying the external loading, the restraint force in the slab was not significantly influenced by the heat of hydration effects and the non-uniformity of shrinkage strains.
- The multi-physics analysis framework allowed to understand the reason why such effects do influence the restraint force magnitude before the total external load application, but this influence tends to vanish in the long-term. This is a relevant conclusion for application in the design practice. Crack widths increase with time, as shown in the results of the application example. Therefore, crack width calculations should be made using the long-term restraint force. The fact that the latter is not significantly affected by the heat of hydration and drying shrinkage effects, in this type of thin solid slabs, is relevant for the development of simplified SLS design methodologies.

A sensitivity analysis was also performed in Chapter 5, where the structural behaviour of a slab with different solutions of steel reinforcement was assessed with a non-linear thermo-hygro-mechanical simulation. It was observed that different levels of reinforcement do influence the restraint force during the crack formation stage, however, this influence tends to vanish at long term. Additionally, the evolution of crack width over time, observed for all reinforcement scenarios, showed the importance of considering the effect of restrained deformations for controlling the crack width under a pre-determined limit. However, it was also shown that conservative approaches where the cracking force of the concrete is considered as the restraint force leads to overdesign situations where the adopted reinforcement is significantly higher than the optimal solution.

It was also concluded that, for this type of slab (thin, solid RC slab), the simplified procedures proposed by Camara and Luís [13] and the one presented in sub-chapter 4.3 are valid for estimation of the long-term restraint force. The former method is based on a straightforward calculation of the restraint force by multiplication of a reduction coefficient with the concrete's cracking force. This reduction coefficient depends on the reinforcement ratio and restrained imposed deformation and is assessed through a table

that was developed based on the results of a set of non-linear structural analyses, in which the vertical loads were defined in relation to the adopted reinforcement (in order to correspond to a realistic service load condition). The latter method, which is based on the compatibility of deformation of the entire member length, is more time consuming but has a wider applicability.

6.2 Further developments

During the course of this thesis, some research perspectives associated with the developed theme have emerged, which due to time or resource limitations, were not deepened. Because the author considers these matters to be relevant, it is suggested in the following paragraphs some lines of investigation to be explored in the future.

- The deployment of the experimental campaign described in Chapter 3 under periodic stages of dry/moist environments, with periodic variation of the vertical loading and with a different restraint system to enable the combination of periods of passive restraint with periods of active (force controlled) restraint, would contribute to a more realistic simulation of the slab's hygro-mechanical behaviour and to the validation of numerical models under more complex scenarios.
- In-situ monitorization of slabs subjected to high levels of axial restraint would yield relevant information regarding real-scale slabs under realistic restraint conditions which cannot be accurately replicated in laboratory experiments. In this regard, the author had the opportunity, during the course of this thesis, to be involved in the planning and conduction of the following in-situ monitorizations of slabs subjected to the combined effect of vertical loading and significant axial deformations: i) a 70cm thick foundation slab, pertaining to the technical area from a commercial building, with a total length of ~71m in the longitudinal direction and confined by earth retaining walls; ii) a 25cm thick slab with a net area of ~60x60m^2, pertaining to an underground parking, confined by diaphragm walls. At the time of writing, the drying process of both slabs is still on an early stage and monitorization is still ongoing. The results provided by these experimental campaigns should enable the assessment of numerical and analytical models for prediction of the structural behaviour of axially restrained RC slabs subjected to realistic conditions, as well as the influence of the adopted simplifications.
- In Chapter 4, the calculation bases for determination of the restraint force with a sectional analysis founded on the compatibility of deformations were presented. For simplification of calculations, the tension stiffening effect was disregarded and the criteria for crack initiation is based in a weighted value between uniaxial and flexural tensile strength. The influence of these

simplifications should be studied for different element geometries and load levels. Additionally, the development of a user-friendly algorithm for automatic calculation of the restraint force, based on the material properties, element geometry, imposed deformations and external loads and degree of restraint, to be made available online, would facilitate the use of the proposed method in design.

Chapter 7

References

[1] S.A. Kristiawan, M.T.M. Aditya, Effect of High Volume Fly Ash on Shrinkage of Self-compacting Concrete, Procedia Eng. 125 (2015) 705–712. https://doi.org/https://doi.org/10.1016/j.proeng.2015.11.110.

[2] G. Pickett, Effect of Aggregate on Shrinkage of Concrete and a Hypothesis Concerning Shrinkage, ACI Journal Proceedings. 52 (1956) 581–590. https://doi.org/10.14359/11617.

[3] FIB, fib bulletin 92: serviceability limit state of concrete structures. 2019.

[4] Casal A., O Efeito das Deformações Impostas em Edifícios com Dimensões Significativas em Planta: Análise de Pilares e/ou Paredes de Alvenaria, MSc thesis, Universidade Técnica de Lisboa, Instituto Superior Técnico (IST), 2013.

[5] Bamforth P., CIRIA C766: Control of cracking caused by restrained deformation in concrete., (2018).

[6] CEN, EN 1992-1-1: Eurocode 2 Design of concrete structures Part 1-1 General rules and rules for buildings. (2004).

[7] CEN, EN 1992-3: Eurocode 2 Design of concrete structures Part 3: Liquid retaining and containment sttructures, (2006).

[8] ACI, ACI 224.2R-92: cracking of concrete members in direct tension (reapproved 2004). (2002).

[9] ACI, ACI 224R-01: control of cracking in concrete structures (reapproved 2008). (2002).

[10] FIB, fib Model Code for Concrete Structures 2010, Ernst & Sohn, Berlin, Germany, 2013.

[11] M. Azenha, C. Sousa, J. Granja, R. Faria, B. Zahabizadeh, Reinforcement design for the combined effect of restrained shrinkage and applied loads in slabs: a design challenge. In: International conference on sustainable materials, systems and structures (SMSS 2019) challenges in design and management of structures., in: Rovinj, Croatia, 2019.

[12] Azenha M, Granja J., Seminar: design of reinforcement for RC elements under the combined effect of applied loads and restrained shrinkage. (2017).

[13] J. Camara, R. Luís, Structural response and design criteria for imposed deformations superimposed to vertical loads., in: The Second Fib Congress, Naples, Italy., 2006: pp. 1–12.

[14] R. Luís, Análise e dimensionamento de estruturas de betão com sobreposição de cargas e Deformações Impostas, MCs, Instituto Superior Técnico, 2005.

[15] J. Carvalho, Estudo da fendilhação em lajes restringidas, devido ao efeito conjunto da retração e das ações distribuídas no piso., MCs, FEUP, 2013.

[16] C. Ribeiro, Estudo da fendilhação em lajes bi-direcionais restringidas, atendendo aos efeitos da retração e das ações gravíticas., MSc, FEUP, 2014.

[17] C. Sousa, E. Felisberto, R. Faria, Influence of restrained shrinkage in RC building slabs: a case study. in: International RILEM Conference on Materials, Systems and Structures in Civil Engineering – Conference Segment on Service Life of Cement-Based Materials and Structures. , Technical University of Denmark, Lyngby, Denmark., 2016.

[18] D. Schlicke, N.V. Tue, Minimum reinforcement for crack width control in restrained concrete members considering the deformation compatibility, Structural Concrete. 16 (2015) 221–232. https://doi.org/10.1002/suco.201400058.

[19] D. Schlicke, V.T. Nguyen, Crack width control: verification of the deformation compatibility vs. covering the cracking force, in: Proceedings of the International RILEM Conference on Materials, Systems and Structures in Civil Engineering 2016: Service Life of Cement-Based Materials and Structures, Lyngby, Denmark, 2016: pp. 563–572.

[20] D. Schlicke, N.V. Tue, J. Gomes, C. Sousa, M. Azenha, Analytical assessment of restraint forces and crack widths in end-restrained building slabs, Eng Struct. 224 (2020) 111218. https://doi.org/10.1016/j.engstruct.2020.111218.

[21] M. Azenha, C. Sousa, R. Faria, A. Neves, Thermo–hygro–mechanical modelling of self-induced stresses during the service life of RC structures, Eng Struct. 33 (2011) 3442–3453. https://doi.org/https://doi.org/10.1016/j.engstruct.2011.07.008.

[22] A. Jefferson, R. Tenchev, A. Chitez, I. Mihai, G. Coles, P. Lyons, J. Ou, Finite element crack width computations with a thermo-hygro-mechanical-hydration model for concrete structures, European Journal of Environmental and Civil Engineering. 18 (2014) 793–813. https://doi.org/10.1080/19648189.2014.896755.

[23] R.I. Gilbert, S. Nejadi, An experimental study of flexural cracking in reinforced concrete members under sustained loads. UNICIV report R-435. 2004.

[24] K. Kovler, Testing system for determining the mechanical behaviour of early age concrete under restrained and free uniaxial shrinkage, Mater Struct. 27 (1994) 324–330. https://doi.org/10.1007/BF02473424.

[25] D. Cusson, T. Hoogeveen, An experimental approach for the analysis of early-age behaviour of high-performance concrete structures under restrained shrinkage, Cem Concr Res. 37 (2007) 200–209. https://doi.org/10.1016/j.cemconres.2006.11.005.

[26] R. Faria, L. Leitão, L. Teixeira, M. Azenha, D. Cusson, A structural experimental technique to characterize the viscoelastic behavior of concrete under restrained deformations, Strain. 53 (2017) e12216. https://doi.org/10.1111/str.12216.

[27] B. Delsaute, S. Staquet, Monitoring of the creep and the relaxation behaviour of concrete since setting time, part 2 : tension, in: Strategies for Sustainable Concrete Structures (SSCS), 2012.

[28] L. Buffo-Lacarrière, A. Sellier, B. Kolani, Application of thermo-hydro-chemo-mechanical model for early age behaviour of concrete to experimental massive reinforced structures with strain–restraining system, European Journal of Environmental and Civil Engineering. 18 (2014) 814–827. https://doi.org/10.1080/19648189.2014.896754.

[29] Leitão L., Análise Termo-Higro-Mecânica das Tensões Autoinduzidas em Estruturas de Betão., PhD thesis, FEUP, 2018.

[30] K. Turner, D. Schlicke, N.V. Tue, Systematic investigation with restraining frames for reinforced concrete. In: 2° International RILEM/COST Conference on Early Age and Serviceability in Cement-Based Materials and Structures (EAC2), Brussels, Belgium, 2017.

[31] S. Mindess, D. Darwin, J.F. Young, Concrete 2nd Edition, Technical Documents. (2003).

[32] C. Meyer, The greening of the concrete industry, Cem Concr Compos. 31 (2009) 601–605. https://doi.org/https://doi.org/10.1016/j.cemconcomp.2008.12.010.

[33] P.K. Mehta, High performance, high-volume fly Ash concrete for sustainable development. In: Proceedings of the International Workshop on Sustainable Development and Concrete Technology, Beijing, China, 2004: pp. 3–14.

[34] A.C. Duran, High-Volume Fly Ash Concrete with High Strength and Low Drying Shrinkage, Journal of Materials in Civil Engineering. 15 (2003) 153–156. https://doi.org/10.1061/(ASCE)0899-1561(2003)15:2(153).

[35] P. Chindaprasirt, S. Homwuttiwong, V. Sirivivatnanon, Influence of fly ash fineness on strength, drying shrinkage and sulfate resistance of blended cement mortar, Cem Concr Res. 34 (2004) 1087–1092. https://doi.org/https://doi.org/10.1016/j.cemconres.2003.11.021.

[36] K. Binod, G.K. Tike, P.K. Nanda, Evaluation of Properties of High-Volume Fly-Ash Concrete for Pavements, Journal of Materials in Civil Engineering. 19 (2007) 906–911. https://doi.org/10.1061/(ASCE)0899-1561(2007)19:10(906).

[37] A. Borsoi, M. Collepardi, S. Collepardi, R. Troli, Influence of fly ashes on the drying shrinkage of superplasticised concretes in the presence of SRA. In: The 9th CANMET/ACI International Conference on Superplasticisers and Other Chemical Admixture in Concrete, Seville, Spain, 2009: pp. 287–296.

[38] A.E. Klausen, T. Kanstad, The effect of shrinkage reducing admixtures on drying shrinkage, autogenous deformation, and early age stress development of concrete, Structural Concrete. 22 (2021) E596–E606. https://doi.org/https://doi.org/10.1002/suco.201900583.

[39] RILEM, Early Age Cracking in Cementitious Systems - Report of RILEM Technical Committee 181-EAS - Early age shrinkage induced stresses and cracking in cementitious systems, 2003.

[40] P.H. Bischoff, Effects of shrinkage on tension stiffening and cracking in reinforced concrete, Canadian Journal of Civil Engineering. 28 (2001) 363–374. https://doi.org/10.1139/l00-117.

[41] G. Kaklauskas, V. Gribniak, D. Bacinskas, P. Vainiunas, Shrinkage influence on tension stiffening in concrete members, Eng Struct. 31 (2009) 1305–1312. https://doi.org/10.1016/j.engstruct.2008.10.007.

[42] M. Fastabend, T. Schäfers, M. Albert, B. Schücker, N. Doering, Fugenlose und fugenreduzierte Bauweise - Optimierung im Hochbau, Beton- Und Stahlbetonbau. 107 (2012) 225–235. https://doi.org/10.1002/best.201200008.

[43] F. Kanavaris, M. Azenha, D. Schlicke, K. Kovler, Longitudinal restraining devices for the evaluation of structural behaviour of cement-based materials: The past, present and prospective trends, Strain. 56 (2020). https://doi.org/10.1111/str.12343.

[44] A. Bentur, K. Kovler, Evaluation of early age cracking characteristics in cementitious systems, Mater Struct. 36 (2003) 183–190. https://doi.org/10.1007/BF02479556.

[45] F. Kanavaris, M. Azenha, M. Soutsos, K. Kovler, Assessment of behaviour and cracking susceptibility of cementitious systems under restrained conditions through ring tests: A critical review, Cem Concr Compos. 95 (2019) 137–153. https://doi.org/10.1016/j.cemconcomp.2018.10.016.

[46] A.B. Hossain, J. Weiss, Assessing residual stress development and stress relaxation in restrained concrete ring specimens, Cem Concr Compos. 26 (2004) 531–540. https://doi.org/10.1016/S0958-9465(03)00069-6.

[47] W.J. Weiss, S.P. Shah, Restrained shrinkage cracking: the role of shrinkage reducing admixtures and specimen geometry, Mater Struct. 35 (2002) 85–91. https://doi.org/10.1007/BF02482106.

[48] Z. Li, M. Qi, Z. Li, B. Ma, Crack width of high-performance concrete due to restrained shrinkage, Journal of Materials in Civil Engineering. 11 (1999) 214–223. https://doi.org/10.1061/(ASCE)0899-1561(1999)11:3(214).

[49] C.O. Surendra P. Shah Shashidhara Marikunte Wei Yang and Emil Becq-Giraudon, A Method to Predict Shrinkage Cracking of Concrete, ACI Mater J. 95 (n.d.). https://doi.org/10.14359/9875.

[50] K. Kovler, J. Sikuler, A. Bentur, Restrained shrinkage tests of fibre-reinforced concrete ring specimens: effect of core thermal expansion, Mater Struct. 26 (1993) 231–237. https://doi.org/10.1007/BF02472616.

[51] M. Grzybowski, S.P. Shah, Shrinkage cracking of fiber reinforced concrete, ACI Mater J. 87 (1990) 138–148.

[52] J.H. Moon, J. Weiss, Estimating residual stress in the restrained ring test under circumferential drying, Cem Concr Compos. 28 (2006) 486–496. https://doi.org/10.1016/j.cemconcomp.2005.10.008.

[53] H.T. See, E.K. Attiogbe, M.A. Miltenberger, Shrinkage cracking characteristics of concrete using ring specimens, ACI Mater J. 100 (2003) 239–245.

[54] R.N. Swamy, A.K. Bandyopadhyay, H. Stavrides, The ring method of measuring restrained shrinkage in mortar and concrete, Cem. Concr. Aggregates. 1 (1979) 13 – 20.

[55] R.N. Swamy, H. Stavrides, Influence of Fiber Reinforcement on Restrained Shrinkage and Cracking, ACI Journal Proceedings. 76 (1979) 443–460. https://doi.org/10.14359/6954.

[56] AASHTO, AASHTO T 334-08. Standard Method of Test for Estimating the Cracking Tendency of Concrete (2022).

[57] ASTM, ASTM C1581/C1581M-18a. Standard Test Method for Determining Age at Cracking and Induced Tensile Stress Characteristics of Mortar and Concrete under Restrained Shrinkage (2018).

[58] P. Soroushian, A. Alhozajiny, F. Mirza, Plastic Shrinkage Cracking of Polypropylene Fiber Reinforced Concrete, ACI Mater J. 92 (1995) 553–560. https://doi.org/10.14359/894.

[59] K. Yokoyama, S. Hiraishi, Y. Kasai, K. Kishitani, Shrinkage and cracking of high strength concrete and flowing concrete at early ages, in: V.M. Malhotra (Ed.), Proc. 4th CANMET/ACI International Conference on Superplasticizers and Other Chemical Admixtures in Concrete. ACI SP-148, American Concrete Institute, 1994: pp. 243–258.

[60] C.A. Shaeles, K.C. Hover, Influence of mix proportions and construction operations on plastic shrinkage cracking in thin slabs, Materials. 85 (1988) 495–504.

[61] P.P. Kraii, Proposed test to determine the cracking potential due to drying shrinkage of concrete, Concrete Construction. 30 (1985) 775-778.

[62] S. Guan, Influence of polypropylene fiber on concrete performance, Jianzhu Jiegou Xuebao/Journal of Building Structures. 27 (2006) 44–49.

[63] K. Xiao, J. Li, H. Yang, Study of crack resistance property of polyvinyl alcohol fiber reinforced concrete, 2011. https://doi.org/10.4028/www.scientific.net/AMR.287-290.178.

[64] S. Han, M. An, R. Guo, G. Liu, Crack resistance of ceramsite self-curing high performance concrete, Jianzhu Cailiao Xuebao/Journal of Building Materials. 18 (2015) 742–748. https://doi.org/10.3969/j.issn.1007-9629.2015.05.005.

[65] N. Banthia, C. Yan, S. Mindess, Restrained shrinkage cracking in fiber reinforced concrete: A novel test technique, Cem Concr Res. 26 (1996) 9–14. https://doi.org/10.1016/0008-8846(95)00186-7.

[66] N. Banthia, R. Gupta, Plastic shrinkage cracking in cementitious repairs and overlays, Mater Struct. 42 (2009) 567–579. https://doi.org/10.1617/s11527-008-9403-9.

[67] R.W. Poston, K. Kesner, J.E. McDonald, A.M. Vaysburd, P.H. Emmons, Concrete Repair Material Performance—Laboratory Study, ACI Mater J. 98 (2001). https://doi.org/10.14359/10197.

[68] M. Chilwesa, L. Facconi, F. Minelli, A. Reggia, G. Plizzari, Shrinkage induced edge curling and debonding in slab elements reinforced with bonded overlays: Influence of fibers and SRA, Cem Concr Compos. 102 (2019) 105–115. https://doi.org/10.1016/j.cemconcomp.2019.04.017.

[69] S.R. Kasu, S. Patel, A.R. Muppireddy, Field experiments and numerical analysis of curling behavior of cast-in-situ short paneled concrete pavement on lean concrete base, International Journal of Pavement Engineering. 23 (2022) 3743–3756. https://doi.org/10.1080/10298436.2021.1916820.

[70] A.M. Vaysburd, P.H. Emmons, B. Bissonnette, M. Pigeon, Some aspects of evaluating cracking sensitivity of repair materials, in: K. Kovler, A. Bentur (Eds.), International RILEM Conference on Early Age Cracking in Cementitious Systems, RILEM Publications, 2003: pp. 169–185.

[71] H.C.D. German Federal Ministry of Transport, TP BE-PCC - Technical Test Regulations for Concrete Substitution Systems Made of Cement Mortar/Concrete with a Plastic Additive (PCC). (1990).

[72] N. Banthia, M. Azzabi, M. Pigeon, Restrained shrinkage cracking in fibre-reinforced cementitious composites, Mater Struct. 26 (1993) 405–413. https://doi.org/10.1007/BF02472941.

[73] N. Banthia, M. Azzabi, M. Pigeon, Restrained Shrinkage Tests on Fiber Reinforced Cementitious Composites, in: D. Stevens, N. Banthia, V.S. Gopalaratnam, P.C. Tatnall (Eds.), SP-155: Testing of Fiber Reinforced Concrete, American Concrete Institute, 1995: pp. 137–151. https://doi.org/10.14359/932.

[74] M.P. Berke, N. Dallaire, Effect of Low Addition Rates of Polypropylene Fibers on Plastic Shrinkage Cracking and Mechanical Properties of Concrete, in: J.I. Danile, S.P. Shah (Eds.), SP-142: Fiber Reinforced Concrete Developments and Innovations, American Concrete Institute, 1994: pp. 19–42. https://doi.org/10.14359/1179.

[75] R. Breitenbücher, Investigation of thermal cracking with the cracking-frame, Mater Struct. 23 (1990) 172–177. https://doi.org/10.1007/BF02473015.

[76] RILEM TC 119-TCE, Recommendations of TC 119-TCE: Avoidance of thermal cracking in concrete at early ages, Mater Struct. 30 (1997) 451–464.

[77] K.A. Riding, J.L. Poole, A.K. Schindler, M.C.G. Juenger, K.J. Folliard, Statistical Determination of Cracking Probability for Mass Concrete, Journal of Materials in Civil Engineering. 26 (2014). https://doi.org/10.1061/(ASCE)MT.1943-5533.0000947.

[78] K.A. Riding, J.L. Poole, A.K. Schindler, M.C.G. Juenger, K.J. Folliard, Simplified concrete resistivity and rapid chloride permeability test method, ACI Mater J. 105 (2008) 390–394.

[79] A. Williams, A. Markandeya, Y. Stetsko, K. Riding, A. Zayed, Cracking potential and temperature sensitivity of metakaolin concrete, Constr Build Mater. 120 (2016) 172–180. https://doi.org/10.1016/j.conbuildmat.2016.05.087.

[80] K.A. Riding, J.L. Poole, A.K. Schindler, M.C.G. Juenger, K.J. Folliard, Effects of construction time and coarse aggregate on bridge deck cracking, ACI Mater J. 106 (2009) 448–454.

[81] B.E. Byard, A.K. Schindler, R.W. Barnes, Early-age cracking tendency and ultimate degree of hydration of internally cured concrete, Journal of Materials in Civil Engineering. 24 (2012) 1025–1033. https://doi.org/10.1061/(ASCE)MT.1943-5533.0000469.

[82] B.E. Byard, A.K. Schindler, R.W. Barnes, Cracking tendency of lightweight aggregate bridge deck concrete, ACI Mater J. 111 (2014) 179–188. https://doi.org/10.14359/51686499.

[83] M.N. Amin, J.-S. Kim, Y. Lee, J.-K. Kim, Simulation of the thermal stress in mass concrete using a thermal stress measuring device, Cem Concr Res. 39 (2009) 154–164. https://doi.org/10.1016/j.cemconres.2008.12.008.

[84] J.-H.J. Kim, S.-E. Jeon, J.-K. Kim, Development of new device for measuring thermal stresses, Cem Concr Res. 32 (2002) 1645–1651. https://doi.org/10.1016/S0008-8846(02)00842-6.

[85] B. Kim, W.J. Weiss, Using acoustic emission to quantify damage in restrained fiber-reinforced cement mortars, Cem Concr Res. 33 (2003) 207–214. https://doi.org/10.1016/S0008-8846(02)00978-X.

[86] J.-J. Park, D.-Y. Yoo, S.-W. Kim, Y.-S. Yoon, Drying shrinkage cracking characteristics of ultra-highperformance fibre reinforced concrete with expansive and shrinkage reducing agents, Magazine of Concrete Research. 65 (2013) 248–256. https://doi.org/10.1680/macr.12.00069.

[87] T.-S. Seo, M.-S. Lee, Experimental Study on Tensile Creep of Coarse Recycled Aggregate Concrete, Int J Concr Struct Mater. 9 (2015) 337–343. https://doi.org/10.1007/s40069-015-0105-8.

[88] T. Seo, M. Lee, C. Choi, Y. Ohno, Properties of drying shrinkage cracking of concrete containing fly ash as partial replacement of fine aggregate, Magazine of Concrete Research. 62 (2010) 427–433. https://doi.org/10.1680/macr.2010.62.6.427.

[89] S.S. Park, S.-J. Kwon, H.-W. Song, Analysis technique for restrained shrinkage of concrete containing chlorides, Materials and Structures/Materiaux et Constructions. 44 (2011) 475–486. https://doi.org/10.1617/s11527-010-9642-4.

[90] K.-K. Choi, G.T. Truong, S.-J. Choi, Restrained shrinkage cracking of amorphous metallic fibre-reinforced concrete, Proceedings of the Institution of Civil Engineers: Structures and Buildings. 168 (2015) 902–914. https://doi.org/10.1680/stbu.14.00051.

[91] W. Jason Weiss, W. Yang, S.P. Shah, Shrinkage cracking of restrained concrete slabs, J Eng Mech. 124 (1998) 765–773. https://doi.org/10.1061/(asce)0733-9399(1998)124:7(765).

[92] K.H. Younis, K. Pilakoutas, Assessment of post-restrained shrinkage mechanical properties of concrete, ACI Mater J. 113 (2016) 267–276. https://doi.org/10.14359/51688699.

[93] Z. Al-Kamyani, K. Pilakoutas, M. Guadagnini, P. Papastergiou, Free and restrained shrinkage of hybrid steel fibres reinforced concrete, in: High Tech Concrete: Where Technology and Engineering Meet - Proceedings of the 2017 Fib Symposium, 2017: pp. 339–346. https://doi.org/10.1007/978-3-319-59471-2_41.

[94] R. Lameiras, M. Azenha, J. Barros, Concepção de sistemas de restrição passiva à retracção para avaliação das tensões associadas à deformação impedida, in: BE2010—Econtro Nacional Betao Estutural, Lisboa, 2010.

[95] R. Springenschmid, R. Breitenbucher, M. Mangold, Development of the cracking frame and the temperature stress testing machine, in: R. Springenschmid (Ed.), Proceedings of the RILEM Symposium in Thermal Cracking in Concrete at Early Ages, Munich, Germany, 1994.

[96] R. Bloom, A. Bentur, Free and restrained shrinkage of normal and high-strength concretes, ACI Mater J. 92 (1995) 211–217.

[97] A. Darquennes, S. Staquet, M.-P. Delplancke-Ogletree, B. Espion, Effect of autogenous deformation on the cracking risk of slag cement concretes, Cem Concr Compos. 33 (2011) 368–379. https://doi.org/10.1016/j.cemconcomp.2010.12.003.

[98] M. Sule, K. van Breugel, The effect of reinforcement on early-age cracking due to autogenous shrinkage and thermal effects, Cem Concr Compos. 26 (2004) 581–587. https://doi.org/10.1016/S0958-9465(03)00078-7.

[99] M. Sule, K. van Breugel, Cracking behaviour of reinforced concrete subjected to early-age shrinkage, Materials and Structures/Materiaux et Constructions. 34 (2001) 284–292. https://doi.org/10.1617/13758.

[100] P. Lura, K. van Breugel, I. Maruyama, Effect of curing temperature and type of cement on early-age shrinkage of high-performance concrete, Cem Concr Res. 31 (2001) 1867–1872. https://doi.org/10.1016/S0008-8846(01)00601-9.

[101] K. Kovler, S. Igarashi, A. Bentur, Tensile creep behavior of high strength concretes at early ages, Materials and Structures/Materiaux et Constructions. 32 (1999) 383–387. https://doi.org/10.1007/bf02479631.

[102] A.A.M. Neto, M.A. Cincotto, W.L. Repette, Retração restringida e fluência por tração: desenvolvimento de equipamento e metodologia, in: 50º Congresso Brasileiro Do Concreto Do Instituto Brasileiro Do Concreto IBRACON, 2008.

[103] B. Delsaute, C. Boulay, S. Staquet, Creep testing of concrete since setting time by means of permanent and repeated minute-long loadings, Cem Concr Compos. 73 (2016) 75–88. https://doi.org/10.1016/j.cemconcomp.2016.07.005.

[104] K. Hájková, D. Schlicke, K. Turner, V. Šmilauer, P. Havlásek, P. Heinrich, Validation of CTU Prague thermo-mechanical simulator with TU Graz restraining frame experiments, in: S. Staquet, D. Aggelis (Eds.), Proceedings of the 2nd International RILEM/COST Conference on Early Age Cracking and Serviceability in Cement-Based Materials and Structures Volume 2, 2017: pp. 703–708.

[105] K. Turner, D. Schlicke, N.V. Tue, Restrained Concrete Members - New Findings from Systematic Investigations with Restraint Frames for Reinforced Concrete | Zwangbeanspruchung von Stahlbetonbauteilen: Neue Erkenntnisse aus der systematischen Untersuchung mit Zwangrahmen für bewehrten Beton, Beton- Und Stahlbetonbau. 111 (2016) 301–309. https://doi.org/10.1002/best.201600003.

[106] D. Schlicke, K. Hofer, N.V. Tue, Adjustable Restraining Frames for Systematic Investigation of Cracking Risk and Crack Formation in Reinforced Concrete Under Restrained Conditions, in: 2020: pp. 211–239. https://doi.org/10.1007/978-3-030-39738-8_7.

[107] J. Gomes, J. Granja, C. Sousa, C. Ferreira, D. Schlicke, R. Faria, M. Azenha, Long-Term Experimental Campaign on RC Shrinkage Cracking: Conceptualization, Planning and Experimental Procedures, 2021. https://doi.org/10.1007/978-3-030-72921-9_12.

[108] J.G. Gomes, J. Granja, C. Sousa, B. Zahabizadeh, R. Faria, D. Schlicke, M. Azenha, A new test setup for simulation of the combined effect of bending and axial restraint in slab-like specimens, Eng Struct. 225 (2020). https://doi.org/10.1016/j.engstruct.2020.111251.

[109] J.G. Gomes, M. Azenha, J. Granja, R. Faria, C. Sousa, B. Zahabizadeh, A. Edalat-Behbahani, D. Schlicke, Proposal of a test set up for simultaneous application of axial restraint and vertical loads to slab-like specimens: sizing principles and application, in: SynerCrete'18 International Conference on Interdisciplinary Approaches for Cement-Based Materials and Structural Concrete, Funchal, 2018.

[110] M. Azenha, Numerical simulation of the structural behaviour of concrete since its early ages, Numerical Simulation of the Structural Behaviour of Concrete since Its Early Ages. (2009).

[111] C. Ferreira, C. Sousa, R. Faria, M. Azenha, M. Pimentel, Thermo-Hygro-Mechanical Simulation of Cracking in Thick Restrained RC Members: Application to a 50cm Thick Slab, Journal of Advanced Concrete Technology. 17 (2019) 489–505. https://doi.org/10.3151/jact.17.489.

[112] D. Ferreira, DIANA 10.4 user's manual, (2020).

[113] F.P. Incropera, D.P. DeWitt, T.L. Bergman, A.S. Lavine, Fundamentals of heat and mass transfer, Wiley, New York, 1996.

[114] H. Reinhardt, J. Blaauwendraad, J. Jongedijk, Temperature development in concrete structures taking account of state dependent properties, in: International Conference on Concrete at Early Ages., 1982.

[115] Jonasson J-E., Modelling of temperature, moisture and stresses in young concrete., Luleå tekniska universitet, 1994.

[116] V. Baroghel-Bouny, M. Mainguy, T. Lassabatere, O. Coussy, Characterization and identification of equilibrium and transfer moisture properties for ordinary and high-performance cementitious materials, Cem Concr Res. 29 (1999) 1225–1238. https://doi.org/10.1016/S0008-8846(99)00102-7.

[117] J.R. Rico, Effect of superplasticizers on the behavior of concrete in the fresh and hardened states: implications for high performance concretes, PhD thesis, Universitat Politècnica de Catalunya (UPC), 2000.

[118] Z.P. Bažant, L.J. Najjar, Non-linear water diffusion in nonsaturated concrete, Matériaux et Constructions. 5 (1972) 3–20. https://doi.org/10.1007/BF02479073.

[119] H.-G. Kwak, S.-J. Ha, J.-K. Kim, Non-structural cracking in RC walls: Part I. Finite element formulation, Cem Concr Res. 36 (2006) 749–760. https://doi.org/https://doi.org/10.1016/j.cemconres.2005.12.001.

[120] Z.P. Bažant, E. Osman, Double power law for basic creep of concrete, Matériaux et Construction. 9 (1976) 3–11. https://doi.org/10.1007/BF02478522.

[121] J.G. Rots, J. Blaauwendraad, Crack models for concrete, discrete or smeared? Fixed, multi-directional or rotating?, HERON, 34 (1), 1989. (1989).

[122] K. Maekawa, F. Vecchio, O. Bayrak, E. Bentz, J. Blaauwendraad, J. Cervenka, V. Cervenka, T. Ishida, M. Jirasek, W. Kaufmann, J. Kollegger, D. Kuchma, H.J. Lee, G. Mancini, G. Monti, J. Ozbolt, C. Preisinger, E. Spacone, T. Tjhin, fib Bulletin 45. Practitioners' guide to finite element modelling of reinforced concrete structures, fib. The International Federation for Structural Concrete, 2008. https://doi.org/10.35789/fib.BULL.0045.

[123] P. Marti, M. Alvarez, W. Kaufmann, V. Sigrist, Tension Chord Model for Structural Concrete, Structural Engineering International. 8 (1998) 287–298. https://doi.org/10.2749/101686698780488875.

[124] C. Sousa, L. Leitão, R. Faria, M. Azenha, A formulation to reduce mesh dependency in FE analyses of RC structures under imposed deformations, Eng Struct. 132 (2017) 443–455. https://doi.org/10.1016/j.engstruct.2016.11.040.

[125] F.H. Feenstra, R. de Borst, Aspects of robust computational modeling for plain and reinforced concrete, HERON, 38 (4), 1993. (1993).

[126] J. Schnell, A. Albert, A. Dridiger, Ressourcenschonende Reduktion von Bewehrungsstahl in Hochbaudecken. (SWD-10.08.18.7-14.17) - Forschungsbericht, Technische Universität Kaiserslautern. ISBN: 978-3-7388-0077-7., Fraunhofer IRB Verlag, 2017.

[127] E. Fehling, T. Lautbecher, Beschränkung der Rißbreite bei kombinierter Beanspruchung aus Last und Zwang, Beton- Und Stahlbetonbau. 98 (2003) 377–388. https://doi.org/https://doi.org/10.1002/best.200301860.

[128] ISO, ISO 10303: Industrial automation systems and integration - Product data representation and exchange, (1994).

[129] CEN, EN 1991-1-1: Eurocode 1 Actions on structures – Part 1-1: General actions – densities, self-weight, imposed loads for buildings, (2002).

[130] J.L. Granja, M. Azenha, C. de Sousa, R. Faria, J. Barros, Hygrometric Assessment of Internal Relative Humidity in Concrete: Practical Application Issues, Journal of Advanced Concrete Technology. 12 (2014) 250–265. https://doi.org/10.3151/jact.12.250.

[131] CEN, EN 12390-3 testing hardened concrete – Part 3: Compressive strength of test specimens., (2009).

[132] CEN, EN 12390-13 testing hardened concrete – Part 13: Determination of secant modulus of elasticity in compression., (2013).

[133] CEN, EN 12390-6 Testing hardened concrete – Part 6: Tensile splitting strength of test specimens., (2009).

[134] RILEM, Recommendations of RILEM TC 162-TDF: Test and design methods for steel fibre reinforced concrete: bending test., Mater Struct. 35 (2002) 579–582.

[135] ASTM, C512–02 Standard Test Method for Creep of Concrete in Compression., (2002).

[136] J. Gomes, M. Azenha, J. Granja, R. Faria, C. Sousa, B. Zahabizadeh, A. Edalat-Behbahani, D. Schlicke, Proposal of a test set up for simultaneous application of axial restraint and vertical loads to slab-like specimens: sizing principles and application, in: SynerCrete'18 International Conference on Interdisciplinary Approaches for Cementbased Materials and Structural Concrete., Funchal, Madeira Island, Portugal, 2018: pp. 303–308.

[137] Gomes J., J. Granja, Sousa C., Ferreira C., Schlicke D., Faria R., Azenha M., Long-Term Experimental Campaign on RC Shrinkage Cracking: Conceptualization, Planning and Experimental Procedures, in: F. and A.M. Kanavaris Fragkoulis and Benboudjema (Ed.), International RILEM Conference on Early-Age and Long-Term Cracking in RC Structures, Springer International Publishing, Cham, 2021: pp. 141–153. https://doi.org/10.1007/978-3-030-72921-9_12.

[138] CEN, EN 12390-2: Testing hardened concrete - Part 2: Making and curing specimens for strength tests, (2019).

[139] Z.P. Bazant, Prediction of Concrete Creep Effects Using Age-Adjusted Effective Modulus Method, ACI Journal Proceedings. 69 (1972) 212–219. https://doi.org/10.14359/11265.

[140] CEN, EN 1990: Eurocode - Basis of structural design., (2002).

[141] M. Azenha, L. Leitão, J.L. Granja, C. de Sousa, R. Faria, J.A.O. Barros, Experimental validation of a framework for hygro-mechanical simulation of self-induced stresses in concrete, Cem Concr Compos. 80 (2017) 41–54. https://doi.org/https://doi.org/10.1016/j.cemconcomp.2017.02.008.

[142] C. Boulay, S. Staquet, M. Azenha, A. Deraemaeker, M. CRESPINI, J. Carette, J. Granja, B. Delsaute, C. Dumoulin, G. Karaiskos, Monitoring elastic properties of concrete since very early age by means of cyclic loadings, ultrasonic measurements, natural resonant frequency of composite beam (EMM-ARM) and with smart aggregates, 2013.

[143] V. Malárics, H.S. Müller, Evaluation of the splitting tension test for concrete from a fracture mechanical point of view, Proc. of 7th International Conference on Fracture Mechanics of Concrete and Concrete Structures. 7 (2010) 709 – 716. https://www.scopus.com/inward/record.uri?eid=2-s2.0-84870027174&partnerID=40&md5=49947c0e09a394605db7ed435698fdac.

[144] G. Zhang, C. Li, H. Wei, M. Wang, Z. Yang, Y. Gu, Influence of Humidity on the Elastic Modulus and Axis Compressive Strength of Concrete in a Water Environment, Materials. 13 (2020) 5696. https://doi.org/10.3390/ma13245696.

[145] B.D. Liu, W.J. Lv, L. Li, P.F. Li, Effect of moisture content on static compressive elasticity modulus of concrete, Constr Build Mater. 69 (2014) 133–142. https://doi.org/https://doi.org/10.1016/j.conbuildmat.2014.06.094.

[146] I. Maruyama, Impact of drying on concrete and concrete structures, RILEM Technical Letters. 7 (2022) 1–11. https://doi.org/10.21809/rilemtechlett.2022.154.

[147] J.-K. Kim, C.-S. Lee, Prediction of differential drying shrinkage in concrete, Cem Concr Res. 28 (1998) 985–994. https://doi.org/https://doi.org/10.1016/S0008-8846(98)00077-5.

[148] V.D. da Silva, Mechanics and Strength of Materials, Springer Berlin Heidelberg, Berlin, Heidelberg, 2006. https://doi.org/10.1007/3-540-30813-X.

[149] CEN, EN 12390-5 Testing hardened concrete - Part 5: Flexural strength of test specimens, (2019).

[150] Boris Bresler, Lawrence Selna, Analysis of Time-Dependent Behavior of Reinforced Concrete Structures, ACI Symposium Publication. SP-9 (1964) 115–128. https://doi.org/10.14359/17222.

[151] O. Faber, PLASTIC YIELD, SHRINKAGE, AND OTHER PROBLEMS OF CONCRETE, AND THEIR EFFECT ON DESIGN., Minutes of the Proceedings of the Institution of Civil Engineers. 225 (1928) 27–73. https://doi.org/10.1680/imotp.1928.14232.

[152] G. Lacidogna, M. Tarantino, Approximate expressions for the ageing coefficient and the relaxation function in the viscoelastic analysis of concrete structures, Mater Struct. 29 (1996) 131–140. https://doi.org/10.1007/BF02486158.

[153] M.A. Chiorino, G. Lacidogna, Approximate values of ageing coefficient for the age-adjusted-effective-modulus method in linear creep analysis of concrete structures (CEB Model 1990 for Creep). Atti del Dipartimento di Ingegneria Strutturale, (1991).

[154] J.L.D. Granja, Continuous characterization of stiffness of cement-based materials: experimental analysis and micro-mechanics modelling., PhD Thesis, University of Minho, 2016.

[155] B. Delsaute, C. Boulay, J. Granja, J. Carette, M. Azenha, C. Dumoulin, G. Karaiskos, A. Deraemaeker, S. Staquet, Testing Concrete E-modulus at Very Early Ages Through Several Techniques: An Inter-laboratory Comparison, Strain. 52 (2016) 91–109. https://doi.org/10.1111/str.12172.

[156] Z.P. Bazant, J. Chern, Log Double Power Law for Concrete Creep, ACI Journal Proceedings. 82 (n.d.). https://doi.org/10.14359/10377.

[157] D.S. Atrushi, Tensile and Compressive Creep of Early Age Concrete: Testing and Modelling, PhD Thesis, The Norwegian University of Science and Technology , 2003.

[158] M. Azenha, R. Faria, D. Ferreira, Identification of early-age concrete temperatures and strains: Monitoring and numerical simulation, Cem Concr Compos. 31 (2009) 369–378. https://doi.org/10.1016/j.cemconcomp.2009.03.004.

[159] B. Zahabizadeh, A. Edalat-Behbahani, J. Granja, J.G. Gomes, R. Faria, M. Azenha, A new test setup for measuring early age coefficient of thermal expansion of concrete, Cem Concr Compos. 98 (2019). https://doi.org/10.1016/j.cemconcomp.2019.01.014.

[160] C. Sousa, R. Faria, E. Felisberto, Dimensionamento de Armaduras Mínimas em Lajes Restringidas Considerando a Interação Solo-Estrutura, in: Encontro Nacional Betão Estrutural - BE2016, 2016: pp. 73–80.